Eindhoven University of Technology

MASTER

Explorative study on simple rhodanine based non-fullerene acceptors for use in organic photovoltaics

Louw, F.J.M.

Award date:
2021

Link to publication

Disclaimer
This document contains a student thesis (bachelor's or master's), as authored by a student at Eindhoven University of Technology. Student theses are made available in the TU/e repository upon obtaining the required degree. The grade received is not published on the document as presented in the repository. The required complexity or quality of research of student theses may vary by program, and the required minimum study period may vary in duration.

General rights
Copyright and moral rights for the publications made accessible in the public portal are retained by the authors and/or other copyright owners and it is a condition of accessing publications that users recognise and abide by the legal requirements associated with these rights.

- Users may download and print one copy of any publication from the public portal for the purpose of private study or research.
- You may not further distribute the material or use it for any profit-making activity or commercial gain

Explorative study on simple rhodanine based non-fullerene acceptors for use in organic photovoltaics

Graduation report of

Sietske (F.J.M.) de Louw

Supervisor: Dr. ir. Pieter J. Leenaers
Supervising professor: Prof. dr. ir. René A. J. Janssen

Molecular Systems & Materials Chemistry (MSMC)
Eindhoven University of Technology
May 2021

TU/e EINDHOVEN UNIVERSITY OF TECHNOLOGY

Abstract

In this work, the synthesis, optoelectronic properties and photovoltaic performance of several new and simple A-D-A type non-fullerene acceptors with rhodanine as the electron-accepting unit are investigated. Simple structured non-fullerene acceptors (NFAs) are a means to reduce the synthetic costs of photovoltaic devices, hereby aiding the commercialization of these devices. Research by the group of Eunhee Lim has shown that a simple NFA, consisting of a bithiophene core flanked by two octyl *N*-functionalized rhodanines, can achieve a promising photovoltaic performance of 9.33%. Therefore this material is synthesized and used as a reference in this research. The goal of this research is to investigate the effect of structural changes on the performance of similar simple A-D-A type NFAs.

In chapter 2, the octyl side-chains on the acceptor units of the reference NFA (**2T-ORh**) are changed to 2'-ethylhexyl side-chains (**2T-EHRh**). The absorption spectra and energy levels of this new NFA are compared to that of **2T-ORh**. It is found that changing the side-chain results in a different aggregation behavior, whereas the energy levels remain equal. For each NFA, different processing conditions are required to obtain the best device performance. For **2T-ORh**, solvent vapor annealing (SVA) results in a 4.74% device, whereas the best device for **2T-EHRh** (5.19%) is obtained by adding 2 vol% of DPE in the casting solution.

Chapter 3 describes structural variations in the core of the reference NFA. For this, the core is changed to either a thienothiophene, a thiophene-furan or a bifuran. Changing the core to a thienothiophene reduces the solubility to such an extent that the molecule cannot be used in photovoltaic devices. While the furan-based NFAs and **2T-ORh** show virtually identical absorption spectra in solution, their aggregation behavior in thin film is remarkably different. **TF-ORh** shows a poor device performance of 0.32%, which worsens by SVA or addition of a co-solvent. The performance of **2F-ORh** was maximized at 1.87%, which is still remarkably lower than the reference material. Atomic force microscopy (AFM) shows a large phase-segregation for both furan-based NFAs, explaining the low efficiencies.

Contents

Chapter 1: Introduction

Abstract

This chapter shows the importance of the use of renewable energy resources to reduce global warming. Solar energy is shown as one of the most promising renewable energy resources and organic photovoltaics is introduced as emerging photovoltaic technology. Next, the operating principle of OPV devices, the device structure and their characterization are discussed. Furthermore, the importance of finding new acceptor materials is stressed and an overview of the current acceptor materials in OPV devices is given. Lastly, the research goal of this project is stated.

1. Photovoltaics as a renewable energy resource to reduce global warming

2020 was the second warmest year on record, with a 0.98 °C average surface temperature anomaly compared to the 20th century average.[1,2] The increase in surface temperature is related to an increased concentration of greenhouse gasses such as carbon dioxide in the atmosphere. These gasses absorb heat that is reflected from the earth's surface and would otherwise be emitted back into space.[3] The primary source of CO_2 emission is the combustion of fossil fuels for electricity, heat and transportation.[4] In order to mitigate the threat of climate change, the European Green Deal has set the objective to become the first climate-neutral continent by 2050.[5] To achieve this goal, a gradual change towards the use of renewable energy resources is needed. These resources replenish themselves naturally, whereas depletion of fossil fuels is a serious problem.[6]

Renewable energy resources include for instance: hydropower, wind energy and solar energy. Of these three, solar energy is the most promising owing to its vast availability.[7] This availability is illustrated by the fact that the 120.000 TW of solar radiation that reaches the earth's surface far exceeds the global energy demand.[8] Solar energy can be harvested with several solar technologies, for instance thermal solar power and photovoltaics. Of these methods, photovoltaics (PV) is the most versatile as it directly converts sunlight into electricity.[9]

2. Different generations of photovoltaics

The photovoltaic market consists of a wide range of techniques, which all have certain benefits and limitations. These techniques can roughly be divided into three generations, classified by the level of commercial availability.[10–12]

First Generation
The oldest and still the most widely used photovoltaic devices are of the first generation; these are the crystalline silicon photovoltaic devices. These devices still dominate the PV market owing to their high efficiencies and good stability.[13,14] Originally, the overall costs per watt of this type of photovoltaics were relatively high, which led to the development of the second generation photovoltaics. Nowadays, the production costs have decreased and the efficiency of the modules has increased, which has significantly reduced the costs per watt.[15,16]

Second Generation
This generation mainly comprises thin film technologies and includes for instance amorphous silicon (a-Si), copper indium gallium (di)selenide (CIGS) and cadmium telluride (CdTe).[7] Another advantage of thin film photovoltaic devices is their flexibility, which generates the possibility to produce flexible modules. Although the costs per area in these type of devices are substantially lower than for the first generation photovoltaics, the low efficiencies and/or toxic or rare materials make these type of photovoltaic devices less commercially attractive.[17]

Third Generation
The last generation of photovoltaic devices is focusing on emerging PV technologies, meaning that they are still in the research or development stage. These devices are designed to overcome the limitations of earlier generations.[18] Recent research on these devices has been focusing on approaching the Shockley-Queisser limit for single junction cells, which is 33.7%, or the thermodynamic limit for multi junction cells.[19] Some examples of third generation photovoltaic devices are: dye-sensitized photovoltaics, organic photovoltaics, perovskite photovoltaics and tandem cells.

3. Organic photovoltaics

Although the earliest studies on organic semiconductors date back to the early 20th century,[20] these type of semiconductors only gained attention after the 1970s, when Chiang *et al.* showed that doped conjugated polymers can conduct electricity.[21,22] The use of organic semiconductors in electronic devices has several advantages over the use of their inorganic counterparts. First of all, organic semiconductors consist of non-toxic and abundant carbon-based materials. Secondly, their high absorption coefficient allows them to be used in the thin film industry, which lowers material costs. Lastly, the active layer is completely solution processable, allowing devices to be manufactured via fast and cheap roll-to-roll or other printing techniques.[20,22–24] These advantageous properties have led to a new kind of photovoltaic device, namely organic photovoltaics (OPVs).[20] The first report of organic systems producing a photovoltaic effect dates back to 1958 when Kearns and Calvin reported a 200 mV photovoltage for a system consisting of magnesium phthalocyanine and tetramethyl *p*-phenylenediamine.[25] This discovery was quickly followed by others and in 1985 Tang was the first to produce a working OPV device by using a heterojunction between a donor (p-type) and an acceptor (n-type) material.[26] By using copper phthalocyanine as the p-type material and a perylene tetracarboxylic derivative as the n-type material, Tang achieved a power conversion efficiency of 1% under simulated AM2 illumination.

3.1 Operating principle

In contrast to inorganic semiconductors, excitation in organic semiconductors does not directly result in free charges. Instead, owing to the relatively low dielectric constants in organic materials excitation leads to a coulombically bound electron-hole pair (exciton),[27] as schematically depicted in **Figure 1.1a**. As this exciton is a neutral quasiparticle, it does not contribute to the photocurrent and thus first needs to dissociate into free charges. This dissociation occurs at the junction between a donor and an acceptor material, where there is an offset between their energy levels (**Figure 1.1c**). When this energy offset is sufficiently large, *i.e.* larger than the exciton binding energy, the exciton can dissociate into a free electron and a free hole. An electric field, caused by the difference in work functions between the two electrodes, assists the further separation of these charges and their subsequent transport to the correct electrodes (**Figure 1.1d**).[28] At the electrodes, the charges are collected for use in the external circuit (**Figure 1.1e**).

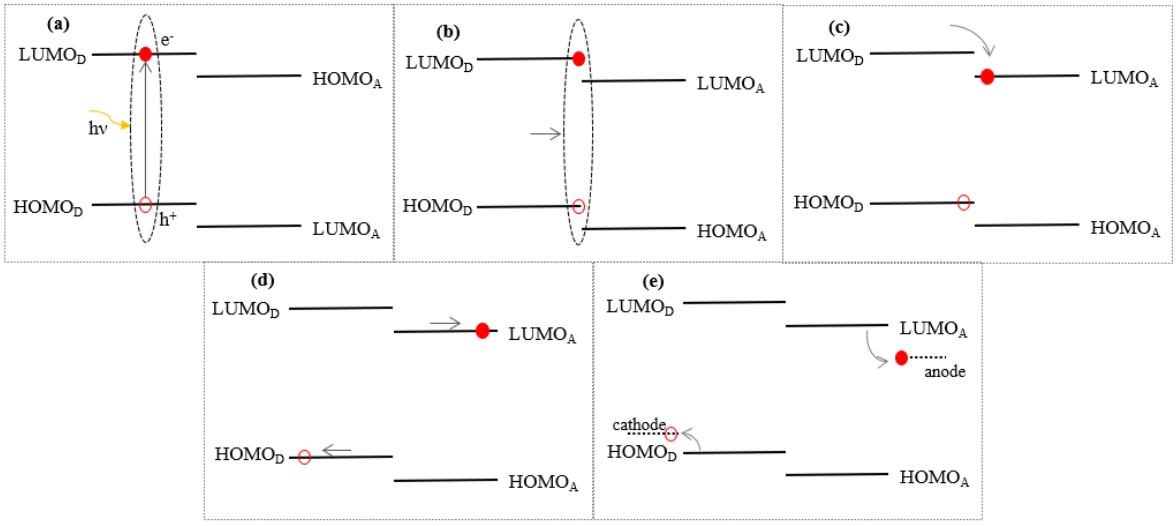

Figure 1.1: Schematic illustration of the entire charge collection process in an OPV device with: (a) photoexcitation, (b) exciton diffusion to donor/acceptor interface, (c) charge separation, (d) charge transport and (e) charge collection. LUMO stands for the lowest unoccupied molecular orbital, HOMO for the highest occupied molecular orbital and the subscripts D and A for donor and acceptor respectively. This scheme assumes donor excitation. Acceptor excitation is also possible, but then the hole will transfer to the HOMO of the donor.

3.2 Morphology

Because exciton dissociation can only occur at the junction between the donor and acceptor material, the exciton first needs to diffuse towards this junction (**Figure 1.1b**). Knowing that excitons in organic semiconductors have a limited diffusion length of around 10 nm,[29,30] layers of donor and acceptor material can only be 10 nm thick so that all excitons can reach the junction. While a thin bilayer structure would allow for efficient exciton dissociation, the thin layers can only absorb a limited amount of sunlight, as demonstrated by the low current obtained in the work of Tang.[26] A second limitation in this bilayer structure is the relatively small junction area, where the dissociation occurs. Both these features limit the efficiency of a bilayer photovoltaic device.

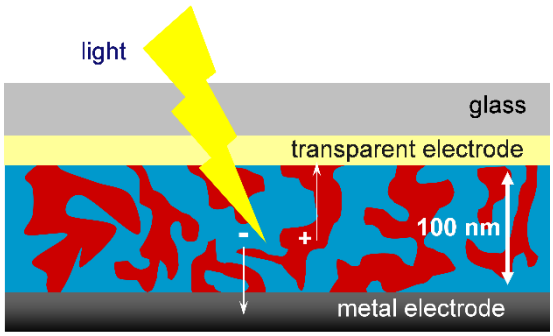

Figure 1.2: Schematic representation of a BHJ morphology.[31]

A major breakthrough in the field of OPVs came in 1991 with the invention of the bulk heterojunction (BHJ).[32] In an OPV device with a BHJ the two absorber materials are intimately mixed to create a large junction area for charge dissociation (**Figure 1.2**).[33] Using such a lay-out allows for a much thicker active layer, ~100 nm,[34] compared to a bilayer structure. The efficiency of a BHJ OPV strongly depends on the morphology of the active layer, in which the degree of phase separation is an important factor.[35] The ideal BHJ morphology has several crucial characteristics. Firstly, the domain size of the acceptor or donor material needs to be smaller than the exciton diffusion length in at least one direction. Secondly, there need to be continuous pathways to transport charge carriers to their respective electrodes. These pathways need to consist out of pure and crystalline material such that the amount of defects in the material are kept to a minimum. These defects act as energetic traps favoring bimolecular recombination. Additionally a high domain purity and crystallinity allow for a higher charge mobility, which increases the efficiency.[36,37] This shows that control over the active layer morphology is a key parameter in achieving efficient photovoltaic devices. However, practically the morphology is hard to control.

There are several commonly employed strategies to control the active layer morphology. One of them is the choice of the donor and acceptor components in the casting solution. Both components need to have a sufficiently high solubility in the primary casting solvent to create a blended film with an appropriate thickness. However, a certain limit in the solubility is needed in order to promote phase separation.[38] Eventually, upon complete drying of a film it is kinetically "frozen" meaning that the solvent evaporation rate is a key-factor in determining the film crystallinity.[39] Due to the limited selection of casting solvents, effectively controlling the phase separation in a single solvent system has proven difficult, giving either insufficient or excessive phase separation. Therefore other methods to control the degree of phase separation have been investigated. One way is the incorporation of co-solvents or additives in the casting solution. These additives are chosen to selectively solubilize one of the components in the blend (D or A) during the drying process. Thus, they should have a higher boiling point than the primary solvent. During the drying of the film the increased solubility difference between D and A allows them to form more crystalline domains,[40] as well as more favorable domain sizes.[41] Another commonly employed morphology optimization method is varying the donor/acceptor ratio. Altering this ratio has an effect on the size and the distribution of the domains, which may lead to a changed interface surface and in its turn a different probability of exciton dissociation.[42]

Besides changing the casting solution and thus the morphology during processing, post-treatment steps are also commonly employed to change the active layer morphology. These post-treatment steps are also known as annealing methods and the two most widely employed methods are thermal annealing (TA) and solvent vapor annealing (SVA). In thermal annealing, heat is supplied to the deposited film which causes increased molecular mobility. The increased mobility allows the molecules to reorient themselves, which attributes to an increased domain crystallinity, as well as diminishing defects and improve phase separation.[43–45] Solvent vapor annealing is commonly known as a milder annealing method, because it is suitable for ambient processing conditions. During annealing, solvent vapor penetrates the deposited film, which partially solubilizes one or both of the components in the film. This allows them to reorient in a more ordered packing, thereby increasing the domain crystallinity and improve phase separation.[46–48]

4. OPV device structure

An OPV device usually comprises multiple thin layers deposited on a substrate. Besides the three main layers for a working solar cell, the active layer and the two electrodes, transport layers are just as important for efficiency (**Figure 1.3**). As mentioned earlier, the active layer is a blend of donor and acceptor material and is responsible for the absorption of solar radiation and for converting it to free charges. The transport layers in **Figure 1.3**, denoted as electron and hole transport layers (ETL and HTL), have multiple functions. These functions include protection of the active layer, providing ohmic contacts with the electrode and forming selective contacts for one specific charge carrier.[49] A device can be built in two different lay-outs, depending on the configuration of the electrodes and transport layers and thus the direction of the charge flow, as shown in **Figure 1.3**. In both lay-outs the front electrode, where sunlight enters the cell, is a transparent conductive oxide (TCO). A commonly employed TCO is indium tin oxide (ITO) due to its exceptional electrical and optical properties.[50] The back electrode is usually a shiny metal in both lay-outs and thus also acts as a reflective coating, thereby increasing the probability of solar radiation absorption.

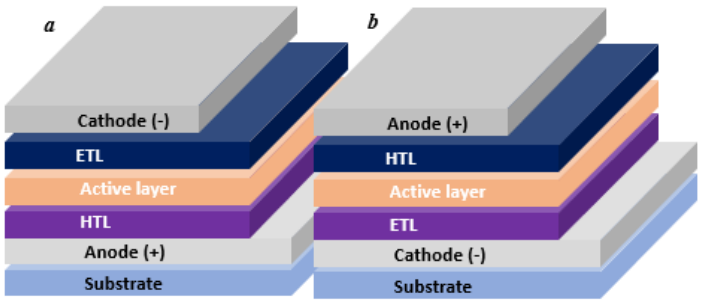

Figure 1.3: OPV device lay-out in (a) regular and (b) inverted structure.

In the regular lay-out, the HTL is deposited on top of the ITO. Poly(3,4-ethylenedioxythiophene):polystyrenesulfonate (PEDOT:PSS) is often used as HTL. Besides its function as transport layer it is also known to smoothen the ITO surface, thereby preventing possible pinhole formation. At the back side a low work-function ETL and cathode complete the device. Often used combinations are Ca/Al or LiF/Al, of which LiF/Al is more commonly used due to higher reported efficiencies.[51] A drawback of the regular lay-out is its short-term stability. Both interface layers, ETL and HTL, are known to degrade the device lifetime. The low work-function metals are prone to oxidation,[52] whereas the acidity of PEDOT:PSS causes interface instability.[53]

These instabilities are decreased in the inverted lay-out, where the low work-function metal is not in contact with air. In this lay-out the ETL has an extra property, it should lower the work-function of the ITO in order to be employed as a cathode. N-type metal-oxides, such as zinc oxide and titanium oxide, are often used owing to their solution processability, transparency and good electron selectivity.[52,54] Of these metal-oxides, ZnO is most widely used as ETL due to a better synthetic availability.[55] However, the trap and defect states caused by the relatively rough surface of the ZnO aid the recombination of charge carriers. Therefore, a passivation layer that is able to smoothen the contact between the active layer and the ZnO is usually employed. Several polymers have shown to effectively modify the ZnO surface and thereby decrease the charge recombination. One commonly employed passivation layer is polyethyleneimine ethoxylated (PEIE) which smoothens the surface and further decreases the ITO work-function, making it a better ETL.[56–58] A high work-function transition metal oxide HTL, often molybdenum oxide (MoO_3), and stable metal electrode, Ag, complete the device.

In this thesis, only devices with an inverted structure, based on ZnO+PEIE, MoO_3 and Ag, will be shown.

5. Characterization of OPV

Sunlight is a collection of electromagnetic radiation of different energies. The earth's atmosphere absorbs part of this radiation, limiting the amount of energy that reaches the surface. This shows that the energy available for a photovoltaic device depends on the pathlength traveled through the atmosphere and thus the angle of the sun to the surface. In order to limit deviations by the use of different solar energy references, a standardized solar spectrum has been defined. This spectrum, AM1.5G or Air Mass 1.5 Global, shows the energy flux of solar radiation which has traveled through 1.5 times the thickness of the atmosphere on a clear day (**Figure 1.4**). Integration of the spectrum yields the maximum power of the incident light and is equal to 1000 W m^{-2}.[7]

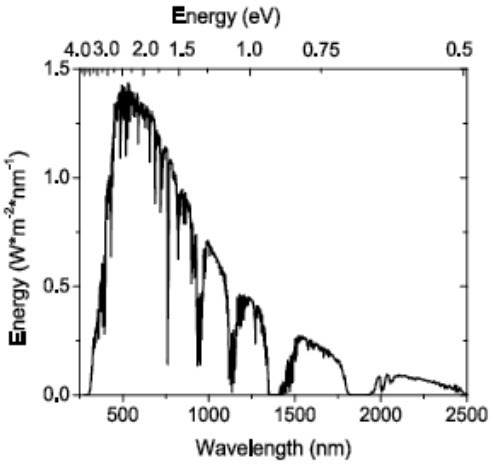

Figure 1.4: The AM1.5G spectrum.[8]

In the photovoltaic field two measurement techniques are usually performed to estimate the performance of an OPV device, a current-voltage measurement and an external quantum efficiency measurement. A current-voltage (*I-V*) measurement is used to determine several key performance parameters. These parameters can be determined by connecting the electrodes of the cell and recording the current while sweeping a voltage over the device, both in the dark and under AM1.5G illumination conditions. While it might seem odd to measure a photovoltaic device in the dark it provides a lot of information, for example about possible shorts and diode properties.[59,60] In the dark, the device behaves like a diode. Under reverse bias in the dark the energy barrier increases, causing drift current to prevail over diffusion current, allowing only a small leakage current to pass.[60,61] The energy barrier decreases when a forward

bias is applied, and when the applied voltage exceeds the built-in voltage set by the contacts a large diffusion current can be passed. When the cell is illuminated, the photoexcited charge carriers cause the *I-V* curve to shift down. Now the three key performance parameters can be determined, namely the short-circuit current (I_{sc}), the open-circuit voltage (V_{oc}) and the fill-factor (FF). The short-circuit current is the current that flows through the shorted circuit when zero voltage is applied. This is the maximum current a solar cell can deliver and depends on the optical and morphological properties of the solar cell.[62] Because the current also depends on the incident photon flux and the cell area, the *I-V* measurements are performed under standardized light and the current is described as a current density making that the short-circuit current becomes the short-circuit current-density (J_{sc}). The open-circuit voltage is the voltage at which no current flows through the circuit. The V_{oc} depends on the recombination dependent reverse saturation current and is therefore also a measure for the amount of recombination in the solar cell.[62] The last key performance parameter, the fill-factor, contains information of all the processes involved in charge recombination, transport and collection. Therefore, it is greatly influenced by the morphology of the active layer, which is sensitive to changes as described in section 3.2.[63] The FF is the ratio between the maximum power point of the *J-V* curve ($P_{max} = J_{mmp} V_{mmp}$) and the product of the V_{oc} and J_{sc} and thus represents the squareness of the *J-V* curve.[60,62] A typical *J-V* curve is depicted in **Figure 1.5a**.

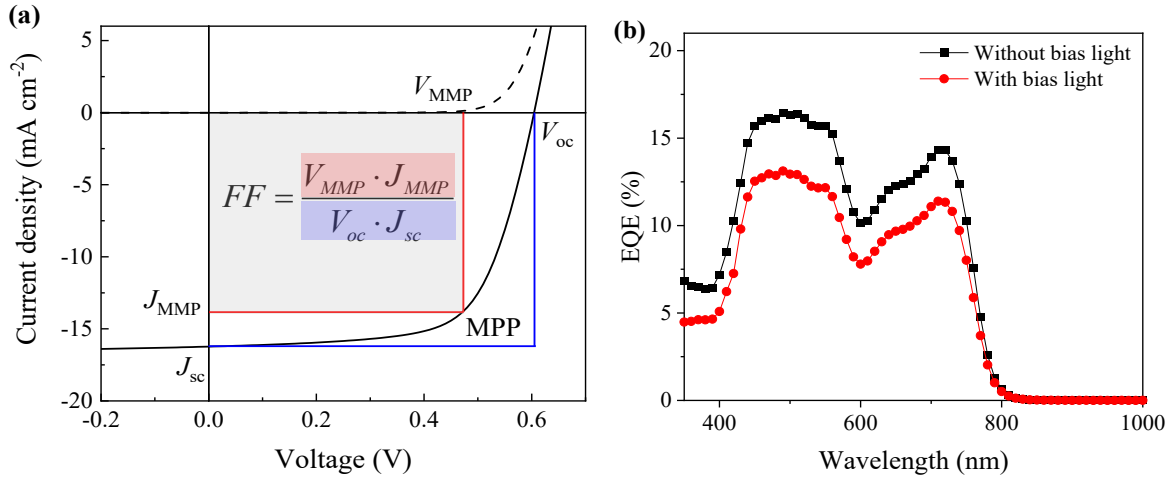

Figure 1.5: (a) A characteristic *J-V* curve, in the dark (dashed line) and under AM1.5G illumination (solid line) with all characterization parameters. (b) A typical EQE spectrum under different light intensities.

The power conversion efficiency (PCE) is now determined by the ratio of the maximum attainable power and the incident power. A typical *J-V* measurement is performed under AM1.5G conditions and thus has an incident power of 1000 W m^{-2}.

$$PCE = \frac{P_{max}}{P_{in}} = \frac{J_{sc} \cdot V_{oc} \cdot FF}{P_{in}}$$

The second device characterization method is an external quantum efficiency (EQE) measurement. During this measurement the ratio of collected charge carriers over the number of incident photons is determined.[64] In other words, the measurement provides information about the efficiency of all photoconversion processes in a solar cell. EQE spectra (**Figure 1.5b**) are always collected under at least two light intensity conditions. A higher light intensity causes an increased charge creation, but consequently also an increased bi-molecular recombination. Since a higher light intensity is closer to the actual solar light intensity this light biased measurement allows for a more accurate determination of the short circuit current.[60,65] The short-circuit current density can be determined using the following integral:

$$J_{sc} = q\int_0^\infty EQE(\lambda)\cdot\phi_{ph}(\lambda)d\lambda$$

where $\phi_{ph}(\lambda)$ is the incident photon flux. With this J_{sc}, a more exact PCE can be determined.

A crucial factor in limiting the PCE of OPV devices has been attributed to significant energy losses.[66]

$$E_{loss} = E_g - eV_{oc}$$

As can be seen in **Figure 1.6**, the energy losses can be divided into two contributions, one from the energy offsets necessary for charge generation and the other from fundamental recombination, both limiting the V_{oc}. The V_{oc} is largely determined by the energy offset between the LUMO of the acceptor and the HOMO of the donor (the charge transfer energy E_{CT}), as shown in the equation below.[67] The factor 0.3 in this equation is the radiative limit as found in de detailed balance analysis of Shockley and Queisser.[19,68]

$$V_{oc} \approx \frac{1}{e}(\left|E_H^D\right| - \left|E_L^A\right|) - 0.3$$

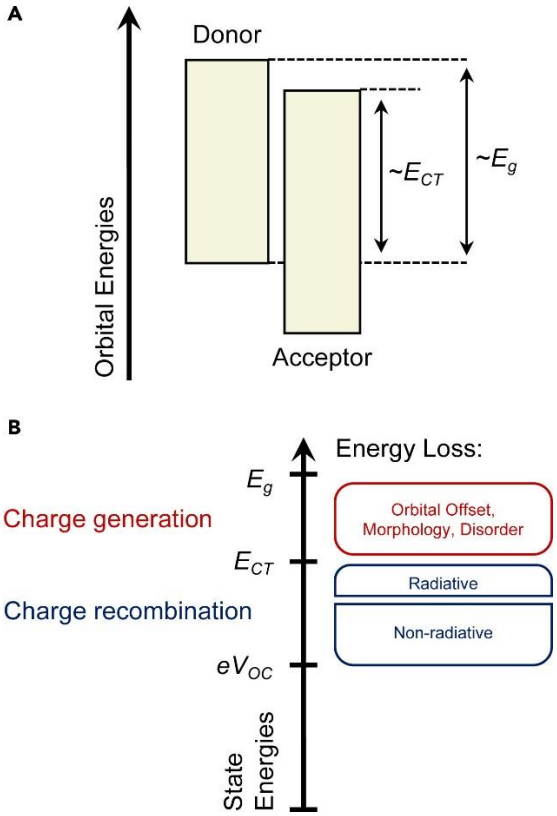

Figure 1.6: (a) Schematic representation of an energy diagram showing the donor and acceptor energies, their respective bandgaps (E_g) and the charge transfer energy (E_{CT}). (b) Energy losses in an OPV, separated as losses incurred during charge generation (E_g-E_{CT}) and during charge recombination (E_{CT}-eV_{oc}).[68]

6. Transition from fullerene to non-fullerene acceptors

While both donor and acceptor molecules are important for an efficiently working solar cell, past research has mainly focused on finding a more effective donor. Owing to their attractive optoelectronic properties, fullerene-based materials such as (6,6)-phenyl-C_{61}-butyric acid methyl ester ([60]PCBM) (**Figure 1.7**) or (6,6)-phenyl-C_{71}-butyric acid methyl ester ([70]PCBM) have long been the standard acceptor in OPV devices. The 3D conjugated structure of the fullerene molecules causes the LUMOs to be delocalized over the entire surface, allowing for highly isotropic electron mobilities and electron

affinities. This delocalization also allows for weak π-π interactions between the molecules, such that the BHJ domains are highly dispersed and have a length scale similar to the exciton diffusion length.[33,69–71] Careful optimization of fullerene-based devices has led to efficiencies around 10%.[72–74] Despite the aforementioned highly attractive properties of fullerene-based acceptors, there are certain drawbacks that limit further device optimization. First, the fullerene acceptors exhibit a weak absorption in the visible and near-infrared region of the solar spectrum. Secondly, there is little opportunity for synthetic alterations of the molecule, limiting the variation of the energy levels. Lastly, the strong aggregation tendency of fullerenes causes long-term device stability issues and high synthetic costs limit commercialization of these type of OPV devices.[69,71,75]

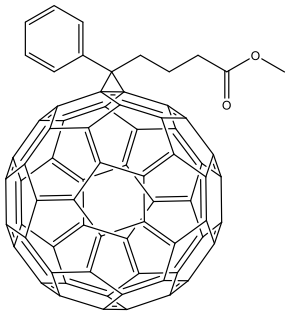

Figure 1.7: Chemical structure of [60]PCBM

Over the past years, there has been a rapid and impressive progress in non-fullerene acceptor (NFA) based devices. These NFAs overcome the limitations of fullerene acceptors, mainly because of their higher synthetic flexibility. Their tunable bandgaps allow for higher absorption in the NIR region, their tunable energy levels allow for suitable energy offsets, *i.e.* a higher V_{oc}, and their tunable planarity and crystallinity allow for control over the active layer morphology and improved device stability.[75,76] During the early stages of the development of NFAs, NFAs based on multiple different structures have been reported. These structures include: perylene diimide (PDI),[77,78] naphthalene diimide (NDI)[79,80] and benzothiadiazole (BT).[81,82] Although OPV devices based on these NFAs did not outperform fullerene based devices, they were a gateway into the potential of non-fullerene acceptors.[75]

6.1 Molecular design of non-fullerene acceptors

NFAs based on the acceptor-donor-acceptor (A-D-A) structure have shown to be the most promising in terms of photovoltaic performance. In this design, an electron rich core (D) is flanked by two electron deficient units (A), which are usually coupled through a vinyl bridge (**Figure 1.8**). This design makes use of the so called push-pull hybridization, enabling the NFA to absorb strongly in the visible range.[71,75,83] Another advantage of the A-D-A structure is that its design is modular, meaning that tuning of the energy levels and absorption spectra can easily be achieved by varying either the donor or the acceptor unit. Since the LUMO is mainly situated on the A units and the HOMO is mainly located on the D unit, the frontier molecular orbital energies can individually be altered.[71]

6.1.1 Choice of the acceptor unit

Many different acceptor end-groups have been reported, which are typically coupled to the D unit via a synthetically simple Knoevenagel condensation.[84] By adjusting the nature of the A units and the side-chains attached to them, proper energy level alignment (mainly due to an adjusted LUMO), molecular packing and solubility can be achieved.[85] The molecular packing in NFAs is important for charge transport as is shown in the work of Han *et al.*, who found that π-π stacking of the terminal groups is a key parameter to achieve three-dimensional charge transport.[86] This shows that the choice of the acceptor unit in A-D-A type NFAs is critical for achieving high performance OPV devices. The most widely reported terminating acceptor groups are depicted in **Figure 1.8**. In NFAs based on rhodanine derivates (Rh), the solubility and aggregation behavior can be varied through different alkyl side-chains. On the other hand, the energy levels and also the aggregation behavior can be altered through

substitution of the carbonyl group for a malononitrile group, because the malononitrile group lies out-of-plane and extends the π-conjugation.[84,87] The decreased molecular packing caused by the malononitrile group has shown to counteract the excessive aggregation often found in A-D-A type NFAs.[88] Another widely used terminating group is the 1,3-indandione (IN) family and its malononitrile substituted counterpart 1,1-dicyanomethylene-3-indanone (INCN). Molecular alterations within this family are easily achieved, which allows for better compatibility with the donor molecule. Examples of published high performing INCN alterations are the addition of halogen atoms,[89] or the extension of the π-conjugated system by changing to a naphthyl-fused indanone. The latter alteration has shown to enhance charge separation efficiency through an increased interaction between the donor and the acceptor molecule.[90] Diketopyrrolopyrrole (DPP) is an electron deficient group, commonly known in the photovoltaic world as a building block in polymer donors. Their strong electron withdrawing character has made them interesting for use as terminating acceptor group in A-D-A type NFAs.[76]

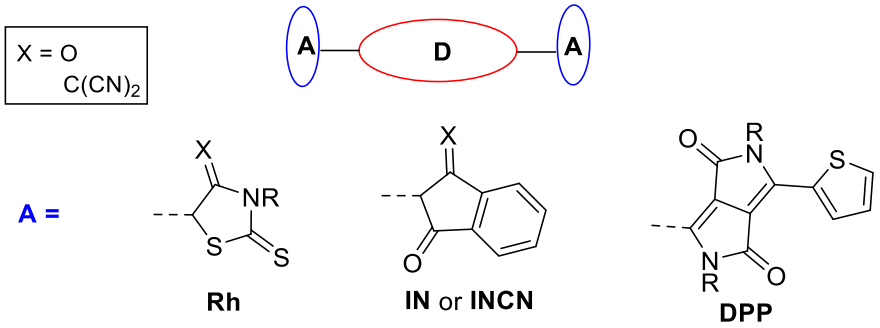

Figure 1.8: Design motif of A-D-A type non-fullerene acceptors with the chemical structures of different acceptor unit end-groups

6.1.2 Different non-fullerene acceptor families

One well-known family of NFAs is the ITIC family. This molecule (**Figure 1.9a**) is composed of a rigid indacenodithieno[3,2-*b*]thiophene (IDTT) core, flanked by two INCN groups. In 2015, Lin *et al.* reported a record breaking 6.8% fullerene-free device with ITIC blended with poly[4,8-bis(5-(2-ethylhexyl)thiophen-2-yl)benzo[1,2-*b*;4,5-*b*′]dithiophene-2,6-diyl-alt-(4-(2-ethylhexyl)-3-fluorothieno[3,4-b]thiophene-)-2-carboxylate-2-6-diyl)] (PTB7-Th) as the donor polymer.[91] More reports on high performance NFAs based on ITIC blended with other polymer donors quickly followed. Just two years later, Zhoa *et al.* reported a blend of IT-4F, ITIC with fluorine atoms on its end groups, and poly[(2,6-(4,8-bis(5-(2-ethylhexyl-3-fluoro)thiophen-2-yl)-benzo[1,2-*b*:4,5-*b*′]dithiophene))-alt-(5,5-(1′,3′-di-2-thienyl-5′,7′-bis(2-ethylhexyl)benzo[1′,2′-*c*:4′,5′-c′]dithiophene-4,8-dione)] (PM6) achieving a PCE of 13.3%.[92]

A second family of NFAs based on the A-D-A structure is the IDTBR family (**Figure 1.9b**). A striking difference between the ITIC and the IDTBR family is that IDTBR is built up out of 2 different acceptor units, benzothiadiazole and rhodanine, at either end of the indacenodithiophene core. The two most widely established NFAs in the IDTBR family are EH-IDTBR and O-IDTBR. These molecules are branched with 2'-ethylhexyl and *n*-octyl side-chains respectively. Of these two molecules the O-IDTBR is more crystalline and shows a slight red-shifted absorption compared to EH-IDTBR.[83]

One of the more recent and most impressive NFA families is the so-called Y-series. In 2019, Yuan *et al.* reported a record-breaking 15.7% efficiency for Y6 (**Figure 1.9c**) blended with PM6 as donor polymer.[93] The Y-series has a remarkably different design motif compared to the other high performance non-fullerene acceptors. It has an electron deficient benzothiadiazole (BT) in the core and thus has the so-called A-D-A'-D-A design motif. The addition of the BT unit in the core gives the molecule an angular structure, which causes a steric repulsion between the two alkyl chains on the pyrrole rings. Due to the repulsion there is a twist in the molecule, which allows the molecule to pack in a unique 3D network. This 3D network allows for highly efficient charge transport and is therefore a reason for the

high performance found in OPV devices composed of these type of NFAs.[88] In 2020, the highest single-junction OPV efficiency to date (18.22%) was reported for a blend of Y6 and poly[(2,6-(4,8-bis(5-(2-ethylhexyl-3-fluoro)thiophen-2-yl)-benzo[1,2-b:4,5-b']dithiophene))-alt-5,5'-(5,8-bis(4-(2-butyloctyl)thiophen-2-yl)dithieno[3',2':3,4;2",3":5,6]benzo[1,2-c][1,2,5]thiadiazole)] (D18).[94]

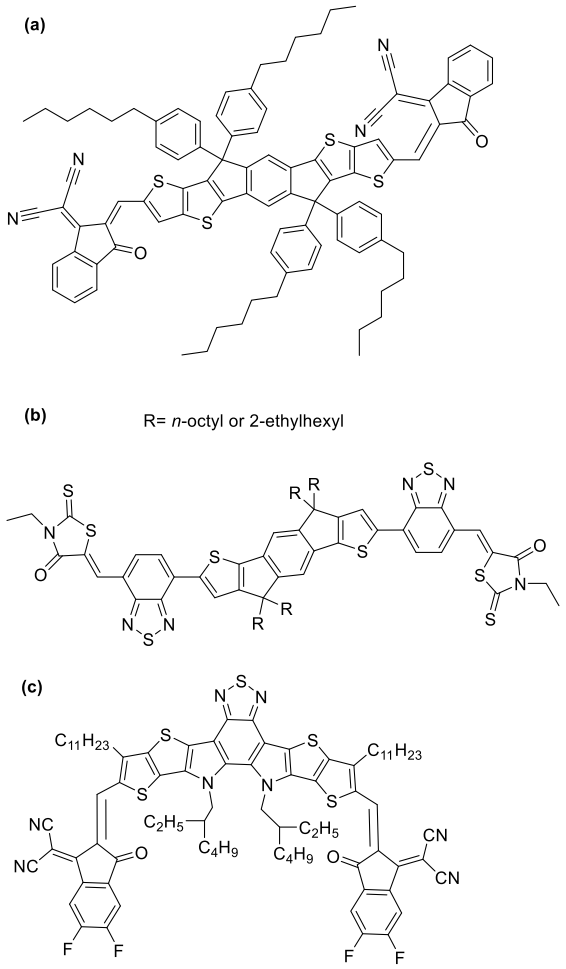

Figure 1.9: Chemical structures of (a) ITIC, (b) IDTBR and (c) Y6

6.1.3 Simple non-fullerene acceptors

Although the aforementioned A-D-A or A-D-A'-D-A type NFAs show impressive PCEs, the core of these molecules is composed of highly extended fused-ring networks. These networks require multistep synthesis reactions which result in high synthesis costs and therefore might limit commercialization. To reduce synthetic costs, research on unfused ring acceptors has gained attention. In 2017, Li *et al.* reported an unfused ring acceptor with a core composed of two cyclopentadithiophene moieties and a 2,5-difluorobenzene group. For a blend of this NFA with PBDB-T as donor they showed a 10.14% device effiency.[95] Although synthesis of this molecule is still reasonably complex, its performance demonstrates the potential of these non-fused acceptors.

To further reduce the synthetic complexity Li *et al.* showed a simple unfused NFA, prepared *via* three synthetic steps. Their NFA, an alkyl substituted 2,2'-bithiophene flanked by two INCN groups, adhered to the A-D-A structure and showed a 2.4% efficiency.[96] Not much later Lee *et al.* published a paper about a 2,2'-bithiophene flanked by two octyl *N*-functionalized rhodanine units (**2T-ORh**), with a promising efficiency of 9.3%.[97] Due to the relatively short π-conjugation in these simple NFAs, a low bandgap polymer such as PTB7-Th can be used as the complementary donor material.

6.2 Important non-fullerene specific design and operating principles

Due to the long dominance of fullerene acceptors (FAs) in the OPV world there are certain operating and design principles which are adopted without question, but are in fact different in non-fullerene based OPV devices.

The first thing to consider when constructing devices with a new NFA is the choice of an appropriate donor material. Previously, new donor materials were designed to match with fullerene as acceptor, which provided a one-to-one point of comparison. With a newly designed NFA there is no universal donor to blend it with as a point of reference. Besides the obvious optical and electrochemical requirements for a donor, *i.e.* complementary absorption and adequate energy level alignment, crystallinity and morphology also play a major role in determining the device performance. Where it is often found that a highly crystalline donor works well with rather amorphous FAs, a poorer performance is usually achieved when the same donor is blended with NFAs, which are usually also quite crystalline.[98,99]

One major difference between FAs and low bandgap NFAs is the higher absorption for these NFAs in the visible range. This absorption allows for hole energy transfer from the acceptor to the donor, also called channel II photocurrent generation,[71] indicating that also a sufficient HOMO-HOMO offset is important for charge generation. This is the opposite of FA based OPVs, where it is believed that the HOMO-HOMO offset is relatively unimportant. Another difference is the extend of offset needed for sufficient charge separation. In FA based OPV devices it is generally believed that a 0.3 eV offset is necessary for charge separation.[67] However, in OPV devices employing NFAs efficient charge separation has repeatedly been found while the energy offsets were extremely small.[100] The exact nature of this is still speculated on. Tu *et al*. proposed that the separated charges are stabilized through the larger electronic polarization in the bulk of A-D-A type NFAs. Through these stabilized charges, the charge separation is aided.[101] Classen *et al.* found that the exciton lifetime is remarkably larger in NFAs and that this increased lifetime is a key parameter in maintaining an efficient charge separation.[102] Another possible explanation was reported by Neher and coworkers, who found that a quadrupole is formed at the interface between donor crystallites and A-D-A type NFA crystallites. This quadrupole may give rise to an electrostatic field, which can repel charges from the interface and thereby encourages charge separation.[103]

Another major difference between FAs and NFAs is their aggregation behavior and how it relates to charge transport. In conjugated materials, the charge mobility is affected by the π-π stacking intensity. The fact that FAs form closely packed domains and have a 3D conjugated nature allows for isotropic charge transport in all directions.[104] In contrast, in NFAs there is no such 3D nature which results in anisotropic charge transport. The A-D-A type NFAs can aggregate in multiple ways, which are depicted in **Figure 1.10**. A distinction between the presence of H- and J-aggregates can be made using absorption spectroscopy, where the difference in Coulomb coupling causes a red-shifted absorption for the J-aggregates and a blue-shifted absorption for the H-aggregates relative to the monomer absorption.[105] The two types of J-aggregates are often found to co-exist, which offers multiple pathways for efficient exciton and electron transport and leads to higher mobilities.[106] This observation and the lower energy needed to excite the J-aggregates has led to the believe that having NFAs with only J-type aggregation is the most favorable. However, Li *et al.* showed the advantage of a combination between H- and J-aggregates on the broadness of the absorption spectrum.[107] Furthermore, Lai and co-workers found that the cooperation between H- and J-aggregates led to a 3D interpenetrating network.[108]

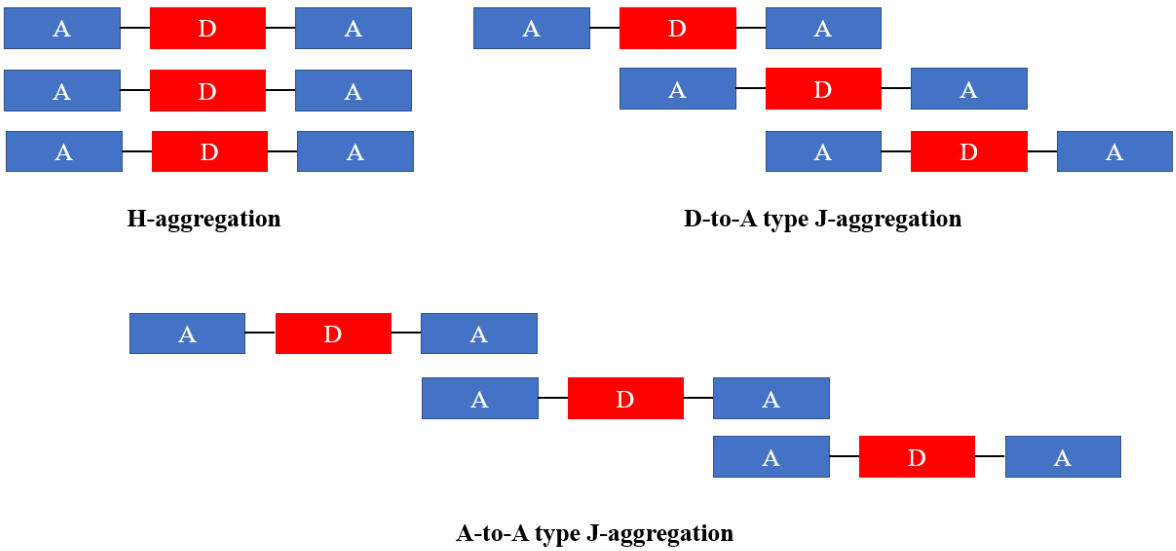

Figure 1.10: Schematic representation of the different aggregation types found in A-D-A type non-fullerene acceptors.

7. Project goal

Paragraph 6.1 described the impressive and fast evolution of the power conversion efficiencies found in BHJ photovoltaic devices incorporating non-fullerene acceptors in the active layer. Unfused NFAs hold a great promise for commercialization due to their simple synthesis.

This thesis aims to develop deeper insight into how structural changes in simple non-fullerene acceptors with *N*-functionalized rhodanine as the acceptor unit affect their optoelectronic properties and photovoltaic performance. In particular, this work focuses on: 1) the effect of side-chain engineering in the acceptor unit (***Chapter 2***) and 2) the effect of engineering of the donor unit (***Chapter 3***). Based on the good performance of the **2T-ORh** NFA,[97] this NFA will be used as the starting point for and as the reference material in this work. All the synthesized non-fullerene acceptors will be blended with PTB7-Th as the donor polymer and can therefore be compared one-on-one.

8. References

(1) Dahlman, R. Climate Change: Global Temperature https://www.climate.gov/news-features/understanding-climate/climate-change-global-temperature (accessed April 5, 2021).
(2) Goddard Institute for Space Studies. Global Temperature. In *Van Nostrand's Scientific Encyclopedia*; American Cancer Society, 2005.
(3) NASA. Global Climate Change, vital signs of the planet https://climate.nasa.gov/causes/#no1 (accessed May 20, 2020).
(4) EPA. Sources of Greenhouse Gas Emissions https://www.epa.gov/ghgemissions/sources-greenhouse-gas-emissions (accessed May 20, 2020).
(5) Eurostat. Renewable energy statistics https://ec.europa.eu/eurostat/statistics-explained/index.php/Renewable_energy_statistics#Renewable_energy_produced_in_the_EU_increased_by_two_thirds_in_2007-2017 (accessed May 20, 2020).
(6) European Scientist. The nearby depletion of fossil fuels will force to hasten the energy transition https://www.europeanscientist.com/en/features/nearby-fossil-fuel-depletion/ (accessed May 20, 2020).
(7) Lewis, N. .; Crabtree, G. W. Basic Research needs for Solar Energy Utilization: report of the basic energy workshop on solar energy utilization

https://science.osti.gov/~/media/bes/pdf/reports/files/Basic_Research_Needs_for_Solar_Energy_Utilization_rpt.pdf (accessed May 20, 2020).
(8) Bijleveld, J. C. Synthesis and Application of Pi-Conjugated Polymers for Organic Solar Cells, Eindhoven University of Technology, 2010.
(9) GreenMatch. Solar Panels vs Solar Thermal. A closer look at Solar Thermal and Solar PV and their advantages and disadvantages. https://www.greenmatch.co.uk/blog/2015/04/solar-panels-vs-solar-thermal (accessed May 20, 2020).
(10) Bagnall, D. M.; Boreland, M. Photovoltaic Technologies. *Energy Policy* **2008**, *36* (12), 4390–4396.
(11) Ranabhat, K.; Patrikeev, L.; Revina, A. A. evna; Andrianov, K.; Lapshinsky, V.; Sofronova, E. An Introduction to Solar Cell Technology. *J. Appl. Eng. Sci.* **2016**, *14* (4), 481–491.
(12) Kibria, M.; Ahammed, A.; Sonyy, S.; Sony, F.; Hossain, S.-U.-I. A Review: Comparative Studies on Different Generation Solar Cells Technology; 2014.
(13) Glunz, S. W.; Preu, R.; Biro, D. Crystalline Silicon Solar Cells. State-of-the-Art and Future Developments. In *Comprehensive Renewable Energy*; Sayigh, A. B. T.-C. R. E., Ed.; Elsevier: Oxford, 2012; Vol. 1, pp 353–387.
(14) Saga, T. Advances in Crystalline Silicon Solar Cell Technology for Industrial Mass Production. *NPG Asia Mater.* **2010**, *2* (3), 96–102.
(15) The National Renewable Energy Laboratory. Solar Manufacturing Cost Analysis https://www.nrel.gov/solar/solar-manufacturing-cost.html (accessed Jan 9, 2021).
(16) Andreani, L. C.; Bozzola, A.; Kowalczewski, P.; Liscidini, M.; Redorici, L. Silicon Solar Cells: Toward the Efficiency Limits. *Adv. Phys. X* **2019**, *4* (1), 1548305.
(17) Chopra, K. L.; Paulson, P. D.; Dutta, V. Thin-Film Solar Cells: An Overview. *Prog. Photovoltaics Res. Appl.* **2004**, *12* (2-3), 69–92.
(18) Conibeer, G. Third-Generation Photovoltaics. *Mater. Today* **2007**, *10* (11), 42–50.
(19) Shockley, W.; Queisser, H. J. Detailed Balance Limit of Efficiency of P-n Junction Solar Cells. *J. Appl. Phys.* **1961**, *32* (3), 510–519.
(20) Chen, F.-C. Organic Semiconductors; Guenther, B. D., Steel, D. G. B. T.-E. of M. O. (Second E., Eds.; Elsevier: Oxford, 2018; pp 220–231.
(21) Chiang, C. K.; Fincher, C. R.; Park, Y. W.; Heeger, A. J.; Shirakawa, H.; Louis, E. J.; Gau, S. C.; MacDiarmid, A. G. Electrical Conductivity in Doped Polyacetylene. *Phys. Rev. Lett.* **1977**, *39* (17), 1098–1101.
(22) Brutting, W. Organic Semiconductors https://assets.uni-augsburg.de/media/filer_public/27/2f/272ffc1c-a7b5-4934-b7ff-18df9cdecefc/organicsemiconductors.pdf (accessed Jun 11, 2020).
(23) Brabec, C. J. Organic Photovoltaics: Technology and Market. *Sol. Energy Mater. Sol. Cells* **2004**, *83* (2), 273–292.
(24) Søndergaard, R. R.; Hösel, M.; Krebs, F. C. Roll-to-Roll Fabrication of Large Area Functional Organic Materials. *J. Polym. Sci. Part B Polym. Phys.* **2013**, *51* (1), 16–34.
(25) Kearns, D.; Calvin, M. Photovoltaic Effect and Photoconductivity in Laminated Organic Systems. *J. Chem. Phys.* **1958**, *29* (4), 950–951.
(26) Tang, C. W. Two-layer Organic Photovoltaic Cell. *Appl. Phys. Lett.* **1986**, *48* (2), 183–185.
(27) Knupfer, M. Exciton Binding Energies in Organic Semiconductors. *Appl. Phys. A* **2003**, *77* (5), 623–626.
(28) Kippelen, B.; Brédas, J.-L. Organic Photovoltaics. *Energy Environ. Sci.* **2009**, *2* (3), 251–261.
(29) Hoppe, H.; Sariciftci, N. S. Organic Solar Cells: An Overview. *J. Mater. Res.* **2004**, *19* (7), 1924–1945.
(30) Hayase, S. Organic Solar Cells BT - Organic Electronics Materials and Devices; Ogawa, S., Ed.; Springer Japan: Tokyo, 2015; pp 75–100.
(31) Group, M. R. Organic solar cells at M2N https://www.m2ngroup.nl/research/research_programs/organicsolarcells/ (accessed Mar 10, 2021).
(32) Hiramoto, M.; Fujiwara, H.; Yokoyama, M. Three-layered Organic Solar Cell with a Photoactive Interlayer of Codeposited Pigments. *Appl. Phys. Lett.* **1991**, *58* (10), 1062–1064.
(33) Roncali, J. Molecular Bulk Heterojunctions: An Emerging Approach to Organic Solar Cells.

Acc. Chem. Res. **2009**, *42* (11), 1719–1730.
(34) Hendriks, K. H. Diketopyrrolopyrrolle Polymers for Efficient Organic Solar Cells, Eindhoven University of Technology, 2014.
(35) Scharber, M. C.; Sariciftci, N. S. Efficiency of Bulk-Heterojunction Organic Solar Cells. *Prog. Polym. Sci.* **2013**, *38* (12), 1929–1940.
(36) Yoshikawa, S.; Saeki, A.; Saito, M.; Osaka, I.; Seki, S. On the Role of Local Charge Carrier Mobility in the Charge Separation Mechanism of Organic Photovoltaics. *Phys. Chem. Chem. Phys.* **2015**, *17* (27), 17778–17784.
(37) Scholes, D. T.; Yee, P. Y.; Lindemuth, J. R.; Kang, H.; Onorato, J.; Ghosh, R.; Luscombe, C. K.; Spano, F. C.; Tolbert, S. H.; Schwartz, B. J. The Effects of Crystallinity on Charge Transport and the Structure of Sequentially Processed F4TCNQ-Doped Conjugated Polymer Films. *Adv. Funct. Mater.* **2017**, *27* (44), 1702654.
(38) McDowell, C.; Abdelsamie, M.; Toney, M. F.; Bazan, G. C. Solvent Additives: Key Morphology-Directing Agents for Solution-Processed Organic Solar Cells. *Adv. Mater.* **2018**, *30* (33), 1707114.
(39) Kim, Y. S.; Lee, Y.; Kim, J. K.; Seo, E.-O.; Lee, E.-W.; Lee, W.; Han, S.-H.; Lee, S.-H. Effect of Solvents on the Performance and Morphology of Polymer Photovoltaic Devices. *Curr. Appl. Phys.* **2010**, *10* (4), 985–989.
(40) Liu, X.; Huettner, S.; Rong, Z.; Sommer, M.; Friend, R. H. Solvent Additive Control of Morphology and Crystallization in Semiconducting Polymer Blends. *Adv. Mater.* **2012**, *24* (5), 669–674.
(41) van Franeker, J. J.; Turbiez, M.; Li, W.; Wienk, M. M.; Janssen, R. A. J. A Real-Time Study of the Benefits of Co-Solvents in Polymer Solar Cell Processing. *Nat. Commun.* **2015**, *6* (1), 6229.
(42) Hau, S. K.; O'Malley, K. M.; Cheng, Y.-J.; Yip, H.-L.; Ma, H.; Jen, A. K.-Y. Optimization of Active Layer and Anode Electrode for High-Performance Inverted Bulk-Heterojunction Solar Cells. *IEEE J. Sel. Top. Quantum Electron.* **2010**, *16* (6), 1665–1675.
(43) Savikhin, V.; Jagadamma, L. K.; Purvis, L. J.; Robertson, I.; Oosterhout, S. D.; Douglas, C. J.; Samuel, I. D. W.; Toney, M. F. Morphological, Chemical, and Electronic Changes of the Conjugated Polymer PTB7 with Thermal Annealing. *iScience* **2018**, *2*, 182–192.
(44) Jin, F.; Ding, G.; Wang, Y.; Yuan, J.; Guo, W.; Yuan, H.; Sheng, C.; Ma, W.; Zhao, H. Thermal Annealing Effect on Ultrafast Charge Transfer in All-Polymer Solar Cells with a Non-Fullerene Acceptor N2200. *J. Phys. Chem. C* **2017**, *121* (16), 8804–8811.
(45) Köntges, W.; Perkhun, P.; Kammerer, J.; Alkarsifi, R.; Würfel, U.; Margeat, O.; Videlot-Ackermann, C.; Simon, J.-J.; Schröder, R. R.; Ackermann, J.; Pfannmöller, M. Visualizing Morphological Principles for Efficient Photocurrent Generation in Organic Non-Fullerene Acceptor Blends. *Energy Environ. Sci.* **2020**, *13* (4), 1259–1268.
(46) S. Gurney, R.; Li, W.; Yan, Y.; Liu, D.; J. Pearson, A.; Wang, T. Morphology and Efficiency Enhancements of PTB7-Th:ITIC Nonfullerene Organic Solar Cells Processed via Solvent Vapor Annealing. *J. Energy Chem.* **2019**, *37*, 148–156.
(47) Miller, S.; Fanchini, G.; Lin, Y.-Y.; Li, C.; Chen, C.-W.; Su, W.-F.; Chhowalla, M. Investigation of Nanoscale Morphological Changes in Organic Photovoltaics during Solvent Vapor Annealing. *J. Mater. Chem.* **2008**, *18* (3), 306–312.
(48) Sun, K.; Xiao, Z.; Hanssen, E.; Klein, M. F. G.; Dam, H. H.; Pfaff, M.; Gerthsen, D.; Wong, W. W. H.; Jones, D. J. The Role of Solvent Vapor Annealing in Highly Efficient Air-Processed Small Molecule Solar Cells. *J. Mater. Chem. A* **2014**, *2* (24), 9048–9054.
(49) Li, G.; Zhu, R.; Yang, Y. Polymer Solar Cells. *Nat. Photonics* **2012**, *6* (3), 153–161.
(50) Kim, H.; Gilmore, C. M.; Piqué, A.; Horwitz, J. S.; Mattoussi, H.; Murata, H.; Kafafi, Z. H.; Chrisey, D. B. Electrical, Optical, and Structural Properties of Indium–Tin–Oxide Thin Films for Organic Light-Emitting Devices. *J. Appl. Phys.* **1999**, *86* (11), 6451–6461.
(51) Eo, Y. S.; Rhee, H. W.; Chin, B. D.; Yu, J.-W. Influence of Metal Cathode for Organic Photovoltaic Device Performance. *Synth. Met.* **2009**, *159* (17), 1910–1913.
(52) Chen, L.-M.; Hong, Z.; Li, G.; Yang, Y. Recent Progress in Polymer Solar Cells: Manipulation of Polymer:Fullerene Morphology and the Formation of Efficient Inverted Polymer Solar Cells. *Adv. Mater.* **2009**, *21* (14-15), 1434–1449.

(53) Cameron, J.; Skabara, P. J. The Damaging Effects of the Acidity in PEDOT:PSS on Semiconductor Device Performance and Solutions Based on Non-Acidic Alternatives. *Mater. Horiz.* **2020**, *7* (7), 1759–1772.
(54) Yi, C.; Hu, X.; Gong, X.; Elzatahry, A. Interfacial Engineering for High Performance Organic Photovoltaics. *Mater. Today* **2016**, *19* (3), 169–177.
(55) Gonzalez-Valls, I.; Lira-Cantu, M. Vertically-Aligned Nanostructures of ZnO for Excitonic Solar Cells: A Review. *Energy Environ. Sci.* **2009**, *2* (1), 19–34.
(56) Yu, H.; Huang, X.; Huang, C. PEIE Doped ZnO as a Tunable Cathode Interlayer for Efficient Polymer Solar Cells. *Appl. Surf. Sci.* **2019**, *470*, 318–330.
(57) Li, P.; Wang, G.; Cai, L.; Ding, B.; Zhou, D.; Hu, Y.; Zhang, Y.; Xiang, J.; Wan, K.; Chen, L.; Alameh, K.; Song, Q. High-Efficiency Inverted Polymer Solar Cells Controlled by the Thickness of Polyethylenimine Ethoxylated (PEIE) Interfacial Layers. *Phys. Chem. Chem. Phys.* **2014**, *16* (43), 23792–23799.
(58) Li, P.; Cai, L.; Wang, G.; Zhou, D. C.; Xiang, J.; Zhang, Y. J.; Ding, B. F.; Alameh, K.; Song, Q. L. PEIE Capped ZnO as Cathode Buffer Layer with Enhanced Charge Transfer Ability for High Efficiency Polymer Solar Cells. *Synth. Met.* **2015**, *203*, 243–248.
(59) PV Education. Dark IV Measurements https://www.pveducation.org/pvcdrom/characterisation/dark-iv-measurements (accessed Aug 21, 2020).
(60) Bisquert, J. *The Physics of Solar Cells*; CRC Press: Boca Raton, 2018.
(61) Kitai, A. Principles of Solar Cells, LEDs and Diodes: The Role of the PN Junction. August 11, 2011, pp i–xiv.
(62) Smets, A.; Jäger, K.; Isabella, O.; van Swaaij, R.; Zeman, M. *Solar Energy*; Cambridge UIT.
(63) Etxebarria, I.; Ajuria, J.; Pacios, R. Solution-Processable Polymeric Solar Cells: A Review on Materials, Strategies and Cell Architectures to Overcome 10%. *Org. Electron.* **2015**, *19*, 34–60.
(64) Ananda, W. External Quantum Efficiency Measurement of Solar Cell. In *2017 15th International Conference on Quality in Research (QiR) : International Symposium on Electrical and Computer Engineering*; 2017; pp 450–456.
(65) Cowan, S. R.; Wang, J.; Yi, J.; Lee, Y.-J.; Olson, D. C.; Hsu, J. W. P. Intensity and Wavelength Dependence of Bimolecular Recombination in P3HT:PCBM Solar Cells: A White-Light Biased External Quantum Efficiency Study. *J. Appl. Phys.* **2013**, *113* (15), 154504.
(66) Ji, Y.; Xu, L.; Hao, X.; Gao, K. Energy Loss in Organic Solar Cells: Mechanisms, Strategies, and Prospects. *Sol. RRL* **2020**, *4* (7), 2000130.
(67) Scharber, M. C.; Mühlbacher, D.; Koppe, M.; Denk, P.; Waldauf, C.; Heeger, A. J.; Brabec, C. J. Design Rules for Donors in Bulk-Heterojunction Solar Cells—Towards 10 % Energy-Conversion Efficiency. *Adv. Mater.* **2006**, *18* (6), 789–794.
(68) Menke, S. M.; Ran, N. A.; Bazan, G. C.; Friend, R. H. Understanding Energy Loss in Organic Solar Cells: Toward a New Efficiency Regime. *Joule* **2018**, *2* (1), 25–35.
(69) Speller, E. M.; Clarke, A. J.; Luke, J.; Lee, H. K. H.; Durrant, J. R.; Li, N.; Wang, T.; Wong, H. C.; Kim, J.-S.; Tsoi, W. C.; Li, Z. From Fullerene Acceptors to Non-Fullerene Acceptors: Prospects and Challenges in the Stability of Organic Solar Cells. *J. Mater. Chem. A* **2019**, *7* (41), 23361–23377.
(70) Liu, T.; Troisi, A. What Makes Fullerene Acceptors Special as Electron Acceptors in Organic Solar Cells and How to Replace Them. *Adv. Mater.* **2013**, *25* (7), 1038–1041.
(71) Wadsworth, A.; Moser, M.; Marks, A.; Little, M. S.; Gasparini, N.; Brabec, C. J.; Baran, D.; McCulloch, I. Critical Review of the Molecular Design Progress in Non-Fullerene Electron Acceptors towards Commercially Viable Organic Solar Cells. *Chem. Soc. Rev.* **2019**, *48* (6), 1596–1625.
(72) He, Z.; Xiao, B.; Liu, F.; Wu, H.; Yang, Y.; Xiao, S.; Wang, C.; Russell, T. P.; Cao, Y. Single-Junction Polymer Solar Cells with High Efficiency and Photovoltage. *Nat. Photonics* **2015**, *9* (3), 174–179.
(73) He, Z.; Zhong, C.; Su, S.; Xu, M.; Wu, H.; Cao, Y. Enhanced Power-Conversion Efficiency in Polymer Solar Cells Using an Inverted Device Structure. *Nat. Photonics* **2012**, *6* (9), 591–595.
(74) Liu, Y.; Zhao, J.; Li, Z.; Mu, C.; Ma, W.; Hu, H.; Jiang, K.; Lin, H.; Ade, H.; Yan, H. Aggregation and Morphology Control Enables Multiple Cases of High-Efficiency Polymer

Solar Cells. *Nat. Commun.* **2014**, *5* (1), 5293.
(75) Cheng, P.; Li, G.; Zhan, X.; Yang, Y. Next-Generation Organic Photovoltaics Based on Non-Fullerene Acceptors. *Nat. Photonics* **2018**, *12* (3), 131–142.
(76) McAfee, S. M.; Topple, J. M.; Hill, I. G.; Welch, G. C. Key Components to the Recent Performance Increases of Solution Processed Non-Fullerene Small Molecule Acceptors. *J. Mater. Chem. A* **2015**, *3* (32), 16393–16408.
(77) Zhan, X.; Tan, Z.; Domercq, B.; An, Z.; Zhang, X.; Barlow, S.; Li, Y.; Zhu, D.; Kippelen, B.; Marder, S. R. A High-Mobility Electron-Transport Polymer with Broad Absorption and Its Use in Field-Effect Transistors and All-Polymer Solar Cells. *J. Am. Chem. Soc.* **2007**, *129* (23), 7246–7247.
(78) Zhong, Y.; Trinh, M. T.; Chen, R.; Wang, W.; Khlyabich, P. P.; Kumar, B.; Xu, Q.; Nam, C.-Y.; Sfeir, M. Y.; Black, C.; Steigerwald, M. L.; Loo, Y.-L.; Xiao, S.; Ng, F.; Zhu, X.-Y.; Nuckolls, C. Efficient Organic Solar Cells with Helical Perylene Diimide Electron Acceptors. *J. Am. Chem. Soc.* **2014**, *136* (43), 15215–15221.
(79) Jung, J. W.; Jo, J. W.; Chueh, C.-C.; Liu, F.; Jo, W. H.; Russell, T. P.; Jen, A. K.-Y. Fluoro-Substituted n-Type Conjugated Polymers for Additive-Free All-Polymer Bulk Heterojunction Solar Cells with High Power Conversion Efficiency of 6.71\%. *Adv. Mater.* **2015**, *27* (21), 3310–3317.
(80) Earmme, T.; Hwang, Y.-J.; Murari, N. M.; Subramaniyan, S.; Jenekhe, S. A. All-Polymer Solar Cells with 3.3% Efficiency Based on Naphthalene Diimide-Selenophene Copolymer Acceptor. *J. Am. Chem. Soc.* **2013**, *135* (40), 14960–14963.
(81) Bloking, J. T.; Han, X.; Higgs, A. T.; Kastrop, J. P.; Pandey, L.; Norton, J. E.; Risko, C.; Chen, C. E.; Brédas, J.-L.; McGehee, M. D.; Sellinger, A. Solution-Processed Organic Solar Cells with Power Conversion Efficiencies of 2.5% Using Benzothiadiazole/Imide-Based Acceptors. *Chem. Mater.* **2011**, *23* (24), 5484–5490.
(82) Mori, D.; Benten, H.; Ohkita, H.; Ito, S.; Miyake, K. Polymer/Polymer Blend Solar Cells Improved by Using High-Molecular-Weight Fluorene-Based Copolymer as Electron Acceptor. *ACS Appl. Mater. Interfaces* **2012**, *4* (7), 3325–3329.
(83) Wang, Y.; Lee, J.; Hou, X.; Labanti, C.; Yan, J.; Mazzolini, E.; Parhar, A.; Nelson, J.; Kim, J.-S.; Li, Z. Recent Progress and Challenges toward Highly Stable Nonfullerene Acceptor-Based Organic Solar Cells. *Adv. Energy Mater.* **2021**, *11* (5), 2003002.
(84) Suman; Singh, S. P. Impact of End Groups on the Performance of Non-Fullerene Acceptors for Organic Solar Cell Applications. *J. Mater. Chem. A* **2019**, *7* (40), 22701–22729.
(85) Feng, H.; Yi, Y.-Q.-Q.; Ke, X.; Zhang, Y.; Wan, X.; Li, C.; Chen, Y. Synergistic Modifications of Side-chains and End Groups in Small Molecular Acceptors for High Efficient Non-Fullerene Organic Solar Cells. *Sol. RRL* **2018**, *2* (8), 1800053.
(86) Han, G.; Guo, Y.; Song, X.; Wang, Y.; Yi, Y. Terminal π–π Stacking Determines Three-Dimensional Molecular Packing and Isotropic Charge Transport in an A–π–A Electron Acceptor for Non-Fullerene Organic Solar Cells. *J. Mater. Chem. C* **2017**, *5* (20), 4852–4857.
(87) Suman; Bagui, A.; Garg, A.; Tyagi, B.; Gupta, V.; Singh, S. P. A Fluorene-Core-Based Electron Acceptor for Fullerene-Free BHJ Organic Solar Cells—towards Power Conversion Efficiencies over 10%. *Chem. Commun.* **2018**, *54* (32), 4001–4004.
(88) Armin, A.; Li, W.; Sandberg, O. J.; Xiao, Z.; Ding, L.; Nelson, J.; Neher, D.; Vandewal, K.; Shoaee, S.; Wang, T.; Ade, H.; Heumüller, T.; Brabec, C.; Meredith, P. A History and Perspective of Non-Fullerene Electron Acceptors for Organic Solar Cells. *Adv. Energy Mater.* **2021**, *n/a* (n/a), 2003570.
(89) Yang, F.; Li, C.; Lai, W.; Zhang, A.; Huang, H.; Li, W. Halogenated Conjugated Molecules for Ambipolar Field-Effect Transistors and Non-Fullerene Organic Solar Cells. *Mater. Chem. Front.* **2017**, *1* (7), 1389–1395.
(90) Feng, H.; Qiu, N.; Wang, X.; Wang, Y.; Kan, B.; Wan, X.; Zhang, M.; Xia, A.; Li, C.; Liu, F.; Zhang, H.; Chen, Y. An A-D-A Type Small-Molecule Electron Acceptor with End-Extended Conjugation for High Performance Organic Solar Cells. *Chem. Mater.* **2017**, *29* (18), 7908–7917.
(91) Lin, Y.; Wang, J.; Zhang, Z.-G.; Bai, H.; Li, Y.; Zhu, D.; Zhan, X. An Electron Acceptor Challenging Fullerenes for Efficient Polymer Solar Cells. *Adv. Mater.* **2015**, *27* (7), 1170–

1174.
(92) Zhao, W.; Li, S.; Yao, H.; Zhang, S.; Zhang, Y.; Yang, B.; Hou, J. Molecular Optimization Enables over 13% Efficiency in Organic Solar Cells. *J. Am. Chem. Soc.* **2017**, *139* (21), 7148–7151.
(93) Yuan, J.; Zhang, Y.; Zhou, L.; Zhang, G.; Yip, H.-L.; Lau, T.-K.; Lu, X.; Zhu, C.; Peng, H.; Johnson, P. A.; Leclerc, M.; Cao, Y.; Ulanski, J.; Li, Y.; Zou, Y. Single-Junction Organic Solar Cell with over 15% Efficiency Using Fused-Ring Acceptor with Electron-Deficient Core. *Joule* **2019**, *3* (4), 1140–1151.
(94) Liu, Q.; Jiang, Y.; Jin, K.; Qin, J.; Xu, J.; Li, W.; Xiong, J.; Liu, J.; Xiao, Z.; Sun, K.; Yang, S.; Zhang, X.; Ding, L. 18% Efficiency Organic Solar Cells. *Sci. Bull.* **2020**, *65* (4), 272–275.
(95) Li, S.; Zhan, L.; Liu, F.; Ren, J.; Shi, M.; Li, C.-Z.; Russell, T. P.; Chen, H. An Unfused-Core-Based Nonfullerene Acceptor Enables High-Efficiency Organic Solar Cells with Excellent Morphological Stability at High Temperatures. *Adv. Mater.* **2018**, *30* (6), 1705208.
(96) Li, Y.; Xu, Y.; Yang, F.; Jiang, X.; Li, C.; You, S.; Li, W. Simple Non-Fullerene Electron Acceptors with Unfused Core for Organic Solar Cells. *Chinese Chem. Lett.* **2019**, *30* (1), 222–224.
(97) Lee, T.; Eom, Y.; Song, C. E.; Jung, I. H.; Kim, D.; Lee, S. K.; Shin, W. S.; Lim, E. Simple Bithiophene–Rhodanine-Based Small Molecule Acceptor for Use in Additive-Free Nonfullerene OPVs with Low Energy Loss of 0.51 EV. *Adv. Energy Mater.* **2019**, *9* (16), 1804021.
(98) Li, Z.; Jiang, K.; Yang, G.; Lai, J. Y. L.; Ma, T.; Zhao, J.; Ma, W.; Yan, H. Donor Polymer Design Enables Efficient Non-Fullerene Organic Solar Cells. *Nat. Commun.* **2016**, *7* (1), 13094.
(99) Pelse, I.; Jones, A. L.; Richter, L. J.; Reynolds, J. R. Probing Crystallization Effects When Processing Bulk-Heterojunction Active Layers: Comparing Fullerene and Nonfullerene Acceptors. *Chem. Mater.* **2021**, *33* (2), 657–667.
(100) Yang, C.; Zhang, J.; Liang, N.; Yao, H.; Wei, Z.; He, C.; Yuan, X.; Hou, J. Effects of Energy-Level Offset between a Donor and Acceptor on the Photovoltaic Performance of Non-Fullerene Organic Solar Cells. *J. Mater. Chem. A* **2019**, *7* (32), 18889–18897.
(101) Tu, Z.; Han, G.; Yi, Y. Barrier-Free Charge Separation Enabled by Electronic Polarization in High-Efficiency Non-Fullerene Organic Solar Cells. *J. Phys. Chem. Lett.* **2020**, *11* (7), 2585–2591.
(102) Classen, A.; Chochos, C. L.; Lüer, L.; Gregoriou, V. G.; Wortmann, J.; Osvet, A.; Forberich, K.; McCulloch, I.; Heumüller, T.; Brabec, C. J. The Role of Exciton Lifetime for Charge Generation in Organic Solar Cells at Negligible Energy-Level Offsets. *Nat. Energy* **2020**, *5* (9), 711–719.
(103) Perdigón-Toro, L.; Zhang, H.; Markina, A.; Yuan, J.; Hosseini, S. M.; Wolff, C. M.; Zuo, G.; Stolterfoht, M.; Zou, Y.; Gao, F.; Andrienko, D.; Shoaee, S.; Neher, D. Barrierless Free Charge Generation in the High-Performance PM6:Y6 Bulk Heterojunction Non-Fullerene Solar Cell. *Adv. Mater.* **2020**, *32* (9), 1906763.
(104) Gurney, R. S.; Lidzey, D. G.; Wang, T. A Review of Non-Fullerene Polymer Solar Cells: From Device Physics to Morphology Control. *Rep. Prog. Phys.* **2019**, *82* (3), 36601.
(105) Hestand, N. J.; Spano, F. C. Expanded Theory of H- and J-Molecular Aggregates: The Effects of Vibronic Coupling and Intermolecular Charge Transfer. *Chem. Rev.* **2018**, *118* (15), 7069–7163.
(106) Li, D.; Zhang, X.; Liu, D.; Wang, T. Aggregation of Non-Fullerene Acceptors in Organic Solar Cells. *J. Mater. Chem. A* **2020**, *8* (31), 15607–15619.
(107) Li, W.; Chen, M.; Cai, J.; Spooner, E. L. K.; Zhang, H.; Gurney, R. S.; Liu, D.; Xiao, Z.; Lidzey, D. G.; Ding, L.; Wang, T. Molecular Order Control of Non-Fullerene Acceptors for High-Efficiency Polymer Solar Cells. *Joule* **2019**, *3* (3), 819–833.
(108) Lai, H.; Zhao, Q.; Chen, Z.; Chen, H.; Chao, P.; Zhu, Y.; Lang, Y.; Zhen, N.; Mo, D.; Zhang, Y.; He, F. Trifluoromethylation Enables a 3D Interpenetrated Low-Band-Gap Acceptor for Efficient Organic Solar Cells. *Joule* **2020**, *4* (3), 688–700.

Chapter 2: Side-chain engineering on bithiophene-rhodanine based non-fullerene acceptors

Abstract

Two simple bithiophene-rhodanine-based non-fullerene acceptors, carrying either a linear *n*-octyl (**2T-ORh**) or a branched 2'-ethylhexyl (**2T-EHRh**) alkyl chain on the rhodanine, were synthesized and compared in terms of optoelectronic properties and photovoltaic performance. While the absorption spectra of both molecules were virtually identical in solution, remarkable differences were observed in thin film. In pristine film, **2T-ORh** shows predominantly H-type aggregation, which changes to a more J-type aggregation after solvent vapor annealing. For **2T-EHRh**, more J-type aggregation was observed in pristine film and the aggregation behavior did not change after SVA. As expected both molecules have equal energetics, ruling out any potential electronic effect on the device performance. For each NFA different processing conditions were required to obtain the best performance. For **2T-ORh** devices the highest efficiency was obtained via optimized solvent vapor annealing and was 4.74%. The performance of **2T-EHRh** devices was less influenced by solvent vapor annealing, but showed an efficiency of 5.19% when DPE was added as a co-solvent.

1. Introduction

In A-D-A type non-fullerene acceptors the interplay between the electron donating core (D) and electron accepting (A) units play a major role in determining the optoelectronic properties of the molecule.[1] Besides the influence of optoelectronic properties, the structural organization within the active layer is also important for device performance. Changing the type or length of alkyl side-chain on the acceptor units is an intuitive way of altering the structural organization.

Before non-fullerene acceptors had gained much attention, small molecule donors were a means to reduce synthetic costs. A way to enhance the photovoltaic efficiency of devices with these small molecule donors was through changing the structural orientation. In 2014 Jung *et al.* reported the side-chain engineering of an A-D-A type small donor, consisting of a dithienosilole core flanked by two dietopyrrolopyrrole (DPP) units. Changing the side-chains on the DPP units from *n*-octyl to a 2'-ethylhexyl did not result in any significant differences in optical or electrochemical properties. However, they did find high hole mobilities for the molecules bearing linear side-chains. This was attributed to a more favored molecular packing through octyl-octyl interdigitation.[2] A few years later A-D-A type small molecule acceptors made a breakthrough and research on these type of NFAs was thriving. In 2018, Qu and co-workers found PCEs between 6.96 and 8.18% only by varying the length of alkyl side-chain on ITBTR type NFAs.[3] In 2020, Lim found that changing the length of alkyl side-chain from an ethyl to an octyl causes a three-fold increase in performance from 0.47 to 1.81%, for simple rhodanine flanked bithiophene NFAs. This was attributed to the poor solubility and strong aggregation of the ethyl-rhodanine NFA.[4] Besides changing the length of side-chain, changing the type of side-chain, *i.e.* linear or branched¸ has also been investigated. In their recent work, Lee and co-workers showed that changing an octyl side-chain to a butyloctyl strongly influences the intermolecular aggregation of a rhodanine flanked thiophene-benzothiadizaone-thiophene NFA.[5] It is likely that the performance, attributed to a change in morphology, of these simple unfused NFAs is more susceptible to relatively small structural changes relative to the fused-ring NFAs.

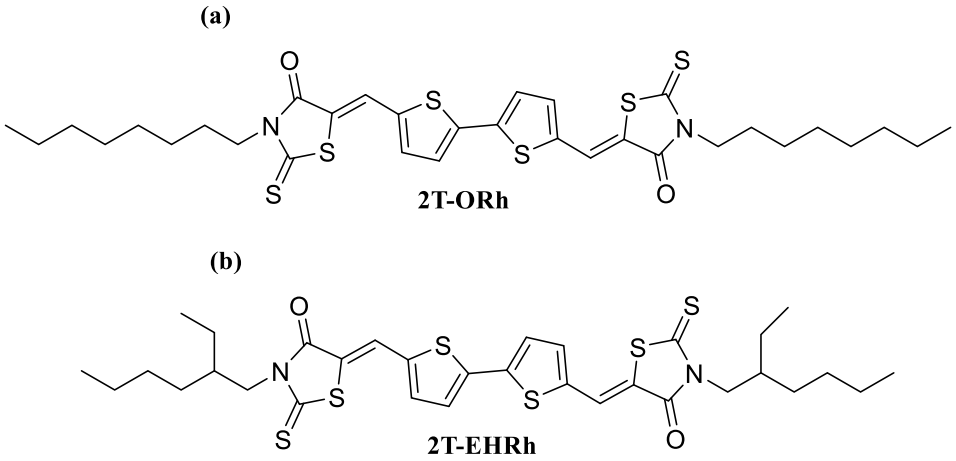

Figure 2.1: Molecular structures of the two non-fullerene acceptors (a) **2T-ORh** and (b) **2T-EHRh**.

In this chapter, the reference material **2T-ORh** (**Figure 2.1a**) and a new side-chain engineered A-D-A type non-fullerene acceptor will be synthesized. This new NFA carries 2'-ethylhexyl side-chains on both rhodanine groups (**Figure 2.1b**). The effect of this change in the acceptor units on the optoelectronic properties and photovoltaic performance will be investigated.

2. Results and Discussion

2.1 Synthesis

The work by Lee *et al.* shows the two-step synthesis of **2T-ORh**.[6] This protocol has been followed and adapted to synthesize the two targeted NFAs, **2T-ORh** and **2T-EHRh** (**Scheme 2.1**). In the first step, the *N*-functionalized rhodanines (**3a** and **3b**) were synthesized by following the Holmberg method,[7,8] in which bis(carboxymethyl)trithiocarbonate is reacted with the corresponding primary-amine (**2a** or **2b**). In the second step, the rhodanine groups were attached to the bithiophene core via a Knoevenagel condensation, using piperidine as the catalyst. While the synthesis of the rhodanine groups was performed in a good yield (≈ 80%), the Knoevenagel condensations resulted in lower yields (≈ 40%) than reported by Lee *et al*.[6] This low yield might be related to the use of non-anhydrous chloroform as solvent. A more detailed description of the performed synthesis and structural characterization is described in the Experimental section.

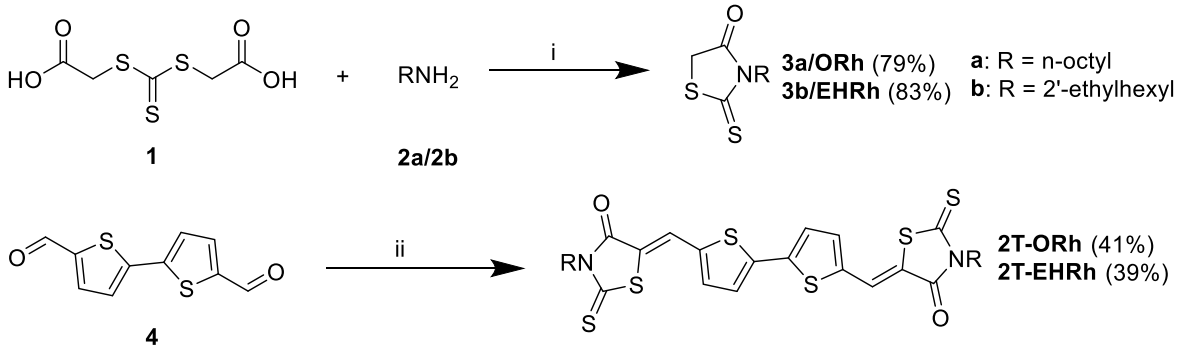

Scheme 2.1: Synthesis of the **2T-ORh** and **2T-EHRh** NFAs. (i) TEA, DME, 90 °C; (ii) 3 eq. **3a**/**3b**, piperidine, CF, 80 °C. Reaction yields are given between parentheses.

2.2 Optical and electrochemical properties

The optical properties of the two bithiophene based NFAs, **2T-ORh** and **2T-EHRh**, were investigated by UV-vis-NIR absorption spectroscopy in chloroform solution and in thin film (**Figure 2.2a**).

Table 2.1: Optical and electrochemical properties of the two NFAs.

	2T-ORh	**2T-EHRh**
[a] $E_{g,opt}^{sol}$ [eV]	2.16	2.16
[a] $E_{g,opt}^{film,\ pristine}$ [eV]	1.97	2.00
[a] $E_{g,opt}^{film,\ SVA}$ [eV]	2.00	1.99
λ_{max}^{sol} [nm]	502	502
$\lambda_{max}^{film,\ pristine}$ [nm]	457	523
$\lambda_{max}^{film,\ SVA}$ [nm]	527	496
[b] E_{ox} [V]	0.88	0.88
[b] E_{red} [V]	-1.25	-1.24
[c] E_{HOMO} [eV]	-5.68	-5.68
[c] E_{LUMO} [eV]	-3.55	-3.56
$E_{g,SWV}$ [eV]	2.13	2.12

[a] $E_{g,opt} = 1240/\lambda_{onset}$ (eV). [b] *vs.* Fc/Fc^+. [c] Determined using a work-function of −4.8 eV for Fc/Fc^+ versus vacuum.

In solution, both molecules show a virtually identical absorption profile, with an absorption maximum (λ_{max}) at 502 nm and shoulder at 535 nm. The relatively weak absorption around 400 nm can be attributed to localized π-π* transitions, while the longer wavelength absorption at 420-600 nm can be attributed to intramolecular charge transfer (ICT) between the bithiophene donor and the rhodanine acceptor units.[1,5,9] In film, both acceptors show a broader absorption related to intermolecular aggregation. Similar to the results in the work of Lee et al.[1], the **2T-ORh** NFA shows a clear blue-shifted absorption maximum at

457 nm and a weak red-shifted absorption around 570 nm in pristine film. This suggests that for the as-cast film the molecule is predominantly in an H-type aggregation.[10,11] The large blue-shifted absorption maximum causes a decreased absorption in the 500-600 nm range, limiting the amount of overlap with the AM1.5G spectrum, which could impede the attainable J_{sc}. In contrast to **2T-ORh**, the absorption spectrum of **2T-EHRh** in pristine thin film does not show a blue-shifted absorption maximum. Instead, the absorption maximum red-shifts and shows a much more pronounced red-shifted absorption around 570 nm, indicating that the molecule is predominantly in a J-type aggregation in the as-cast film. Interestingly, after solvent vapor annealing (SVA) a change in aggregation behavior of **2T-ORh** can be observed. After SVA there is more contribution of J-type aggregates, producing a red-shifted absorption maximum at 527 nm. This effect can also be seen by the color change in the film, as depicted in **Figure 2.2b**. The optical bandgap, estimated from the onset of absorption, does not change significantly with SVA as they are 1.97 and 2.00 eV before and after SVA respectively. For the **2T-EHRh** film, the absorption profile after SVA did not show any significant change in aggregation behavior and is nearly identical to that of the pristine film. The larger blue-shifted absorption in pristine film and the larger red-shifted absorption after SVA of the **2T-ORh** NFA can probably be explained by the better molecular packing of **2T-ORh** compared to **2T-EHRh**. This finding is consistent with previously reported absorption profiles of molecules where branched side-chains are introduced on the rhodanine.[5,12] The **2T-EHRh** NFA shows an optical bandgap of 2.00 eV, which is virtually identical to that of **2T-ORh**. From the absorption spectra in **Figure 2.2a**, it can be seen that after solvent vapor annealing both NFAs show a complementary absorption relative to PTB7-Th. All optical characteristics are summarized in **Table 2.1**.

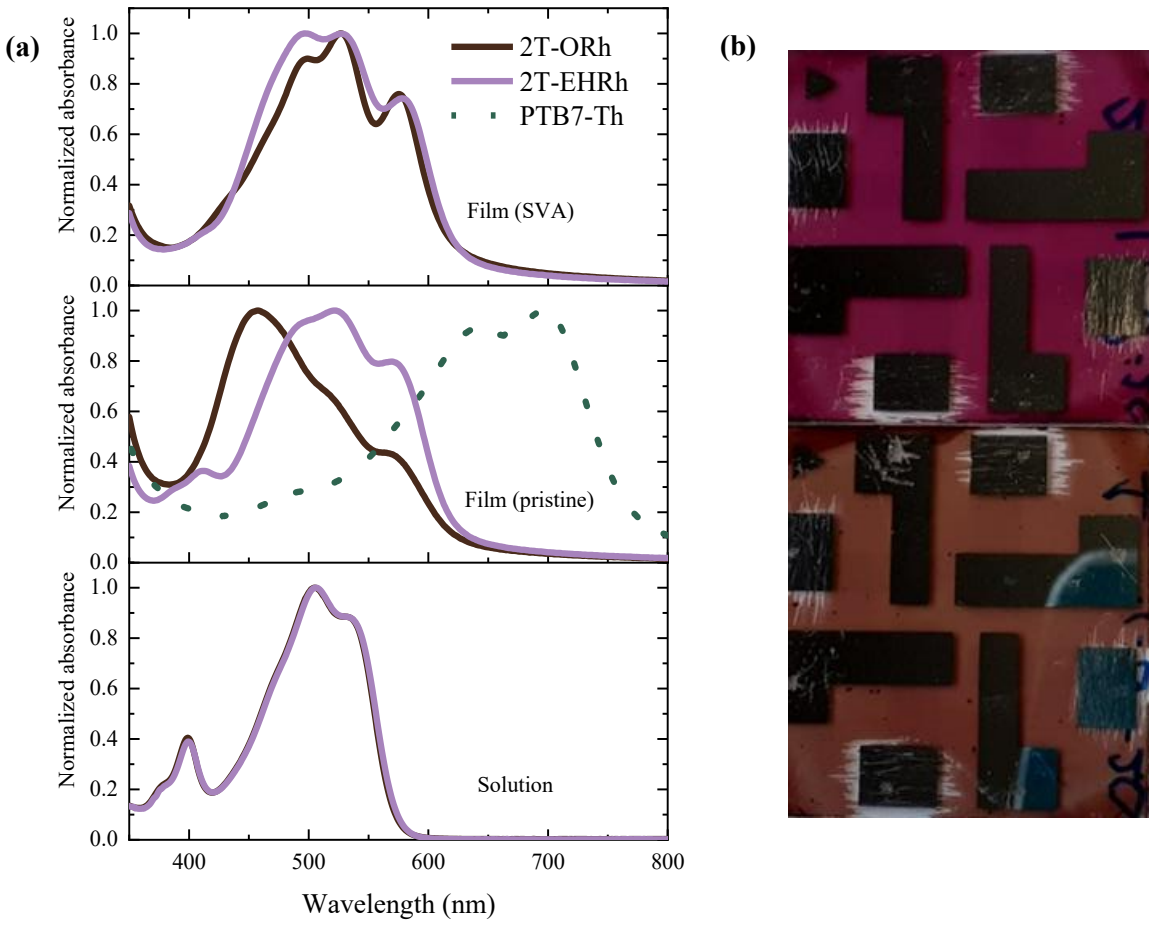

Figure 2.2: (a) Normalized UV-vis-NIR absorption spectra of **2T-ORh** and **2T-EHRh** in chloroform solution, as pristine thin film and as solvent vapor annealed film. The absorption spectrum of PTB7-Th in thin film is also included. (b) The color change caused by the solvent vapor annealing of a PTB7-Th:**2T-ORh** blend film. Bottom: pristine film, top: solvent vapor annealed film.

The frontier molecular orbital energy levels (HOMO and LUMO) of the two rhodanine-based NFAs were determined using square-wave voltammetry (SWV) in thin film. The recorded voltammograms are depicted in **Figure 2.3a** and the determined energy levels and the corresponding bandgaps are listed in **Table 2.1**. It should be noted that the thin-film measurements of the NFAs are not reversible, likely because the small molecules start to dissolve in acetonitrile upon charging. The reversibility was verified by measuring SWV in solution. It can be seen that both the HOMO and the LUMO are essentially the same for both molecules, ruling out any potential electronic effect on the device performance. This similarity in energy levels is expected, because changing the type of the alkyl side-chain does not contribute to a change in electron-accepting strength of the rhodanine and is consistent with previously reported energy levels where only the alkyl side-chain on the rhodanine is varied.[5,12] In **Figure 2.3b**, the energy levels of both NFAs are compared with the energy levels of the PTB7-Th polymer, which were also determined in thin film. The molecules show approximately a 0.25 eV and 0.3 eV LUMO-LUMO and HOMO-HOMO offset with PTB7-Th respectively. As can be seen in **Table 2.1**, the electrochemical bandgaps as determined with SWV are higher than the determined optical bandgaps. This discrepancy is due to different fundamentals of the measurements themselves.

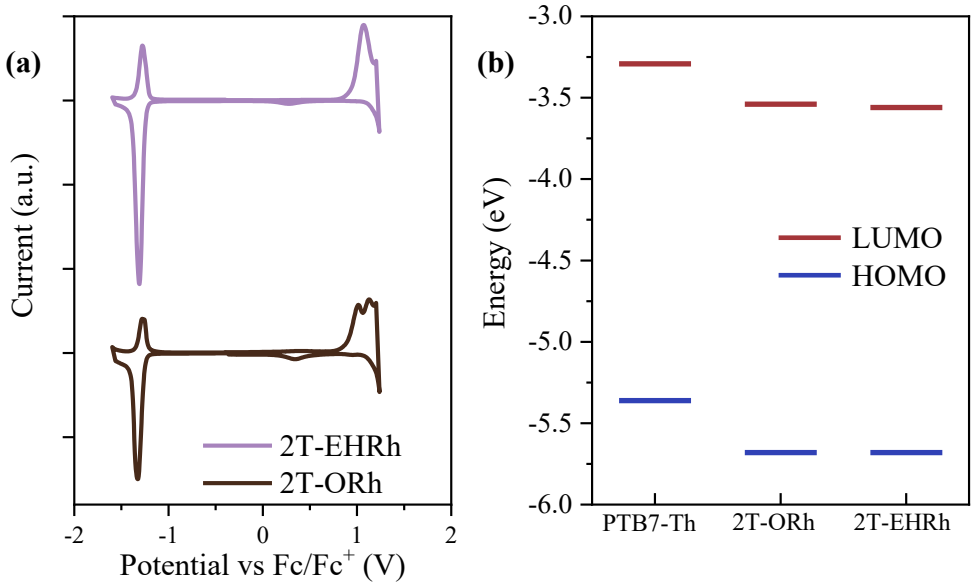

Figure 2.3: (a) Square-wave voltammograms of **2T-ORh** and **2T-EHRh** in thin film. (b) Frontier orbital energy levels of the two NFAs and PTB7-Th, calculated from the oxidation and reduction onsets relative to the vacuum level.

2.3 Photovoltaic devices

The photovoltaic performance of the two rhodanine-based NFAs was characterized in a bulk-heterojunction photovoltaic device, using PTB7-Th as the electron donor. All devices were fabricated in an inverted structure (ITO/ZnO/PEIE/PTB7-Th:NFA (1:2)/MoO_3/Ag). The active layer was spin coated at 1500 rpm, yielding uniform layers of approximately 100 nm thick. Herefore, solutions in chloroform with a total solid concentration of 15 mg mL^{-1}, *i.e.* 5 mg mL^{-1} PTB7-Th and 10 mg mL^{-1} acceptor, were prepared. The influence of two morphology control strategies on the device performance was investigated. The first strategy was subjecting the devices to solvent vapor annealing (SVA) using various solvents and annealing times. As a second method, addition of a co-solvent, diphenyl ether (DPE), in different volume percentages was employed.

2.3.1 Optimization by solvent vapor annealing

Film morphology is a key parameter to OPV device performance and solvent vapor annealing (SVA) has proven to be effective in enhancing the performance of an OPV device by changing the film morphology to a more thermodynamically stable state. In this study the effect on the device performance

of three different solvents, chloroform (CF), chlorobenzene (CB) and *ortho*-dichlorobenzene (*o*-DCB), and the respective annealing times has been investigated.

Table 2.2: Photovoltaic characteristics of **2T-ORh** and **2T-EHRh** based devices under different solvent vapor annealing conditions.

Acceptor	SVA	[a] J_{sc} [mA cm^{-2}]	V_{oc} [V]	FF	[a] PCE [%]
2T-ORh	No	9.21 (7.46)	0.84	0.31	2.37 (1.92)
	5s, CF	8.53	0.82	0.30	2.08
	15s, CF	8.41	0.73	0.29	1.77
	30s, CF	9.57 (8.63)	1.05	0.45	4.46 (4.03)
	45s, CF	9.29	1.05	0.44	4.25
	5s, *o*-DCB	8.11	0.75	0.29	1.77
	15s, *o*-DCB	7.95	0.74	0.29	1.68
	30s, *o*-DCB	8.18	0.84	0.29	2.01
	45s, *o*-DCB	10.50 (9.92)	1.04	0.46	5.04 (4.74)
	60s, *o*-DCB	9.92	1.04	0.47	4.80
	80s, *o*-DCB	10.20	1.06	0.47	4.94
	30s, CB	9.86	1.02	0.41	4.13
	45s, CB	6.14	0.98	0.43	2.62
2T-EHRh	No	9.69 (8.42)	0.83	0.33	2.65 (2.30)
	15s, CF	9.73	0.73	0.31	2.16
	30s, CF	5.91	0.47	0.29	0.80
	30s, *o*-DCB	10.10	0.77	0.32	2.46
	45s, *o*-DCB	10.70 (7.44)	0.87	0.36	3.37 (2.34)
	60s, *o*-DCB	9.75	0.80	0.31	2.46
	90s, *o*-DCB	7.85	0.26	0.26	0.54

[a] Value obtained by integrating the EQE with the AM1.5G spectrum is given between parentheses.

In **Figure 2.4a**, an S-shape in the *J-V* curve is observed for the pristine **2T-ORh** blend, which causes a lowered J_{sc}, V_{oc} and FF. There are multiple reasons for this S-shape to occur, such as unbalanced charge mobilities, energy barriers, defects and dipoles at the interface or non-ideal contact at the cathode, all of which cause charge accumulation in the active layer.[13-15] In **Table 2.2**, it can be seen that the devices show a slight decrease in performance with short SVA times, due to a lowered short-circuit current density (J_{sc}) and open-circuit voltage (V_{oc}). Upon increasing the SVA time, the PCE increases due to an increase of all three characterization parameters (J_{sc}, V_{oc} and FF). For CF and *o*-DCB annealed devices, the efficiency seems to plateau after reaching a maximum efficiency. Whereas for CB annealed devices the PCE decreases from 4.13% to 2.62% when going from 30 to 45 seconds SVA. For devices based on **2T-ORh**, the highest PCE is achieved for films subjected to 45s of solvent vapor annealing with *o*-DCB. After SVA, it can be seen that the S-shape in the *J-V* curve has disappeared which explains the increased characterization parameters. The increased J_{sc} after SVA is also visible in the EQE spectrum as depicted in **Figure 2.4b**, which shows an increased EQE over the entire range. This suggests better charge separation or – transport properties, probably due to increased phase separation and crystallinity. The better overlap with the AM1.5G spectrum after SVA, as indicated in the UV-vis-NIR results, might also contribute to the higher J_{sc}. A more increased contribution from the acceptor in the 400-600 nm range can also be seen in the EQE spectrum, indicating that the channel II photocurrent has become more dominant.[16] Interestingly, upon visual inspection of the films after seven months it was observed that the color of the pristine film changed from brown to purple. This purple color is also observed for the SVA treated film immediately after annealing, as shown in **Figure 2.2b**. The fact that the color of the pristine film changes to the color of the annealed film suggests that the morphology of the annealed film is likely more stable.

The *J-V* curve of the pristine **2T-EHRh** device (**Figure 2.4c**) also shows an S-shape, but it is less pronounced than in the pristine **2T-ORh** device. In **Table 2.2** it can be seen that the performance of the **2T-EHRh** does not increase as drastically with SVA as it does for **2T-ORh**, consistent with the lack of aggregation change found in UV-vis-NIR. It can also be seen that there is a clear maximum in device performance over the SVA time range, whereas for the **2T-ORh** devices there seemed to be a plateau. The optimal SVA conditions were also found to be 45s of solvent vapor annealing with *o*-DCB. As opposed to the solvent vapor annealed **2T-ORh** device, the S-shape in the *J-V* curve of the **2T-EHRh** device has not completely disappeared after SVA. It did however decrease, resulting in the slightly increased device performance, yet there is still a relatively high series resistance and high bias-dependency. The largest difference between the annealed **2T-ORh** and **2T-EHRh** devices is in the V_{oc} which are 1.04 and 0.87 V respectively. As this difference cannot be due to different energetics it is attributed to increased charge recombination in the **2T-EHRh** device. Another interesting difference between the **2T-ORh** and **2T-EHRh** devices is the difference in channel II photocurrent contribution as determined from the EQE (**Figure 2.4d**). Where for the **2T-ORh** devices an increase of this current upon SVA was observed, for **2T-EHRh** this difference is not seen and the contributions are roughly equal to that of the pristine **2T-ORh** device.

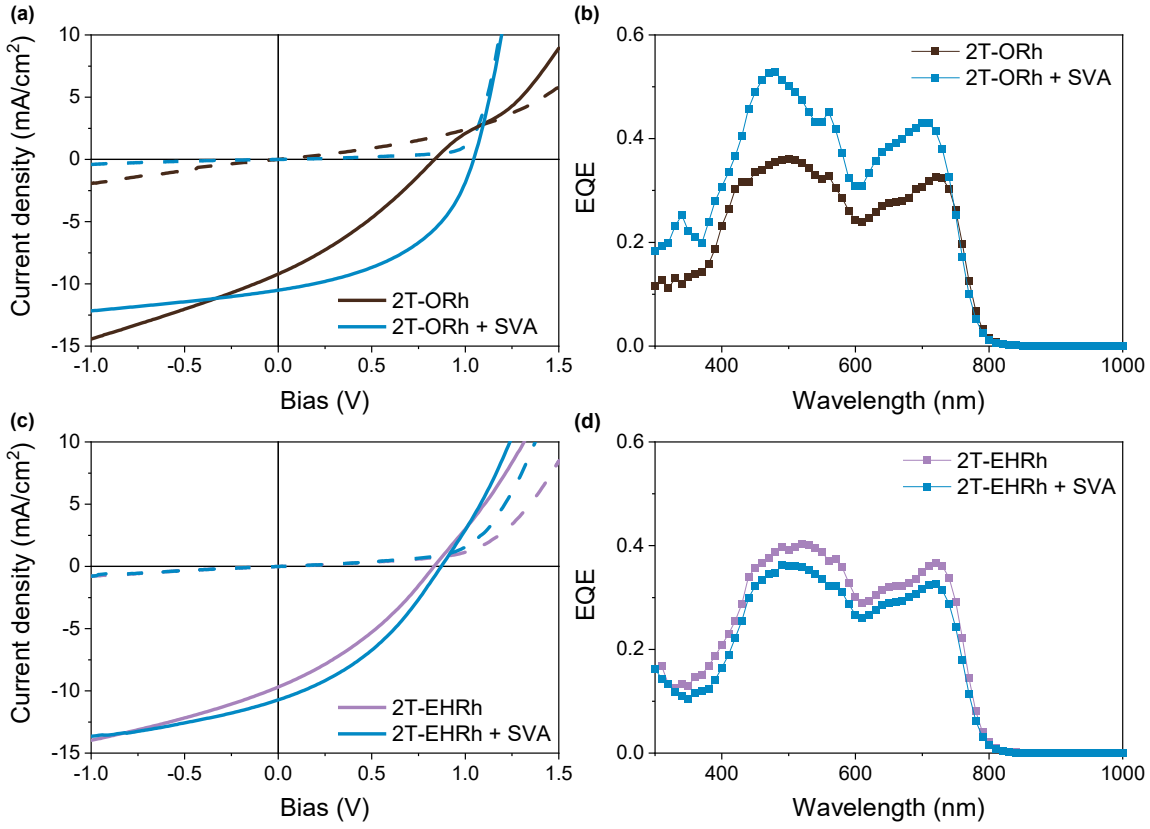

Figure 2.4: (a) *J-V* characteristics in the dark (dashed lines) and under AM1.5G illumination (solid lines) of photovoltaic devices based on **2T-ORh** in pristine film and under optimized SVA conditions. (b) Corresponding EQE spectra of (a). (c) *J-V* characteristics in the dark (dashed lines) and under AM1.5G illumination (solid lines) of photovoltaic devices based on **2T-EHRh** in pristine film and under optimized SVA conditions. (d) Corresponding EQE spectra of (c).

2.3.2 Co-solvent optimization

Another method to enhance the photovoltaic performance by changing the active layer morphology is the incorporation of co-solvents in the solvent system. Diphenyl ether (DPE) has proven to be widely beneficial, being one of the most effective co-solvents for polymer:fullerene blends.[17] More recently, enhanced PCEs by incorporation of DPE in the casting solution in NFA based devices were shown.[12,18,19] Therefore, DPE was chosen as co-solvent in this research.

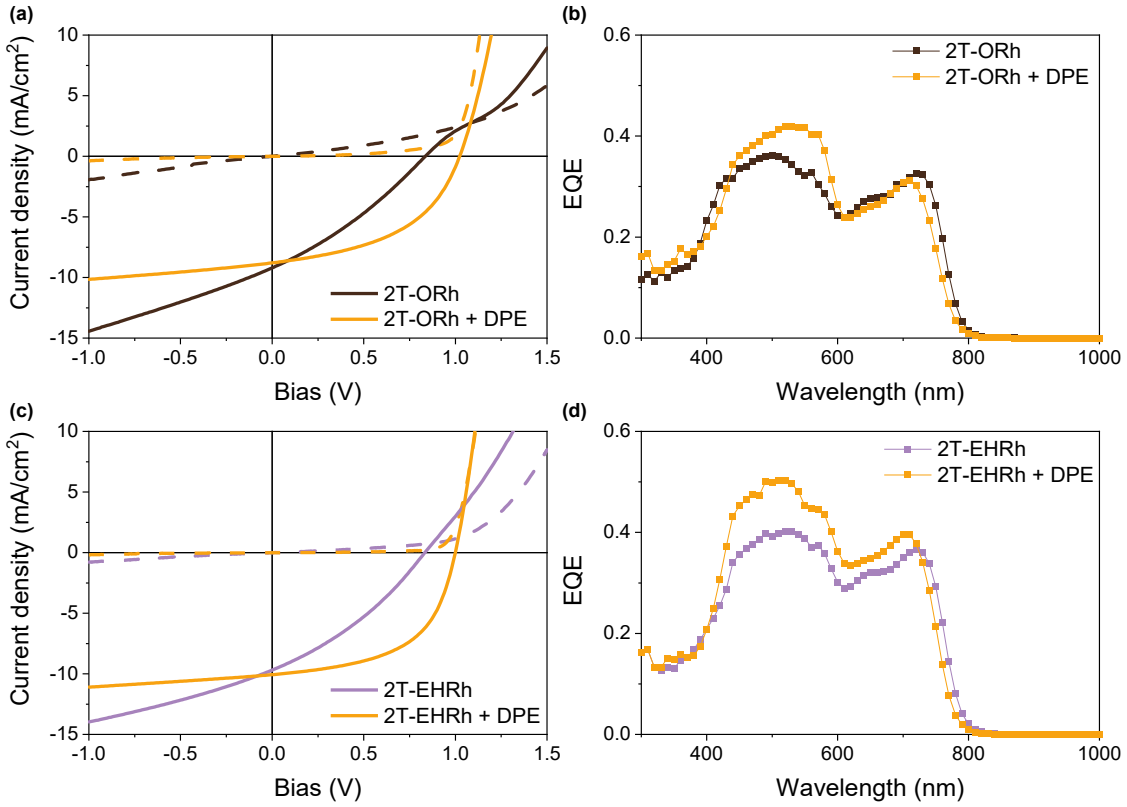

Figure 2.5: (a) *J-V* characteristics in the dark (dashed lines) and under AM1.5G illumination (solid lines) of photovoltaic devices based on **2T-ORh** in pristine film and under optimized co-solvent conditions. (b) Corresponding EQE spectra of (a). (c) *J-V* characteristics in the dark (dashed lines) and under AM1.5G illumination (solid lines) of photovoltaic devices based on **2T-EHRh** in pristine film and under optimized co-solvent conditions. (d) Corresponding EQE spectra of (c).

Table 2.3 shows the effect of the addition of 1, 2 and 3 volume percent of DPE to the solvent system on the photovoltaic characteristics of devices based on each NFA. For both molecules, incorporation of 2 vol% of DPE in the solvent system has shown to yield the most efficient devices, mainly due to an increased V_{oc} and FF. For **2T-ORh** devices, incorporation of DPE in the solvent system seems to have the same effect as SVA, increasing the V_{oc} and FF by eliminating the S-shape in the *J-V* curve (**Figure 2.5a**). As opposed to the solvent vapor annealed device there is no significant increase in J_{sc} (**Figure 2.5b**) and therefore incorporation of DPE in the solvent system does not outperform the solvent vapor annealed device. This finding is consistent with that of Lee *et al.*, where they also found that incorporation of co-solvents does not outperform the solvent vapor annealed device.[6]

Table 2.3: Photovoltaic characteristics of **2T-ORh** and **2T-EHRh** based devices cast from different solvent systems.

Acceptor	Co-solvent	[a] J_{sc} [mA cm^{-2}]	V_{oc} [V]	FF	[a] PCE [%]
2T-ORh	No	9.21 (7.46)	0.84	0.31	2.37 (1.92)
	1 vol% DPE	9.42	0.94	0.44	3.91
	2 vol% DPE	8.17 (7.69)	1.02	0.49	4.11 (3.85)
	3 vol% DPE	6.05	1.03	0.48	3.03
2T-EHRh	No	9.69 (8.42)	0.83	0.33	2.65 (2.30)
	1 vol% DPE	9.50	1.00	0.54	5.09
	2 vol% DPE	10.10 (9.48)	1.00	0.55	5.51 (5.19)
	3 vol% DPE	6.00	0.97	0.46	2.68

[a] Value obtained by integrating the EQE with the AM1.5G spectrum is given between parentheses.

For **2T-EHRh**, the device performance more than doubles (from 2.30% to 5.19%) by incorporating 2 vol% of DPE in the casting solution. From **Figure 2.5c** it can be seen that this increase can mainly be

attributed to the complete disappearance of the S-shape in the *J-V* curve, resulting in a much higher FF and V_{oc}. For the device fabricated by including DPE in the casting solvent an increased channel II photocurrent is visible (**Figure 2.5d**) as opposed to the solvent vapor annealed device.

In the EQE spectrum of **2T-ORh** (**Figure 2.5b**) it can be seen that addition of DPE in the casting solution causes a change in the EQE shape, whereas the shape of the EQE of **2T-EHRh** (**Figure 2.5d**) does not significantly change. Interestingly, incorporating DPE in the solvent system causes a 10 nm blue shift in onset for both blends (**Figure 2.5b** and **d**). This behavior has been further studied *via* UV-vis-NIR absorption spectroscopy, which is depicted in **Figure 2.6a**. From this figure, it can be seen that addition of DPE does not significantly influence the absorption behavior of a polymer only film, whereas it does for the blend film. In the blend film the shift in onset, as in the EQE, is visible as well as the changed shape in the acceptor region. This change in absorption is roughly equal to the change in absorption when the blend is subjected to solvent vapor annealing. This indicates that addition of DPE does not only influence the PTB7-Th aggregation, but also the acceptor aggregation and that the behavior is an interplay between both molecules.

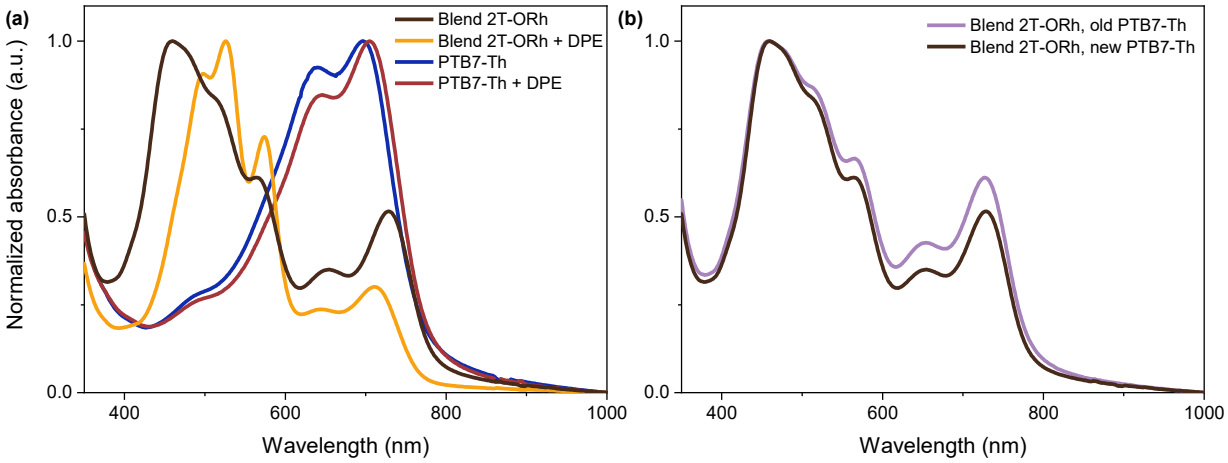

Figure 2.6: Thin film UV-vis-NIR absorption spectra: (a) showing the effect of DPE and (b) showing the difference between the new and old PTB7-Th batch.

2.3.3 New PTB7-Th batch

Near the end of the project, the PTB7-Th batch that had been used in all OPV devices started to run out and therefore all further characterization had to be done with a new batch. The performance of this batch in an OPV device has been determined and is compared to a device made with the old batch. For both these devices the active layer was subjected to 45 seconds of *o*-DCB solvent vapor. These results are depicted in **Table 2.4** and **Figure 2.7**.

Table 2.4: Photovoltaic characteristics of solvent vapor annealed blends of **2T-ORh** with the old and new PTB7-Th batch.

PTB7-Th batch	J_{sc} [mA·cm^{-2}]	V_{oc} [V]	FF	PCE [%]
Old	10.92	1.02	0.44	4.94
New	4.36	0.95	0.33	1.35

Unfortunately, it can be seen that the device performance has dropped from 4.94% to 1.35% with the new polymer batch, mainly attributed to a decreased J_{sc} and FF. From the EQE spectrum (**Figure 2.7b)** it can be seen that the polymer contribution at higher wavelengths is reduced and that the proportion of the peak around 330 nm has increased. This influence of the polymer batch on the device performance could explain the difference between the efficiencies found in literature and found in this research. In **Figure 2.6b** an overlay of a UV-vis-NIR absorption spectrum of a blend made from **2T-ORh** and the new PTB7-Th batch with the spectrum of the same blend with the old batch is made. Here it can also be

seen that in the blend made with the new PTB7-Th the absorption of the polymer at higher wavelengths has decreased, consistent with the findings in the EQE.

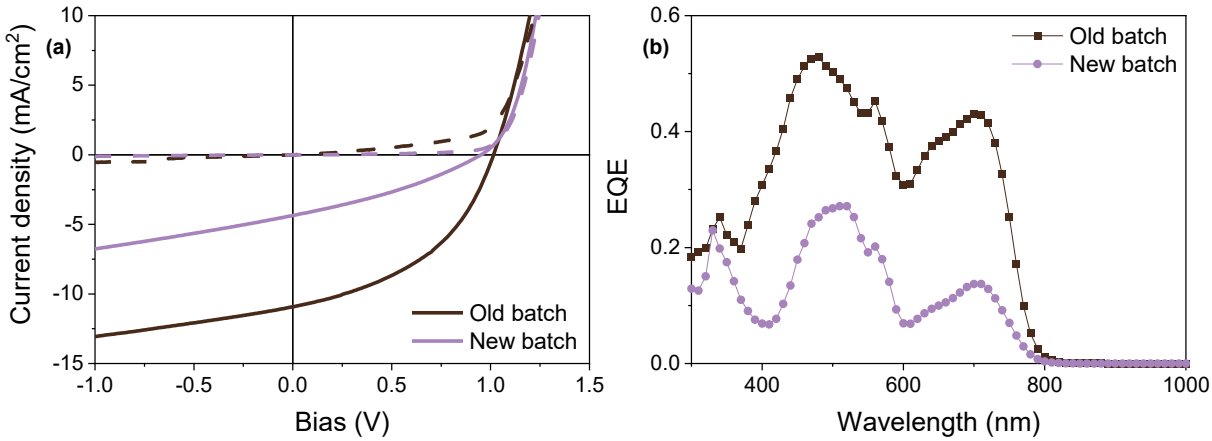

Figure 2.7: *J-V* characteristics (a) in the dark (dashed lines) and under AM1.5G illumination (solid lines) and EQE spectra (b) of solvent vapor annealed devices made with **2T-ORh** and the old or new PTB7-Th batch.

2.4 Morphology

In order to explain some of the observations in photovoltaic performance, the morphology of the pristine and optimized active layers was studied. For this atomic force microscopy (AFM) images in height and phase mode were measured, which are shown in **Figure 2.8** and **Figure 2.9**. A remark should be made that for these measurements the new PTB7-Th batch has been used.

As shown in **Figure 2.8a**, the pristine **2T-ORh** blend film is relatively flat and featureless with a root-mean-square (RMS) roughness of 1.35 nm. After solvent vapor annealing, the **2T-ORh** blend film (**Figure 2.8b**) shows more texture with an increased RMS roughness of 2.47 nm, which might be due to a higher degree of phase segregation and crystallinity. More crystalline features usually lead to higher charge carrier mobilities, which likely explains the observed increase in J_{sc} and FF. The **2T-EHRh** pristine film (**Figure 2.8c**) shows a slightly larger roughness, 2.17 nm, compared to the **2T-ORh** pristine film (**Figure 2.8a**). In contrast to the observations for the **2T-ORh** blend film, the roughness of the solvent vapor annealed **2T-EHRh** film (1.75 nm) is decreased relative to the pristine film (**Figure 2.8d**). This observation matches well with the only marginal improvement of the shape of the *J-V* curve and the lowered EQE current in the solvent vapor annealed device. A large increase in surface roughness (RMS = 4.37 nm) can be seen when 2 vol% of DPE is added to the casting solution (**Figure 2.8e**). The phase image now shows a similar structure to that of the solvent vapor annealed **2T-ORh** blend, with small features. Also in this case, the S-shape in the *J-V* curve of the pristine **2T-EHRh** film disappears, resulting in an improvement of all photovoltaic parameters.

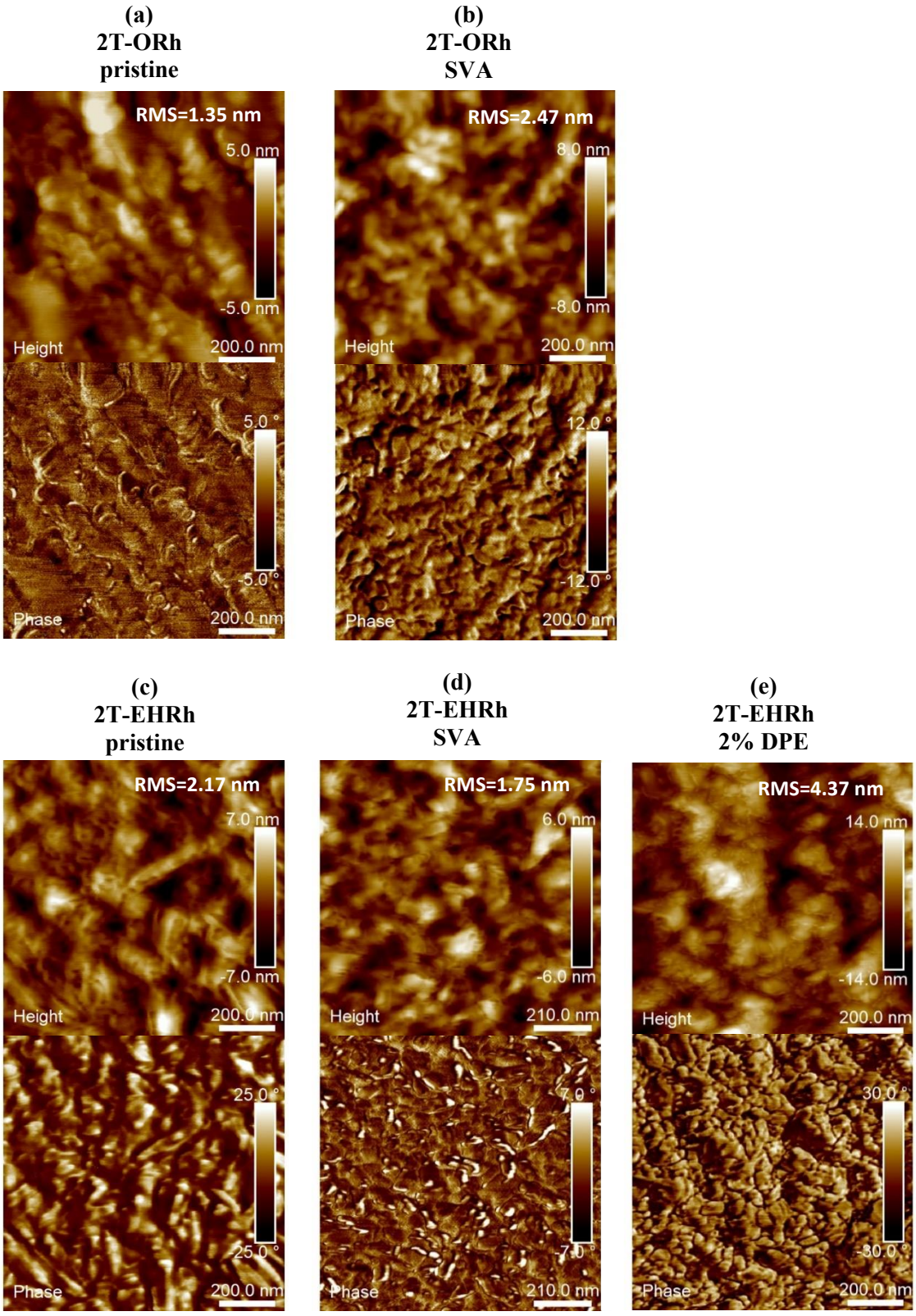

Figure 2.8: AFM height, with the roughness given in top-right corner, (top) and phase (bottom) images (1 x 1µm) of blends for: pristine **2T-ORh** (a), SVA **2T-ORh** (b), pristine **2T-EHRh** (c), SVA **2T-EHRh** (d) and co-solvent **2T-EHRh** (e).

3. Conclusion and Outlook

In this chapter, two bithiophene-rhodanine-based NFAs, one with *n*-octyl side-chains (**2T-ORh**) and one with 2'-ethylhexyl side-chains (**2T-EHRh**) were successfully synthesized. By changing the type of side-chains on the rhodanine, the thin-film aggregation behavior of the molecule is changed. This is verified by UV-vis-NIR absorption spectrometry where **2T-ORh** showed predominantly H-type aggregation in pristine film, while **2T-EHRh** shows more J-type aggregates. After solvent vapor annealing, the aggregation behavior of **2T-EHRh** showed no significant changes, whereas the aggregation of **2T-ORh** showed more J-type contribution after SVA. The optical bandgap for both molecules was determined *via* the absorption onset in the UV-vis-NIR spectra, resulting in bandgaps of ± 2 eV. Square-wave voltammetry measurements confirmed that the energy levels of the acceptors are not influenced by varying the rhodanine side-chain. These measurements also showed roughly equal HOMO-HOMO and LUMO-LUMO offsets, as they were 0.3 and 0.25 eV respectively.

Photovoltaic devices were fabricated and optimized *via* co-solvents and solvent vapor annealing. For **2T-ORh**, the best device was obtained by annealing it for 45s in *o*-DCB, leading to a 4.74% efficiency. By examining the morphology it was found that the phase segregation and domain crystallinity is increased in the annealed film relative to the pristine film, leading to better charge transport properties. The achieved efficiency is lower than efficiencies found in literature, which is probably due to the large influence of processing conditions and the polymer batch-to-batch variation. SVA did not significantly increase the performance of a **2T-EHRh** based device, consistent with the lack of aggregation change after SVA found in the UV-vis-NIR study. The best device was obtained by incorporating 2 volume percent DPE in the casting solution, yielding a 5.19% efficiency. Morphological studies showed a large increase in phase segregation, indicating better charge transport properties.

To further improve the device performance, other co-solvents could be examined. These may help to improve the crystallinity even further and thereby increase the J_{sc} and FF. Furthermore, changing the donor-acceptor ratio could help to improve the active layer morphology. Moreover, it would be interesting to study the crystallinity and aggregation behavior of the active layer in more detail, for this grazing-incidence wide-angle X-ray scattering could be performed. In order to say more about the influence of the side-chains on the device performance, the set of molecules could be expanded. These may include a more bulky side-chain or a longer side-chain.

4. Experimental

4.1 Materials and Methods

2,2'-Bithiophene-5,5'-dicarboxaldehyde (>98%) was purchased from TCI Europe N.V. and PTB7-Th came from 1-Materials. All other chemicals and solvents were purchased from Sigma-Aldrich co or VWR. All commercially available solvents and reactants were used without further purification. All synthetic procedures were performed under a nitrogen atmosphere.

^{1}H and ^{13}C NMR spectra were measured on a Bruker Avance III spectrometer at 400 and 100 MHz respectively. Chemical shifts are reported with respect to tetramethylsilane as internal standard. Molecular weights of the **2T-ORh** and **2T-EHRh** NFAs were determined using matrix assisted laser desorption ionization time-of-flight (MALDI-TOF) mass spectroscopy on a Bruker Autoflex Speed spectrometer.

Solution and film UV-vis-NIR spectra were recorded on a Perkin Elmer Lambda 1050 spectrophotometer. Dilute solutions of **2T-ORh** and **2T-EHRh** were prepared in chloroform and films were prepared by spin coating a 6 mg mL^{-1} solution on a glass substrate at 1500 rpm. Solvent vapor annealed films were prepared from the same solution after which the films were subjected to 45 seconds of *o*-DCB vapor. For the blend films the PTB7-Th donor polymer and rhodanine-based acceptor

molecule were mixed in a 1:2 (D:A) weight ratio and dissolved in chloroform at a total solids concentration of 15 mg mL^{-1}. The films were spin coated on a glass substrate at 1500 rpm in an N_2 filled glove-box.

Square-wave voltammetry (SWV) was performed in thin film under inert atmosphere using a Biologic VSP potentiostat. All films were prepared by dip coating a flame-cleaned platinum working electrode using a stock solution of 2 mg mL^{-1} PTB7-Th in chloroform or a 4 mg mL^{-1} solution of **2T-ORh** or **2T-EHRh** in dichloromethane. A silver rod was used as counter electrode and a silver chloride coated silver rod (Ag/AgCl) was used as quasi-reference electrode. A 0.1 M tetrabutylammonium hexafluorophosphate ($TBAPF_6$) solution in acetonitrile was used as electrolyte. All measurements were reported against ferrocene/ferrocenium (Fc/Fc^+) as reference, with E_{Fc/Fc^+} set at −4.8 eV *vs*. vacuum. Measurements were performed with a 20 mV pulse height, 20 ms pulse width and 5 mV step height.

Photovoltaic devices were fabricated on pre-patterned indium tin oxide (ITO) glass substrates (Naranjo Substrates). The substrates were cleaned by sonication in acetone, followed by scrubbing with a sodium dodecyl sulfate solution (99%, Acros). After sonication in the same sodium dodecyl sulfate solution the substrates were rinsed with deionized water and underwent a final sonication in 2-propanol. To finish the cleaning, the substrates underwent a 30 minute UV-ozone treatment. A ZnO electron transport layer (ETL) was deposited onto the cleaned substrates via a sol gel method by spin coating a precursor solution. The precursor solution was prepared by dissolving 109.72 mg of zinc acetate dehydrate in 1 mL 2-methoxyethanol and 30.2 µL ethanolamine. This solution was stirred for at least 1 hour at room temperature after which it was spin coated at 4000 rpm in ambient air and immediately annealed for 5 minutes at 150 °C, resulting in a 40 nm ZnO layer. A commercially available PEIE solution of 37 wt% was further diluted in ethanol until a total mass fraction of 0.1 wt% was reached. This solution was cast on the ZnO coated substrates by spin-coating at 4000 rpm in air to yield a thin layer. This layer was annealed for 10 minutes at 100 °C. For the active layer, the PTB7-Th donor polymer and rhodanine-based acceptor molecule were mixed in a 1:2 (D:A) weight ratio and dissolved in chloroform at a total solids concentration of 15 mg mL^{-1}. This solution was heated to and kept at 60 °C under continuous stirring for 1 hour and cooled down to room temperature prior to spin coating. The active layer was spin coated at 1500 rpm in a N_2 filled glove-box to obtain an optimal layer thickness of around 100 nm. The blend films were subsequently subjected to solvent vapor annealing using different solvents and annealing times as described in the results section. This was carried out by placing 200 µL of the desired solvent in a petridish and leaving this closed for 1 minute to introduce solvent vapor. The substrate was then placed on top of an elevated stage in this petridish for the desired amount of time. The back electrode layers, MoO_3 (10 nm) followed by Ag (100 nm), were deposited by thermal evaporation in a vacuum chamber at ~ 6×10^{-7} mbar. The active area of the photovoltaic devices was determined by the intersection of the ITO pattern and the back contacts. The intersecting areas resulted in two squares of 9 mm^2 and two squares of 16 mm^2.

J-V and EQE measurements were performed under N_2 atmosphere. In order to photodope the ZnO and MoO_3 layers, the devices were illuminated for 10 minutes with UV light prior to *J-V* measurements. Current density – voltage (*J-V*) characteristics were recorded with a 4 point probe Keithley 2400 source meter under illumination with a tungsten-halogen lamp. To provide a 1000 W m^{-2} AM1.5G illumination, the light was filtered through a Schott GG385 UV filter and a Hoya LB120 daylight filter. Accurate short-circuit current density (J_{sc}) values were obtained by integrating recorded external quantum efficiency (EQE) spectra with the AM1.5G solar spectrum. The EQE measurements were performed on a custom-made setup consisting of a 50W tungsten-halogen lamp (Osram 64610), a monochromator (Oriel, Cornerstone 130), a mechanical chopper (Stanford Research Systems, SR540), a pre-amplifier (SR570), a lock-in amplifier (SR830) and a Thorlabs high intensity LED operating at 530 and 730 as a bias light. Although the setup was in ambient air, the substrates were kept encapsulated in a N_2 filled box equipped with a quartz window. A calibrated silicon cell was used as a reference prior to both the

J-V and the EQE measurements. Lastly, the active layer thickness of the substrates were determined on a Veeco Dektak 150 profilometer.

The morphologies of the films were characterized using atomic force microscopy (AFM). Which was measured on a Dimension 3100 in tapping mode. For this blend films were prepared in the same way as in the UV-vis-NIR measurements.

4.2 Synthesis

3-Octyl-2-thioxothiazolidin-4-one (ORh) (3a)

Bis(carboxymethyl)trithiocarbonate (1.00 g, 4.4 mmol) was dissolved in 12.5 mL 1,2-dimethoxyethane (DME) before adding 0.45 grams (4.4 mmol) of triethylamine (TEA). After stirring for five minutes, a small excess of *n*-octylamine (**2a**) (0.64 g, 5.0 mmol) was added. The solution was stirred at 90 °C overnight and subsequently extracted with DCM and water. The organic phase was then dried over magnesium sulfate and concentrated under reduced pressure. The crude product was purified using column chromatography (silicagel, eluent gradient 100:0 > 50:50 heptane:DCM), resulting in pure **ORh** (yellow oil).

861.8 milligrams of product, 79% yield. ^{1}H-NMR (400 MHz, $CDCl_3$): δ (ppm) 4.04-3.89 (m, 4H), 1.62 (p, J = 7.3 Hz, 2H), 1.39-1.18 (m, 10H), 0.87 (t, J = 6.6 Hz, 3H). ^{13}C-NMR (100 MHz, $CDCl_3$): δ (ppm) 201.49, 174.16, 45.10, 35.63, 32.03, 29.39, 29.37, 27.03, 26.98, 22.90, 14.37.

3-(2-ethylhexyl)-2-thioxothiazolidin-4-one (EHRh) (3b)

The same procedure as for **ORh** was used. Now, a small excess of 2'-ethylhexylamine (**2b**) (0.64 g, 5.0 mmol) was added to a solution of 1 gram bis(carboxymethyl)trithiocarbonate (4.4 mmol) and 0.45 grams of TEA (4.4 mmol) in 12.5 mL DME. After purification by column chromatography (silicagel, eluent gradient 100:0 > 50:50 heptane:DCM), pure **EHRh** was obtained as a yellow oil.

902.5 milligrams of product, 83% yield. ^{1}H-NMR (400 MHz, $CDCl_3$): δ (ppm) 3.96 (s, 2H), 3.88 (d, J = 7.4 Hz, 2H), 1.97 (sept, J = 6.4 Hz, 1H), 1.39-1.11 (m, 8H), 0.87 (t, J = 7.4 Hz, 6H). ^{13}C-NMR (100 MHz, $CDCl_3$): δ (ppm) 201.68, 174.31, 48.63, 36.71, 35.22, 30.46, 28.4, 23.87, 22.99, 14.04, 10.51.

(5Z,5'Z)-5,5'-([2,2'-bithiophene]-5,5'-diylbis(methaneylylidene))bis(3-octyl-2-thioxothiazolidin-4-one) (2T-ORh)

2,2'-Bithiophene-5,5'-dicarboxaldehyde (120 mg, 0.54 mmol) and seven drops of piperidine were dissolved in 3 mL chloroform. Next, **ORh** (400 mg, 1.63 mmol) was dissolved in 2 mL chloroform and added to this solution. The solution was allowed to react for four hours at 80 °C and subsequently extracted with DCM and water. The organic phase was then dried over magnesium sulfate and concentrated under reduced pressure. Pure **2T-ORh** was obtained as a dark red solid after precipitation from chloroform in methanol.

150 milligrams of product, 41% yield. ^{1}H-NMR (400 MHz, $CDCl_3$): δ (ppm) 7.82 (s, 2H), 7.42-7.31 (m, 4H), 4.11 (t, J = 7.6 Hz, 4H), 1.71 (p, J = 7.3 Hz, 4H), 1.45-1.18 (m, 20H), 0.88 (t, J = 6.8 Hz, 6H). ^{13}C-NMR (100 MHz, $CDCl_3$): δ (ppm) 191.72, 167.45, 143.18, 138.43, 135.00, 126.45, 124.21, 122.09, 44.96, 31.77, 29.13, 26.99, 26.78, 22.63, 14.09. (Note: several peaks in the ^{13}C-NMR spectrum overlap). MALDI-TOF-MS: [M+] calc: 676.14 found: 676.14

(5Z,5'Z)-5,5'-([2,2'-bithiophene]-5,5'-diylbis(methaneylylidene))bis(3-(2-ethylhexyl)-2-thioxothiazolidin-4-one) (2T-EHRh)

The same procedure as for **2T-ORh** was used. Now, **EHRh** was dissolved in 2 mL chloroform and added to a solution of 120 mg 2,2'-bithiophene-5,5'-dicarboxaldehyde (0.54 mmol) and seven drops of piperidine in 3 mL chloroform. After precipitation, pure **2T-EHRh** was obtained as a dark red solid.

153.1 milligrams of product, 39% yield. ^{1}H-NMR (400 MHz, $CDCl_3$): δ (ppm) 7.81 (s, 2H), 7.39-7.32 (m, 4H), 4.04 (d, *J* = 7.5 Hz, 4H), 2.13-2.00 (m, 2H), 1.43-1.13 (m, 22H), 0.972-0.779 (m, 6H). ^{13}C-NMR spectrum could not be recorded due to insufficient solubility. MALDI-TOF-MS: [M+] calc: 676.14 found: 676.12

5. References

(1) Wan, X.; Li, C.; Zhang, M.; Chen, Y. Acceptor–Donor–Acceptor Type Molecules for High Performance Organic Photovoltaics – Chemistry and Mechanism. *Chem. Soc. Rev.* **2020**, *49* (9), 2828–2842.

(2) Jung, M.; Yoon, Y.; Park, J. H.; Cha, W.; Kim, A.; Kang, J.; Gautam, S.; Seo, D.; Cho, J. H.; Kim, H.; Choi, J. Y.; Chae, K. H.; Kwak, K.; Son, H. J.; Ko, M. J.; Kim, H.; Lee, D.-K.; Kim, J. Y.; Choi, D. H.; Kim, B. Nanoscopic Management of Molecular Packing and Orientation of Small Molecules by a Combination of Linear and Branched Alkyl Side chains. *ACS Nano* **2014**, *8* (6), 5988–6003.

(3) Qu, J.; Mu, Z.; Lai, H.; Chen, H.; Liu, T.; Zhang, S.; Chen, W.; He, F. Alkyl Chain End Group Engineering of Small Molecule Acceptors for Non-Fullerene Organic Solar Cells. *ACS Appl. Energy Mater.* **2018**, *1* (9), 4724–4730.

(4) Lim, E. P3HT-Based Polymer Solar Cells with Unfused Bithiophene–Rhodanine-Based Nonfullerene Acceptors. *Bull. Korean Chem. Soc.* **2020**, *41* (6), 644–649.

(5) Lee, T.; Song, C. E.; Lee, S. K.; Shin, W. S.; Lim, E. Alkyl-Side-Chain Engineering of Nonfused Nonfullerene Acceptors with Simultaneously Improved Material Solubility and Device Performance for Organic Solar Cells. *ACS Omega* **2021**, *6* (7), 4562–4573.

(6) Lee, T.; Eom, Y.; Song, C. E.; Jung, I. H.; Kim, D.; Lee, S. K.; Shin, W. S.; Lim, E. Simple Bithiophene–Rhodanine-Based Small Molecule Acceptor for Use in Additive-Free Nonfullerene OPVs with Low Energy Loss of 0.51 EV. *Adv. Energy Mater.* **2019**, *9* (16),

(7) Holmberg, B. Über Propio-Rhodanine. *Berichte der Dtsch. Chem. Gesellschaft* **1914**, *47* (1), 159–165.

(8) Radi, M.; Botta, L.; Casaluce, G.; Bernardini, M.; Botta, M. Practical One-Pot Two-Step Protocol for the Microwave-Assisted Synthesis of Highly Functionalized Rhodanine Derivatives. *J. Comb. Chem.* **2010**, *12* (1), 200–205.

(9) Qi, F.; Zhang, Y.; Wan, M.; Liu, J.; Huo, L. Enhanced Photovoltaic Performance of Polymer Solar Cells through Design of a Fused Dithienosilolodithiophene Structure with an Enlarged π-Conjugated System. *J. Mater. Chem. C* **2018**, *6* (15), 4208–4216.

(10) Hestand, N. J.; Spano, F. C. Expanded Theory of H- and J-Molecular Aggregates: The Effects of Vibronic Coupling and Intermolecular Charge Transfer. *Chem. Rev.* **2018**, *118* (15), 7069–7163.

(11) Spano, F. C. The Spectral Signatures of Frenkel Polarons in H- and J-Aggregates. *Acc. Chem. Res.* **2010**, *43* (3), 429–439.

(12) Lee, T.; Oh, S.; Rasool, S.; Song, C. E.; Kim, D.; Lee, S. K.; Shin, W. S.; Lim, E. Non-Halogenated Solvent-Processed Ternary-Blend Solar Cells via Alkyl-Side-Chain Engineering of a Non-Fullerene Acceptor and Their Application in Large-Area Devices. *J. Mater. Chem. A* **2020**, *8* (20), 10318–10330.

(13) Yang, Q.; Wang, J.; Zhang, X.; Zhang, J.; Fu, Y.; Xie, Z. Constructing Vertical Phase Separation of Polymer Blends via Mixed Solvents to Enhance Their Photovoltaic Performance. *Sci. China Chem.* **2015**, *58* (2), 309–316.

(14) Wang, J. C.; Ren, X. C.; Shi, S. Q.; Leung, C. W.; Chan, P. K. L. Charge Accumulation Induced S-Shape J–V Curves in Bilayer Heterojunction Organic Solar Cells. *Org. Electron.* **2011**, *12* (6), 880–885.

(15) Finck, B. Y.; Schwartz, B. J. Understanding the Origin of the S-Curve in Conjugated Polymer/Fullerene Photovoltaics from Drift-Diffusion Simulations. *Appl. Phys. Lett.* **2013**, *103* (5), 53306.

(16) Wadsworth, A.; Moser, M.; Marks, A.; Little, M. S.; Gasparini, N.; Brabec, C. J.; Baran, D.;

McCulloch, I. Critical Review of the Molecular Design Progress in Non-Fullerene Electron Acceptors towards Commercially Viable Organic Solar Cells. *Chem. Soc. Rev.* **2019**, *48* (6), 1596–1625.

(17) Park, S. Y.; Song, S.; Yoon, Y. J.; Lee, T. H.; An, N. G.; Walker, B.; Kim, J. Y. Non-Halogenated Diphenyl-Chalcogenide Solvent Processing Additives for High-Performance Polymer Bulk-Heterojunction Solar Cells. *RSC Adv.* **2018**, *8* (69), 39777–39783.

(18) Tang, C.; Chen, S.-C.; Shang, Q.; Zheng, Q. Asymmetric Indenothiophene-Based Non-Fullerene Acceptors for Efficient Polymer Solar Cells. *Sci. China Mater.* **2017**, *60* (8), 707–716.

(19) Fan, H.; Vergote, T.; Xu, S.; Chen, S.; Yang, C.; Zhu, X. A Thieno[3{,}4-b]Thiophene Linker Enables a Low-Bandgap Fluorene-Cored Molecular Acceptor for Efficient Non-Fullerene Solar Cells. *Mater. Chem. Front.* **2018**, *2* (4), 760–767.

Chapter 3: Core engineering in simple octyl *N*-functionalized rhodanine based non-fullerene acceptors

Abstract

Three new and simple octyl-rhodanine based non-fullerene acceptors (NFA) with either a thienothiophene core (**TT-ORh**), a thiophene-furan core (**TF-ORh**), or a bifuran core (**2F-ORh**) were synthesized. Because the solubility of the **TT-ORh** NFA was quite low, its physical properties and photovoltaic performance were not further investigated. For the **TF-ORh** and the **2F-ORh** NFAs, a comparison with the **2T-ORh** NFA was made in terms of physical properties and photovoltaic performance. While the absorption spectra of the furan-based NFAs and the **2T-ORh** NFA were virtually equal in solution, remarkable differences were observed in thin film. After solvent vapor annealing, the absorption behavior of the furan-based NFAs did not change, while the **2T-ORh** went from an H-type to a more J-type aggregation. For **TF-ORh**, the highest efficiency was obtained in the pristine device and was 0.32%. The performance of **2F-ORh** was increased through SVA or addition of a co-solvent and the best device was obtained *via* optimized SVA and was 1.87%. These efficiencies are remarkably lower than for the optimized **2T-ORh** device. These lower efficiencies are probably due to a too large phase segregation as shown with atomic force microscopy (AFM).

1. Introduction

In the previous chapter, two simple bithiophene rhodanine based non-fullerene acceptors were synthesized and the effect of changing side-chains attached to the rhodanine on the optical, electrochemical and photovoltaic properties was investigated. It was found that changing the type of side-chain from an *n*-octyl to a 2'-ethylhexyl has large effect on the thin film aggregation behavior of the molecules. The molecules required different processing conditions to obtain the best device performance. For the **2T-ORh** NFA solvent vapor annealing yielded a 4.74% device and for **2T-EHRh** addition of 2 vol% DPE showed a 5.19% device efficiency.

Besides changes in the acceptor unit, it also interesting to investigate how changes in the core relate to the device performance. An intuitive change in the core is fusing the rings together, so changing from a bithiophene to a thieno[3,2-*b*]thiophene. Thienothiophenes are an often used electron rich building block in the photovoltaic field. In non-fullerene acceptors, thienothiophenes are often used as a π-bridge between the donor unit and the acceptor units.[1-3] To a lesser extent they are used in the donor unit of non-fullerene acceptors.[4-6] The performance of these thienothiophene based non-fullerene acceptors is consistently good and therefore it is interesting to investigate the performance of a simple non-fullerene acceptor with a thienothiophene core. Another intuitive change in the core is a heterocycle substitution. Investigating the effect of heterocycle substitution is a relatively frequently used technique in the photovoltaic field, but mainly in the donor molecule.[7-9] For A-D-A type non-fullerene acceptors there are papers published discussing the effect of heterocycle substitution, yet all these papers feature large and often fused-ring acceptors.[10-12] These papers also all solely discuss the effect of a thiophene-selenophene substitution, while introducing furans in the donor molecules has also proven effective.[9] Therefore, it is interesting to investigate the effect of thiophene-furan substitution in the core of simple A-D-A type non-fullerene acceptors.

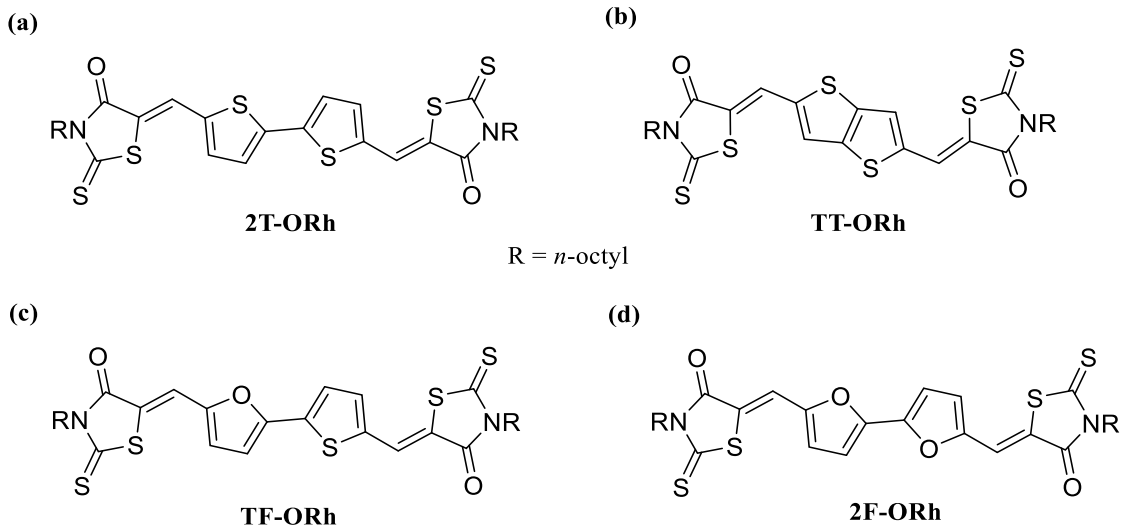

Figure 3.1: Molecular structures of the four non-fullerene acceptors: (a) **2T-ORh**, (b) **TT-ORh**, (c) **TF-ORh** and (d) **2F-ORh**.

In this chapter, three new and simple A-D-A type non-fullerene acceptors will be synthesized and compared to the bithiophene reference (**2T-ORh**). These new NFAs have either a thienothiophene (**TT-ORh**), a thiophene-furan (**TF-ORh**) or a bifuran (**2F-ORh**) core, and all contain octyl *N*-functionalized rhodanines as the acceptor units (**Figure 3.1**). The effect of changes in the core on the optoelectronic properties and photovoltaic performance will be investigated.

2. Results and Discussion

2.1 Synthesis

While the synthesis of the **TT-ORh** NFA was straightforward, the synthesis of the **TF-ORh** and the **2F-ORh** NFAs proved to be more challenging, because for these NFAs the bi-aldehyde starting compounds are not commercially available. To synthesize these compounds several synthetic routes have been attempted. The unsuccessful synthetic routes are discussed in Appendix A. The synthesis of **ORh** is described in chapter 2. All successfully performed synthetic procedures are discussed in more detail in the following subsections and in the Experimental section.

2.1.1 TT-ORh synthesis

The synthesis of **TT-ORh** (**Scheme 3.1**) was performed in the same manner as for the synthesis of **2T-ORh**, which is described in chapter 2. For this NFA, the Knoevenagel condensation was performed in an even lower yield than for **2T-ORh**. The strong aggregation tendency of the rigid and planar thienothiophene lowered the solubility to such an extent that the end product showed a too low solubility in chloroform for use in OPV devices.[13] For this reason, the molecule was not investigated any further.

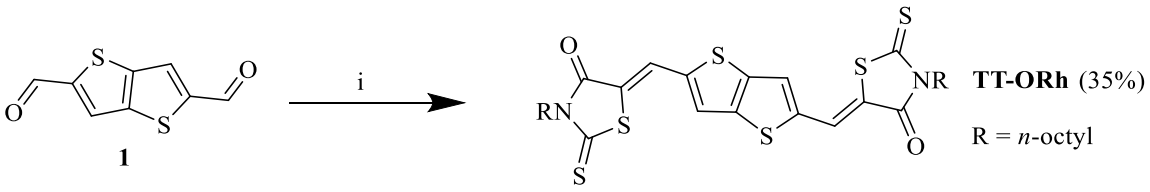

Scheme 3.1: Synthesis of the **TT-ORh** NFA. (i) 3 eq. **ORh**, piperidine, CF, 80 °C. Reaction yields are given between parentheses.

2.1.2 TF-ORh synthesis

In the first step of the synthesis route for **TF-ORh**, the asymmetric bi-aldehyde (**4** in **Scheme 3.2**) was synthesized *via* a Suzuki-Miyaura cross-coupling reaction. For this reaction, several reaction conditions have been screened by performing test reactions, as can be read in Appendix A. A test reaction using the conditions described in **Scheme 3.2** showed a mixture of the desired product, a presumably homo-coupled product and triphenylphosphine. These components were successfully separated by column chromatography, resulting in a pure asymmetric bi-aldehyde in a yield of 24%. Because the yield of the test reaction was quite low but the different components could easily be separated, it was decided to perform the reaction on a larger scale. Unfortunately, the large scale reaction showed to be less efficient with a yield of only 12% after recrystallization. Despite several purification attempts, about 3% of presumably homo-coupled side-product remained.

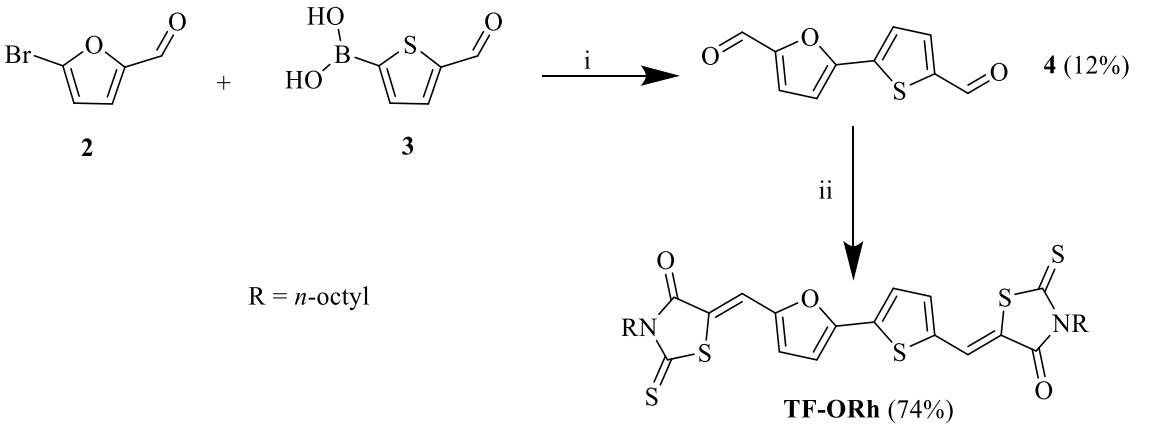

Scheme 3.2: Synthesis of the **TF-ORh** NFA. (i) $Pd(PPh_3)_4$, K_2CO_3 (*aq*), Tol./Meth. (65:35), 100 °C ; (ii) 4 eq. **ORh**, piperidine, CF, 80 °C. Reaction yields are given between parentheses.

Despite the small amount of impurity in de bi-aldehyde product, the second step of the synthetic route, the Knoevenagel condensation, was performed. This time anhydrous chloroform was used as a solvent and a larger excess of rhodanine was added to the reaction mixture, this could explain the higher yield obtained in this reaction. After precipitation and recrystallization, the amount of impurity decreased to only 1%.

2.1.3 2F-ORh synthesis

The synthesis of **2F-ORh** was tried by following the synthetic procedure in **Scheme 3.2**, but now using (5-formylfuran-2-yl)boronic acid instead of (5-formylthiophen-2-yl)boronic acid (**3**) in the Suzuki-Miyaura cross-coupling reaction. Unfortunately, also for this compound the Suzuki-Miyaura cross-coupling reaction resulted in very little and impure bi-aldehyde product. Consequently, a new route was followed for the synthesis of **2F-ORh** (**Scheme 3.3**). In this route, the rhodanine group (**ORh**) is first attached to the starting compound, which avoids the presence of aldehydes in the coupling reaction. The protection of the aldehydes is chosen, because it is believed that the aldehydes impede certain steps in the catalytic cycle. The Knoevenagel condensation was again performed in a good yield of 76%.

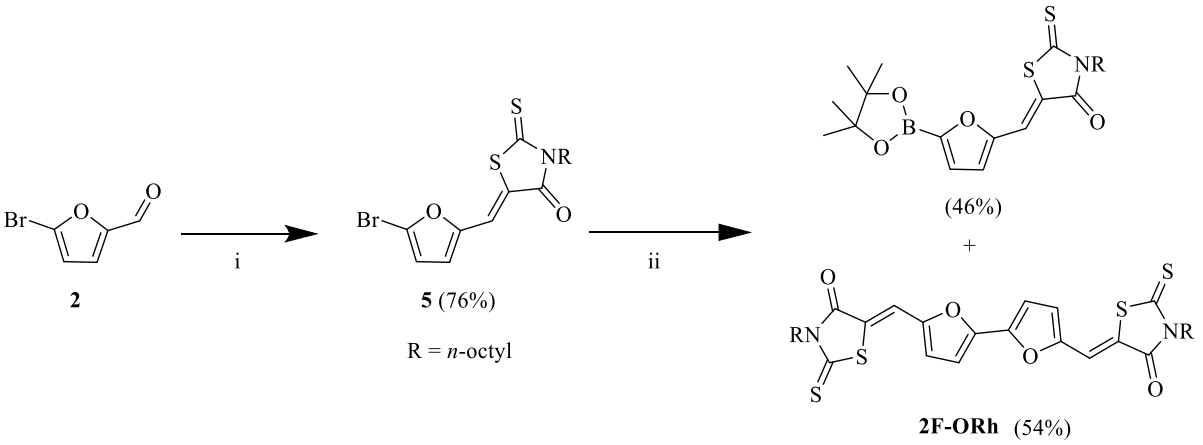

Scheme 3.3: Synthesis of the **2F-ORh** NFA. (i) 2 eq. **ORh**, piperidine, CF, 80 °C ; (ii) B_2Pin_2, $Pd(dppf)Cl_2$, KOAc, Dioxane, 110 °C. Reaction yields are given between parentheses.

In the second step in **Scheme 3.3** a Miyaura borylation was attempted.[14,15] From the literature it is well known that weak bases, such as potassium acetate, should give the borylated compound in high yields.[14,15] Surprisingly, in our case a small scale test reaction showed a 50/50 mixture of the targeted borylated compound and the homo-coupled product. However, because the homo-coupled product is also the desired final NFA, no additional Suzuki-Miyaura reaction between compound **5** and the borylated compound was needed. In the literature, it is also well known that symmetric bi-aryls can efficiently be synthesized by one-pot-two-step borylation/Suzuki-Miyaura CC reactions that use a stronger base like potassium carbonate and 0.5 equivalents of bis(pinacolato)diboron instead of 2 equivalents.[16-18] Using this approach, attempts have been made to further increase the ratio of formed homo-coupled product to borylated compound.[16-18] However, full completion could not be achieved for these reactions. Therefore, the decision was made to scale-up the initial test-reaction and to isolate the homo-coupled product from there. The homo-coupled product was again formed in about 50% yield and was successfully isolated.

2.2 Optical and electrochemical properties

The optical properties of the **TF-ORh** and **2F-ORh** NFAs were investigated by UV-vis-NIR absorption spectroscopy in chloroform solution and in thin film (**Figure 3.2**). The spectra of **2T-ORh** were reproduced from chapter 2 for comparison.

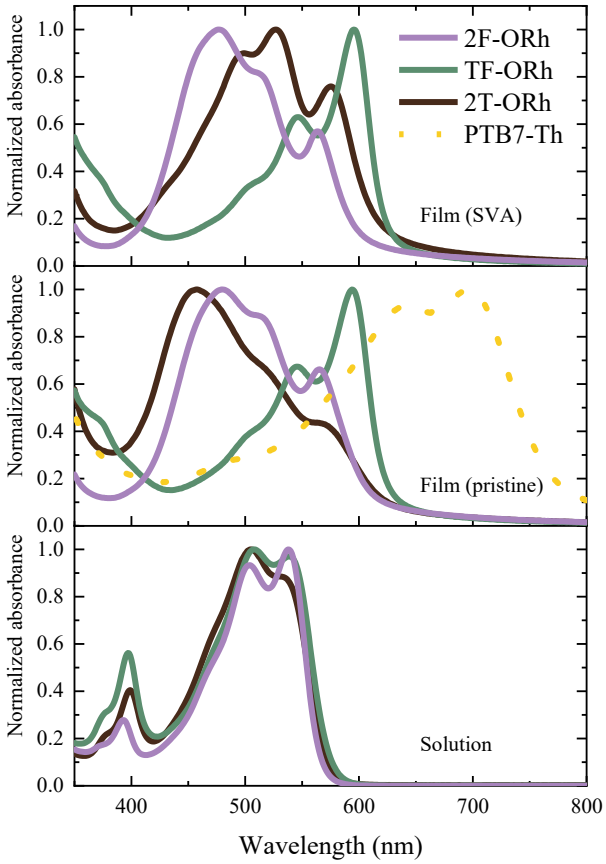

Figure 3.2: (a) Normalized UV-vis-NIR absorption spectra of **2T-ORh**, **TF-ORh** and **2F-ORh** in chloroform solution, as pristine thin film and as solvent vapor annealed film. The absorption spectrum of PTB7-Th in thin film is also included.

In solution, all three molecules show similar absorption spectra, albeit with two small differences. The first difference lies in the intensity ratio between the vibronic peaks around 505 and 535 nm. In **2T-ORh**, the peak around 505 nm has the highest intensity, while in **TF-ORh** the intensities are roughly equal and in **2F-ORh** the peak around 535 nm has the highest intensity. Besides the difference in intensity of the peaks in the intramolecular charge transfer (ICT) region (420-600 nm), there is also a difference in intensity of the peak attributed to localized π-π* transitions around 400 nm. This peak has the highest intensity for the **TF-ORh** NFA, the lowest intensity for the **2F-ORh** NFA and an intermediate intensity for the **2T-ORh** NFA.

Table 3.1: Optical and electrochemical properties of **2T-ORh**, **TF-ORh** and **2F-ORh**.

	[a] 2T-ORh	TF-ORh	2F-ORh
[b] $E_{g,opt}^{sol}$ [eV]	2.16	2.16	2.19
[b] $E_{g,opt}^{film,\ pristine}$ [eV]	1.97	1.98	2.03
[b] $E_{g,opt}^{film,\ SVA}$ [eV]	2.00	1.99	2.06
λ_{max}^{sol} [nm]	502	508	540
$\lambda_{max}^{film,\ pristine}$ [nm]	457	595	481
$\lambda_{max}^{film,\ SVA}$ [nm]	527	596	478
[c] E_{ox} [V]	0.88	0.73	0.70
[c] E_{red} [V]	-1.25	-1.23	-1.32
[d] E_{HOMO} [eV]	-5.68	-5.53	-5.50
[d] E_{LUMO} [eV]	-3.55	-3.57	-3.48
$E_{g,SWV}$ [eV]	2.13	1.96	2.02

[a] Reproduced from chapter 2. [b] $E_{g,opt} = 1240/\lambda_{onset}$ (eV). [c] *vs.* Fc/Fc^+. [d] Determined using a work-function of −4.8 eV for Fc/Fc^+ versus vacuum.

In pristine film, the **2F-ORh** NFA shows similar behavior as **2T-ORh** with a broad and clearly blue-shifted absorption maximum at 481 nm and a weak red-shifted absorption at 570 nm. This suggests that the molecule is predominantly in an H-type aggregation in the as-cast film. The absorption maximum of the **2F-ORh** spectrum is however less blue-shifted than for the **2T-ORh** spectrum and the red-shifted peak at 570 nm is of a higher intensity. Surprisingly, in pristine film the **TF-ORh** NFA shows only J-type aggregation with a red-shifted absorption maximum at 595 nm and an increased absorption around 350 nm. It can be seen that for this molecule there is little absorption in the 400-550 nm range, which could decrease the attainable currents. Where for **2T-ORh** a large red-shift in the absorption maximum is observed after solvent vapor annealing (SVA), no significant change in absorption is seen for both furan-based NFAs after SVA. The optical bandgaps in pristine film, estimated from the onset of absorption, are similar for all three molecules as they are 1.97, 1.98 and 2.03 eV for **2T-ORh**, **TF-ORh** and **2F-ORh** respectively. These bandgaps did not change significantly after SVA. All optical characteristics are summarized in **Table 3.1**.

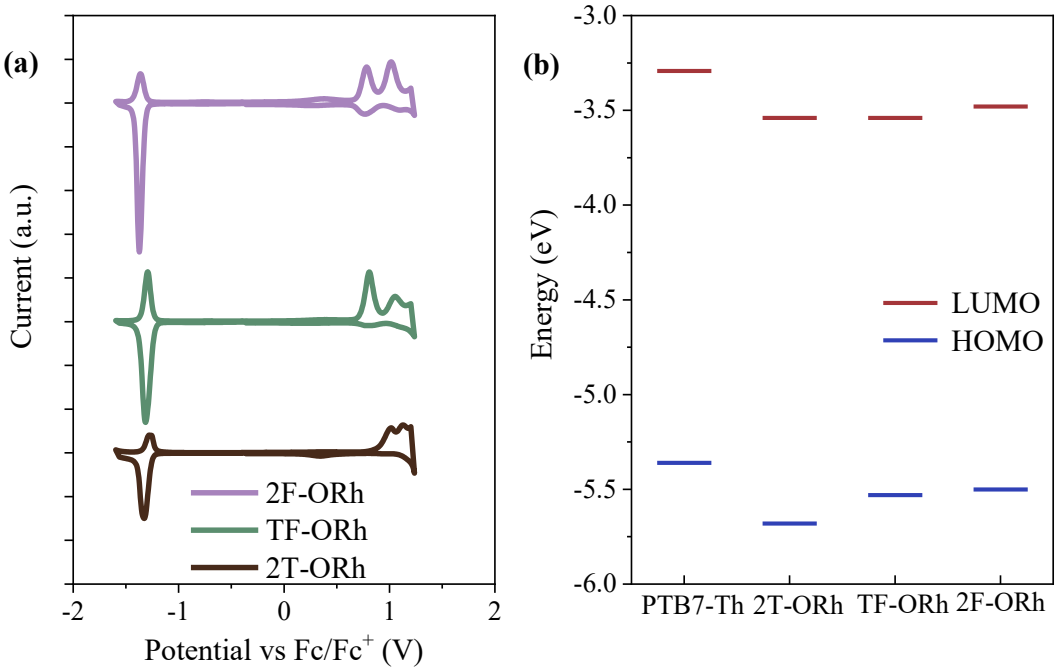

Figure 3.3: (a) Square-wave voltammograms of the **2T-ORh**, **TF-ORh** and **2F-ORh** NFAs in thin film. (b) Frontier orbital energy levels of the three NFAs and PTB7-Th, calculated from the oxidation and reduction onsets relative to the vacuum level.

The frontier molecular orbital energy levels (HOMO and LUMO) of the **TF-ORh** and **2F-ORh** NFAs were determined using square-wave voltammetry (SWV) in thin film. The voltammogram of **2T-ORh** was reproduced from chapter 2 for comparison. The recorded voltammograms are depicted in **Figure 3.3a** and the determined energy levels and the corresponding bandgaps are listed in **Table 3.1**. It should be noted that the thin-film measurements of the NFAs are not reversible, likely because the small molecules start to dissolve in acetonitrile upon charging. The reversibility was verified by measuring SWV in solution. It can be seen that the HOMO energy levels of both furan-based NFAs are up-shifted compared to the bithiophene-based NFA. A shift in the HOMO energy is expected, because in these A-D-A type molecules the HOMO is mainly situated on the donor unit. The higher lying HOMO levels for substitution of thiophene with furan are consistent with previously reported papers about thiophene/furan substitution.[19-21] For the **2F-ORh** an upshifted LUMO level is also visible. In **Figure 3.3b**, the energy levels of both NFAs are compared with the energy levels of the PTB7-Th polymer, which were also determined in thin film. For both furan-based molecules the HOMO-HOMO offsets with the PTB7-Th polymer have decreased compared to the HOMO-HOMO offset for **2T-ORh**. Now, the offsets are 0.17 and 0.14 eV for **TF-ORh** and **2F-ORh** respectively. For **2F-ORh**, also the LUMO-LUMO offset has decreased to 0.19 eV compared to the offset for **2T-ORh**. Whereas the LUMO-LUMO

offset for **TF-ORh** has slightly increased and is now 0.28 eV. This shows that there might be some differences in charge generation efficiency between the molecules, where the **2T-ORh** NFA shows the largest driving force for charge generation. There might also be a difference in maximum attainable open circuit voltages (V_{oc}), where **2F-ORh** shows the largest $LUMO_A/HOMO_D$ difference.

2.3 Photovoltaic devices

The photovoltaic performance of the **TF-ORh** and **2F-ORh** NFAs was characterized in a bulk-heterojunction photovoltaic device, using PTB7-Th as the electron donor. All devices were fabricated in an inverted structure (ITO/ZnO/PEIE/PTB7-Th:NFA (1:2)/MoO_3/Ag). The active layer was spin coated at 1500 rpm, yielding uniform layers of approximately 100 nm thick. Herefore, solutions in chloroform with a total solid concentration of 15 mg mL^{-1}, *i.e.* 5 mg mL^{-1} PTB7-Th and 10 mg mL^{-1} acceptor, were prepared. Similar to chapter 2, we investigate how the performance of the photovoltaic devices for the furan-based NFAs is influenced by solvent vapor annealing as post-treatment and by incorporation of DPE as a co-solvent. All photovoltaic results for **TF-ORh** and **2F-ORh** are compared to the results of **2T-ORh** obtained in chapter 2.

2.3.1 Optimization by solvent vapor annealing

In chapter 2, it was shown that solvent vapor annealing (SVA) is an effective way to enhance the device performance, probably through an increased domain crystallinity. In that chapter, the solvent vapor annealing conditions were systematically optimized in function of solvent and time. This optimization was again performed for the devices in this chapter, but here only the optimized results will be shown.

Table 3.2: Photovoltaic characteristics of **2T-ORh**, **TF-ORh** and **2F-ORh** based devices processed with or without solvent vapor annealing.

Acceptor	SVA	[b] J_{sc} [mA cm^{-2}]	V_{oc} [V]	FF	[b] PCE [%]
[a] **2T-ORh**	No	9.21 (7.46)	0.84	0.31	2.37 (1.92)
	45s, *o*-DCB	10.50 (9.92)	1.04	0.46	5.04 (4.74)
TF-ORh	No	1.66 (1.27)	0.98	0.26	0.43 (0.32)
	15s, *o*-DCB	1.34 (1.14)	0.98	0.25	0.33 (0.28)
2F-ORh	No	3.34 (2.56)	1.00	0.29	0.96 (0.74)
	45s, *o*-DCB	5.86 (5.14)	1.07	0.34	2.13 (1.87)

[a] Reproduced from chapter 2. [b] Value obtained by integrating the EQE with the AM1.5G spectrum is given between parentheses.

As discussed in chapter 2 and again shown in **Figure 3.4a**, the *J-V* curve of the pristine **2T-ORh** device shows a large S-shape. Interestingly, in the *J-V* curve of the pristine **2F-ORh** device this S-shape is only visible to a small extent and not visible at all in the pristine **TF-ORh** device (**Figure 3.4c** and **3.4e**). The fact that there is little to no S-shape in the *J-V* curves for the pristine devices with the furan-based NFAs is probably the reason for the higher V_{oc}s in these devices. In **Table 3.2** it can be seen that devices based on **TF-ORh** have a very poor short-circuit current (J_{sc}), which decreases after 15 seconds of solvent vapor annealing. With longer SVA times, it is found that the device performance drops even more, due to decreasing J_{sc} and V_{oc}. The poor complementary absorption as shown in **Figure 3.2** could contribute to the low J_{sc} in the **TF-ORh** based devices. Interestingly, the EQE of the **TF-ORh** devices (**Figure 3.4d**) shows the same increased absorption around 350 nm as in the UV-vis-NIR absorption spectra. For **2F-ORh**, the pristine device also shows a poor efficiency owing to a low J_{sc} and a high series resistance, but opposed to **TF-ORh** the device performance did increase after SVA. Through an increase in all three characterization variables, the PCE increased from 0.74 to 1.87%. As shown in the SWV results, the **2F-ORh** NFA has the largest $LUMO_A/HOMO_D$ difference, which could explain the higher open-circuit voltage found in the solvent vapor annealed device. When comparing the three EQE spectra (**Figure 3.4b/d/f**), it can be seen that for both the **2T-ORh** and the **2F-ORh** the channel II photocurrent contribution has increased after SVA, whereas the EQE of **TF-ORh** does not show any noticeable differences after SVA.

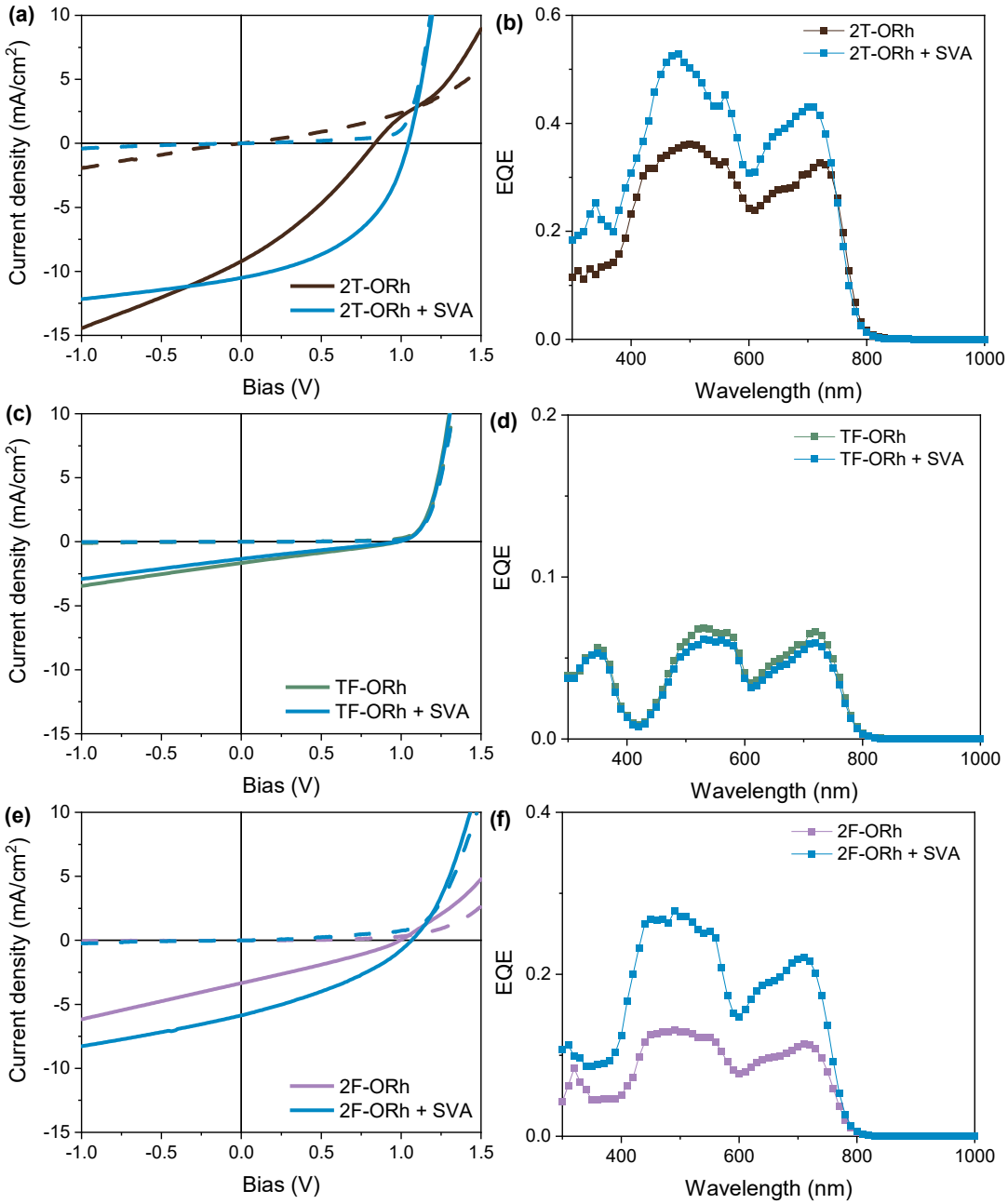

Figure 3.4: (a) *J-V* characteristics in the dark (dashed lines) and under AM1.5G illumination (solid lines) of photovoltaic devices based on **2T-ORh** in pristine film and under optimized SVA conditions. (b) Corresponding EQE spectra of (a). (c) *J-V* characteristics in the dark (dashed lines) and under AM1.5G illumination (solid lines) of photovoltaic devices based on **TF-ORh** in pristine film and under SVA conditions. (d) Corresponding EQE spectra of (c). (e) *J-V* characteristics in the dark (dashed lines) and under AM1.5G illumination (solid lines) of photovoltaic devices based on **2F-ORh** in pristine film and under optimized SVA conditions. (f) Corresponding EQE spectra of (e). Please note the difference in EQE scale between the three EQE spectra shown.

2.3.2 Co-solvent optimization

In chapter 2, it was shown that addition of a co-solvent to the casting mixture leads to an increased device performance, likely through enhancement of the crystallinity in the domains. The optimal concentration of diphenyl ether (DPE) was systematically determined, but will not be shown here.

Table 3.3: Photovoltaic characteristics of **2T-ORh**, **TF-ORh** and **2F-ORh** based devices processed with or without co-solvent.

Acceptor	Co-solvent	[b] J_{sc} [mA cm^{-2}]	V_{oc} [V]	FF	[b] PCE [%]
[a] **2T-ORh**	No	9.21 (7.46)	0.84	0.31	2.37 (1.92)
	2 vol% DPE	8.17 (7.69)	1.02	0.49	4.11 (3.85)
TF-ORh	No	1.66 (1.27)	0.98	0.26	0.43 (0.32)
	1 vol% DPE	0.23	0.26	0.27	0.02
2F-ORh	No	3.34 (2.56)	1.00	0.29	0.96 (0.74)
	0.5 vol% DPE	3.77 (3.38)	1.03	0.33	1.29 (1.15)

[a] Reproduced from chapter 2. [b] Value obtained by integrating the EQE with the AM1.5G spectrum is given between parentheses.

As discussed in chapter 2, addition of DPE in the casting solvent increases the performance of the **2T-ORh** based device, mainly by increasing the V_{oc} and the FF. Because the J_{sc} in the **2T-ORh** device with 2 vol% of DPE is relatively unaffected compared to the pristine **2T-ORh** device (**Table 3.3**), devices made by addition of 2 vol% of DPE do not outperform the solvent vapor annealed device (**Table 3.2**). This same type of behavior is found for the **2F-ORh** based devices, where all three characterization variables increase by the addition of 0.5 vol% of DPE, but the J_{sc} does not reach the same values as it does for the solvent vapor annealed device. Also in this device it can be seen that the incorporation of DPE causes the S-shape in the *J-V* curve to disappear (**Figure 3.5e**), giving rise to a large decrease in series resistance. In the EQE spectra of the **2F-ORh** devices (**Figure 3.5f**) there is no shift between the onsets, in contrast to the EQE spectra of the **2T-ORh** devices (**Figure 3.5b**). Probably this is due to the lower amount of DPE added to the casting solution. For the **TF-ORh** based device, incorporation of DPE in the casting solution is detrimental for the device performance. Both the J_{sc} and the V_{oc} decrease to a large extent and from **Figure 3.5c** it can be seen that addition of the co-solvent leads to an almost flat *J-V* curve. This indicates that charge recombination prevails over charge collection in this device. For this reason, no EQE spectrum could be recorded for this device.

A possible explanation for the low J_{sc} in the furan-based devices could be a decreased electron-mobility, as found by Hendsbee *et al*.[20] In their study they show that the hole mobility of a simple A-D-A type molecule, consisting of a bithiophene core and phtalimide accepting groups, increases when the thiophene units are substituted with furan units. On the other hand, they find that this substitution also results in a complete loss of electron mobility, which they attribute to the loss of degeneracy in the LUMOs.

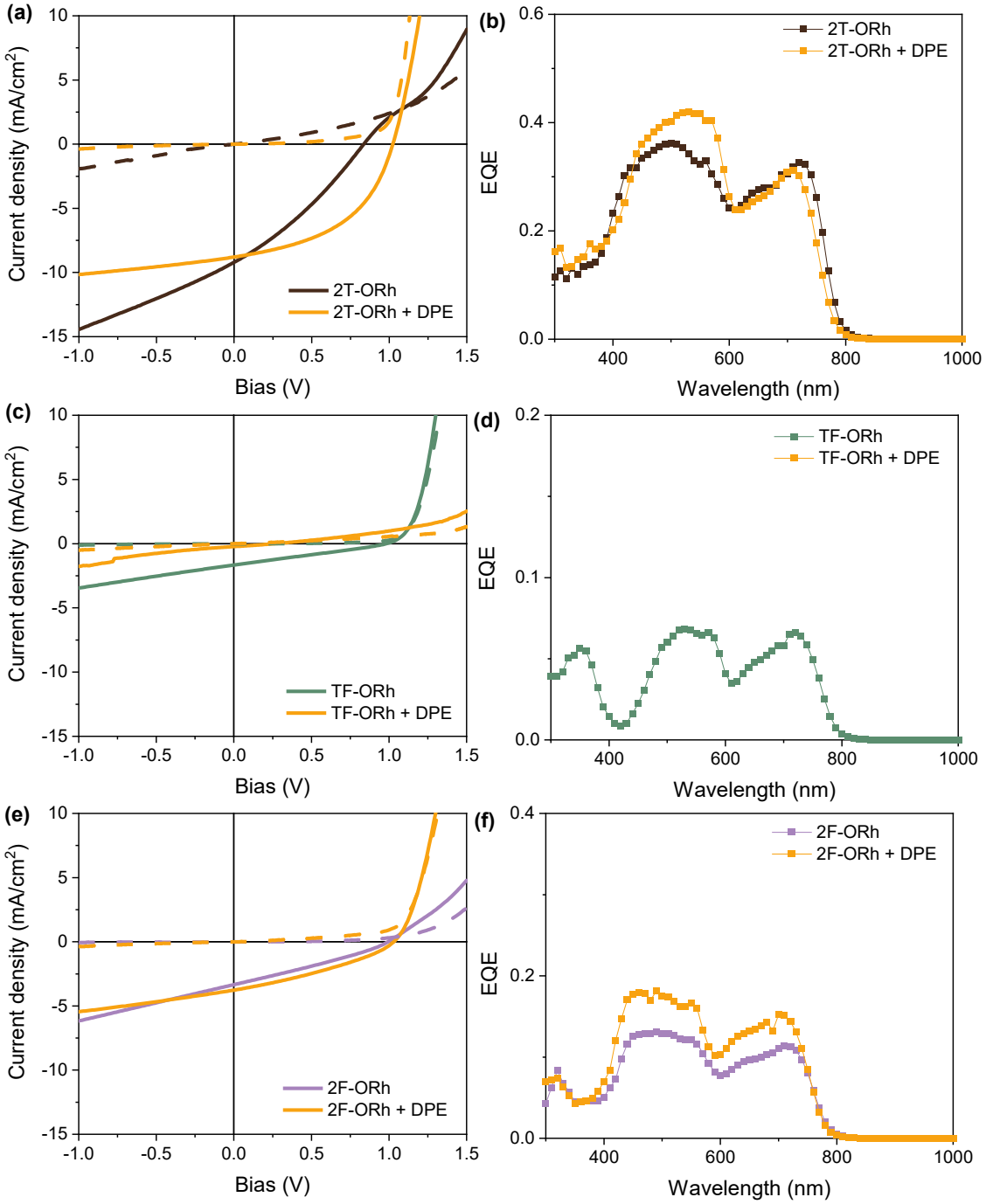

Figure 3.5: (a) *J-V* characteristics in the dark (dashed lines) and under AM1.5G illumination (solid lines) of photovoltaic devices based on **2T-ORh** in pristine film and under optimized co-solvent conditions. (b) Corresponding EQE spectra of (a). (c) *J-V* characteristics in the dark (dashed lines) and under AM1.5G illumination (solid lines) of photovoltaic devices based on **TF-ORh** in pristine film and under co-solvent conditions. (d) Corresponding EQE spectra of (c), the EQE of the co-solvent could not be recorded. (e) *J-V* characteristics in the dark (dashed lines) and under AM1.5G illumination (solid lines) of photovoltaic devices based on **2F-ORh** in pristine film and under optimized co-solvent conditions. (f) Corresponding EQE spectra of (e). Please note the difference in EQE scale between the three EQE spectra shown.

2.4 Morphology

In order to get some insight into why the photovoltaic performance of the furan-based NFAs is much lower than the performance of their bithiophene counterpart, the morphology of the pristine and solvent vapor annealed blend films was studied by atomic force microscopy (AFM). The resulting AFM images

in height and phase mode are shown in **Figure 3.6**. The studied blends were made with a different PTB7-Th batch than used in the photovoltaic devices.

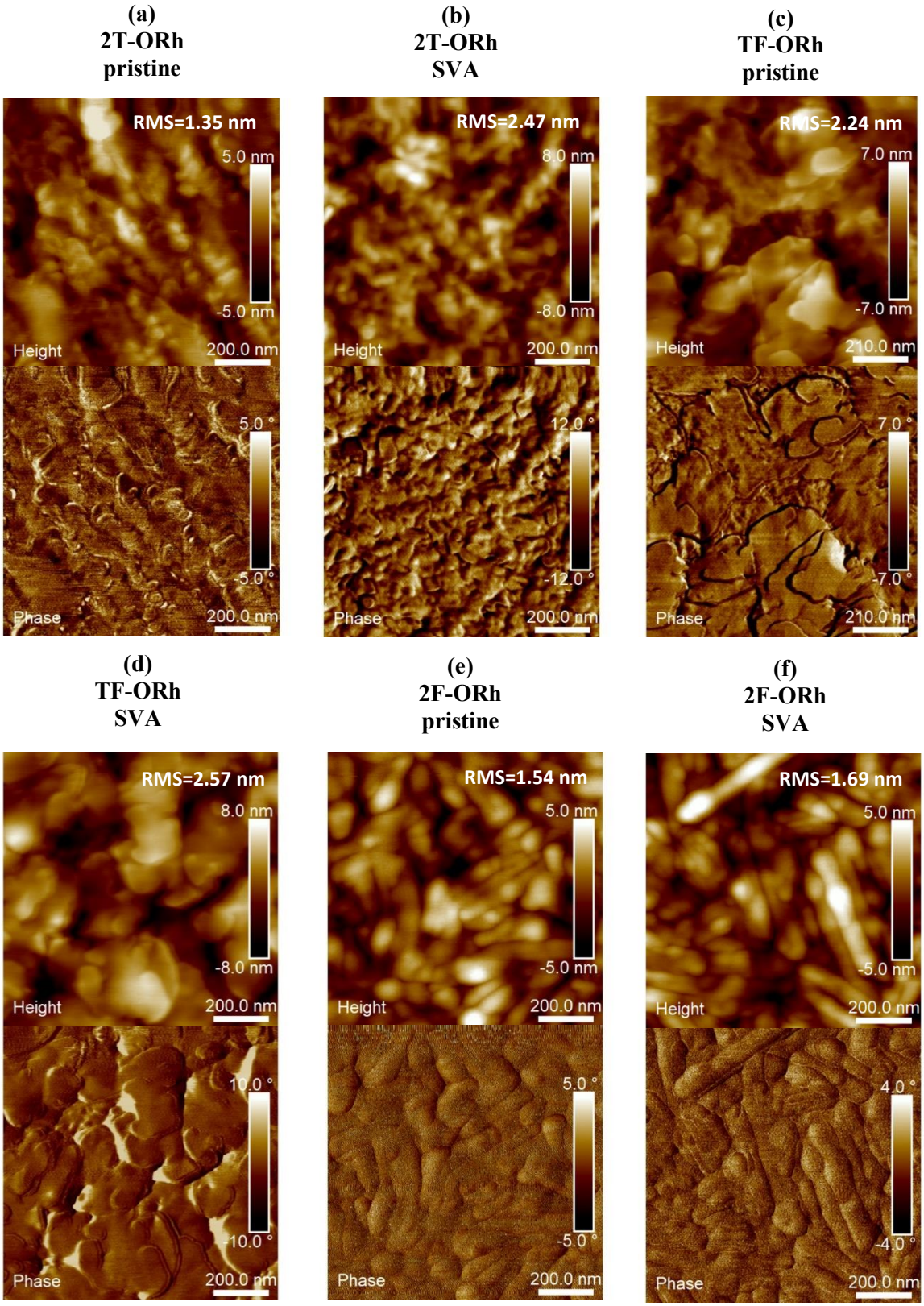

Figure 3.6: AFM height, with the roughness given in top-right corner, (top) and phase (bottom) images (1 x 1µm) of blends for: pristine **2T-ORh** (a), SVA **2T-ORh** (b), pristine **TF-ORh** (c), SVA **TF-ORh** (d), pristine **2F-ORh** (e) and SVA **2F-ORh** (f). SVA was performed under the optimized conditions that are described in the main text.

The AFM images of the blends with **2T-ORh** are only shown as a comparison (**Figure 3.6a&b**), since they were already discussed in chapter 2. The height image of the pristine **TF-ORh** blend shows plateau regions and therefore has a relatively large root-mean-square (RMS) roughness of 2.24 nm (**Figure 3.6c**). The size of these plateaus indicate a too large phase segregation for efficient charge generation. After solvent vapor annealing (**Figure 3.6d**) the images are relatively equal to the pristine film and only the roughness has slightly increased (2.57 nm). The equality of the films matches well with the equality of the *J-V* curves before and after SVA. The slightly larger roughness could indicate an even more extended phase segregation, which could explain the lower J_{sc} in the annealed device. For **2F-ORh**, more defined features are visible in the pristine blend (**Figure 3.6e**). These features are smaller compared to the **TF-ORh** images, yet still too large for efficient charge generation. After SVA (**Figure 3.6f**), the roughness of the **2F-ORh** blend has increased from 1.54 to 1.69 nm and clear elongated structures have become visible. The clearly visible structures and increased roughness suggest more crystalline domains. The higher domain crystallinity is probably a reason for the observed increase in J_{sc} and FF in the solvent vapor annealed device. When comparing the solvent vapor annealed **2T-ORh** and **2F-ORh** blend films, the larger domains in the **2F-ORh** blend film are clearly visible. Additionally, the annealed **2T-ORh** blend has a higher surface roughness, which might indicate a higher crystallinity. The smaller, yet more crystalline domains in the **2T-ORh** blend film could explain the superior performance of the annealed **2T-ORh** device.

3. Conclusion and Outlook

In this chapter, three new octyl-rhodanine based NFAs with thienothiophene, thiophene-furan or bifuran as core units were successfully synthesized. The alkyl side-chains were found to be too short to sufficiently solubilize the fused core of the **TT-ORh** NFA and this molecule was therefore not characterized any further. The synthesis of the furan-based NFAs proved difficult and several synthetic routes have been attempted. The photophysical and photovoltaic properties of the two furan-based NFAs were compared to the bithiophene reference (**2T-ORh**).

The thin film UV-vis-NIR absorption spectra show remarkable differences between the two furan-based NFAs, while only one atom is changed. The **TF-ORh** NFA shows a clear J-type aggregation, while the **2F-ORh** NFA shows mainly an H-type aggregation. The absorption profile of both furan-based NFAs does not significantly change after SVA, whereas the absorption profile of **2T-ORh** shows a change from H- to more J-type aggregates. The optical bandgap for **TF-ORh** and **2F-ORh** after solvent vapor annealing was determined *via* the absorption onset in the UV-vis-NIR spectra, resulting in bandgaps of 1.99 and 2.06 eV respectively.

Square-wave voltammetry measurements showed that substituting thiophene core units for furan core units in octyl-rhodanine based NFAs raises the HOMO energy level. For **2F-ORh**, the LUMO level also shifts to a slightly higher energy level compared to the LUMO level of **2T-ORh**. These shifts cause a decreased energy level offset with PTB7-Th, which could lead to a lower tendency for charge generation. However, the larger $LUMO_A/HOMO_D$ difference found for **2F-ORh** could lead to an increased V_{oc}.

Photovoltaic devices were fabricated and optimized *via* the use of DPE as co-solvent or *via* solvent vapor annealing. The pristine **TF-ORh** device showed a poor efficiency of only 0.32%, which worsened by the use of DPE or by solvent vapor annealing. AFM images showed a large degree of phase segregation, resulting in too large domains for charge generation. Pristine **2F-ORh** based devices showed a slight S-shape in the *J-V* curve. By SVA or addition of DPE in the casting solution this S-shape disappeared, resulting in an increased device efficiency. The best **2F-ORh** based device was obtained by solvent vapor annealing the as-cast device for 45s in *o*-DCB, leading to a 1.87% efficiency. AFM showed large elongated structures in both the pristine and solvent annealed blend, which could

explain the low J_{sc}. By SVA the crystallinity was probably increased, indicating better charge transport properties.

To improve the device performance for both **TF-ORh** and **2F-ORh** based devices other co-solvents could be examined. These co-solvents should be chosen to decrease the domain size and therefore increase the charge generation within the device. In order to say more about the crystallinity and aggregation behavior of the active layer, grazing-incidence wide-angle X-ray scattering could be performed. Charge mobility measurements could help support the finding of Hendsbee *et al.* that substituting thiophene for furan is detrimental for the electron mobility.[20]

4. Experimental

4.1 Materials and Methods

Thieno[3,2-*b*]thiophene-2,5-dicarboxaldehyde was purchased from TCI Europe N.V, PTB7-Th came from 1-Materials and dry toluene was bought from Alpha Aesar. All other chemicals and solvents were purchased from Sigma-Aldrich co or VWR. 1,4-Dioxane was dried over 4 Å molecular sieves prior to use. All other commercially available solvents and reactants were used without further purification. All synthetic procedures were performed under a nitrogen atmosphere.

^{1}H and ^{13}C NMR spectra were measured on a Bruker Avance III spectrometer at 400 and 100 MHz respectively. Chemical shifts are reported with respect to tetramethylsilane as internal standard. Molecular weights of the **TF-ORh** and **2F-ORh** NFAs were determined using matrix assisted laser desorption ionization time-of-flight (MALDI-TOF) mass spectroscopy on a Bruker Autoflex Speed spectrometer.

Solution and film UV-vis-NIR spectra were recorded on a Perkin Elmer Lambda 1050 spectrophotometer. Dilute solutions of **TF-ORh** and **2F-ORh** were prepared in chloroform and films were prepared by spin coating a 6 mg mL^{-1} solution on a glass substrate at 1500 rpm. Solvent vapor annealed films were prepared from the same solution, after which the films were subjected to 15 and 45 seconds of *o*-DCB vapor for **TF-ORh** and **2F-ORh** respectively.

Square-wave voltammetry (SWV) was performed in thin film under inert atmosphere using a Biologic VSP potentiostat. All films were prepared by dip coating a flame-cleaned platinum working electrode using a stock solution of 2 mg mL^{-1} PTB7-Th in chloroform or a 4 mg mL^{-1} solution of **TF-ORh** or **2F-ORh** in dichloromethane. A silver rod was used as counter electrode and a silver chloride coated silver rod (Ag/AgCl) was used as quasi-reference electrode. A 0.1 M tetrabutylammonium hexafluorophosphate ($TBAPF_6$) solution in acetonitrile was used as electrolyte. All measurements were reported against ferrocene/ferrocenium (Fc/Fc^+) as reference, with E_{Fc/Fc^+} set at −4.8 eV *vs*. vacuum. Measurements were performed with a 20 mV pulse height, 20 ms pulse width and 5 mV step height.

Photovoltaic devices were fabricated on pre-patterned indium tin oxide (ITO) glass substrates (Naranjo Substrates). The substrates were cleaned by sonication in acetone, followed by scrubbing with a sodium dodecyl sulfate solution (99%, Acros). After sonication in the same sodium dodecyl sulfate solution, the substrates were rinsed with deionized water and underwent a final sonication in 2-propanol. To finish the cleaning, the substrates underwent a 30 minute UV-ozone treatment. A ZnO electron transport layer (ETL) was deposited onto the cleaned substrates via a sol gel method by spin coating a precursor solution. The precursor solution was prepared by dissolving 109.72 mg of zinc acetate dehydrate in 1 mL 2-methoxyethanol and 30.2 µL ethanolamine. This solution was stirred for at least 1 hour at room temperature after which it was spin coated at 4000 rpm in ambient air and immediately annealed for 5 minutes at 150 °C, resulting in a 40 nm ZnO layer. A commercially available PEIE solution of 37 wt% was further diluted in ethanol until a total mass fraction of 0.1 wt% was reached. This solution was cast on the ZnO coated substrates by spin-coating at 4000 rpm in air to yield a thin layer. This layer was

annealed for 10 minutes at 100 °C. For the active layer, the PTB7-Th donor polymer and rhodanine-based acceptor molecule were mixed in a 1:2 (D:A) weight ratio and dissolved in chloroform at a total solids concentration of 15 mg mL^{-1}. This solution was heated to and kept at 60 °C under continuous stirring for 1 hour and cooled down to room temperature prior to spin coating. The active layer was spin coated at 1500 rpm to obtain an optimal layer thickness of around 100 nm. The blend films were subsequently subjected to solvent vapor annealing using different solvents and annealing times as described in the results section. This was carried out by placing 200 µL of the desired solvent in a petridish and leaving this closed for 1 minute to introduce solvent vapor. The substrate was then placed on top of an elevated stage in this petridish for the desired amount of time. The back electrode layers, MoO_3 (10 nm) followed by Ag (100 nm), were deposited by thermal evaporation in a vacuum chamber at ~ 6×10^{-7} mbar. The active area of the photovoltaic devices was determined by the intersection of the ITO pattern and the back contacts. The intersecting areas resulted in two squares of 9 mm^2 and two squares of 16 mm^2.

J-V and EQE measurements were performed under N_2 atmosphere. In order to photodope the ZnO and MoO_3 layers, the devices were illuminated for 10 minutes with UV light prior to *J-V* measurements. Current density – voltage (*J-V*) characteristics were recorded with a 4 point probe Keithley 2400 source meter under illumination with a tungsten-halogen lamp. To provide a 1000 W m^{-2} AM1.5G illumination, the light was filtered through a Schott GG385 UV filter and a Hoya LB120 daylight filter. Accurate short-circuit current density (J_{sc}) values were obtained by integrating recorded external quantum efficiency (EQE) spectra with the AM1.5G solar spectrum. The EQE measurements were performed on a custom-made setup consisting of a 50W tungsten-halogen lamp (Osram 64610), a monochromator (Oriel, Cornerstone 130), a mechanical chopper (Stanford Research Systems, SR540), a pre-amplifier (SR570), a lock-in amplifier (SR830) and a Thorlabs high intensity LED operating at 530 nm as a bias light. Although the setup was in ambient air, the substrates were kept encapsulated in a N_2 filled box equipped with a quartz window. A calibrated silicon cell was used as a reference prior to both the *J-V* and the EQE measurements. Lastly, the active layer thickness of the substrates were determined on a Veeco Dektak 150 profilometer.

The morphology of the films was characterized by atomic force microscopy (AFM), using a Dimension 3100 in tapping mode. For this, blend films were prepared by mixing the PTB7-Th donor polymer and the rhodanine-based acceptors in a 1:2 (D:A) weight ratio and dissolving them in chloroform at a total solids concentration of 15 mg mL^{-1}. The films were spin coated on a glass substrate at 1500 rpm in an N_2 filled glove-box.

4.2 Synthesis

The octyl substituted rhodanine (**ORh**) was synthesized according to the procedure described in chapter 2 and will not be discussed here.

(5Z,5'Z)-5,5'-(thieno[2,3-*b*]thiophene-2,5-diylbis(methaneylylidene))bis(3-octyl-2-thioxothiazolidin-4-one) (TT-ORh)

Thieno[3,2-*b*]thiophene-2,5-dicarboxaldehyde (106 mg, 0.54 mmol) and seven drops of piperidine were dissolved in 3 mL chloroform. Next, **ORh** (400 mg, 1.63 mmol) was dissolved in 2 mL chloroform and added to this solution. The solution was allowed to react for four hours at 80 °C and subsequently extracted with DCM and water. The organic phase was then dried over magnesium sulfate and concentrated under reduced pressure. Pure **TT-ORh** was obtained as a dark red solid after precipitation from chloroform in methanol.

124 milligrams of product, 35% yield. ^{1}H-NMR (400 MHz, $CDCl_3$): δ (ppm) 7.89 (s, 2H), 7.59 (s, 2H), 4.12 (t, J = 7.67 Hz, 4H), 1.71 (p, J = 7.4 Hz, 4H), 1.42-1.21 (m, 20), 0.88 (t, J = 6.8 Hz, 6H). ^{13}C-NMR spectrum could not be recorded due to insufficient solubility.

5-(5-formylthiophen-2-yl)furan-2-carbaldehyde (4)

A dried Schlenk bomb was charged with 5-bromo-2-furaldehyde (588 mg, 3.36 mmol), (5-formylthiophen-2-yl)boronic acid (577 mg, 3.69 mmol) and palladium-tetrakis(triphenylphosphine) (233 mg, 0.2 mmol). 4.7 mL of a degassed 2 M potassium carbonate (K_2CO_3) solution was added to the Schlenk as well as 20 mL toluene and 11 mL methanol. This solution was degassed for 10 minutes before heating up. The mixture was stirred at 100 °C overnight and subsequently extracted with DCM and water. The organic phase was dried over magnesium sulfate and concentrated under reduced pressure. The crude product was purified by column chromatography (silicagel, eluent gradient 100:0 > 50:50 heptane:ethyl acetate). The resulting product was further purified by recrystallization from methanol and chloroform resulting in a brown solid, which still contained 3% of a homo-coupled impurity.

84 milligrams of product, 12% yield. ^{1}H-NMR (400 MHz, $CDCl_3$): δ (ppm) 9.94 (s, 1H), 9.70 (s, 1H), 7.75 (d, *J* = 3.99 Hz, 1H), 7.59 (d, *J* = 3.99 Hz, 1H), 7.32 (d, *J* = 3.76 Hz, 1H), 6.88 (d, *J* = 3.75 Hz, 1H). ^{13}C-NMR spectrum was not recorded due to the low amount of product.

(Z)-3-octyl-5-((5-(5-((Z)-(3-octyl-4-oxo-2-thioxothiazolidin-5-ylidene)methyl)furan-2-yl)thiophen-2-yl)methylene)-2-thioxothiazolidin-4-one (TF-ORh)

The same procedure as for **TT-ORh** was followed. Now, 84 mg (0.41 mmol) of **4** and 403 mg (1.64 mmol) of **ORh** were dissolved in 3.5 mL anhydrous chloroform. Six drops of piperidine were added and the mixture was let to react at 80 °C for three hours. After the extraction, the crude product was first precipitated from chloroform into methanol followed by recrystallization from methanol and chloroform. This yielded the product as a red solid, which still contained 1% of the bithiophene homo-coupled impurity.

201 milligrams of product, 74% yield. ^{1}H-NMR (400 MHz, $CDCl_3$): δ (ppm) 7.84 (s, 1H), 7.52 (d, *J* = 4.0 Hz, 1H), 7.44 (s, 1H), 7.40 (d, *J* = 4.08 Hz, 1H), 6.93 (d, *J* = 3.8 Hz, 1H), 6.84 (d, *J* = 3.7 Hz, 1H), 4.18-4.04 (m, 4H), 1.82-1.63 (m, 4H), 1.47-1.07 (m, 20H), 0.98-0.77 (m, 6H). ^{13}C-NMR (100 MHz, $CDCl_3$): δ (ppm) 193.76, 191.66, 167.42, 167.40, 152.17, 150.36, 138.67, 138.14, 134.71, 126.43, 124.15, 122.24, 121.91, 120.82, 116.62, 111.16, 44.96, 44.75, 31.77, 29.14, 27.02, 26.99, 26.79, 22.63, 14.09. (Note: several peaks in the ^{13}C-NMR spectrum overlap). MALDI-TOF-MS [M+] calc: 660.16 found: 660.16.

(Z)-5-((5-bromofuran-2-yl)methylene)-3-octyl-2-thioxothiazolidin-4-one (5)

A dried 3-neck flask was loaded with 475 mg (2.71 mmol) 5-bromo-2-furaldehyde, 1.33 g (5.42 mmol) **ORh,** 10 drops of piperidine and 23 mL anhydrous chloroform. The solution was allowed to react for three hours at 80 °C and subsequently extracted with DCM and water. Next, the organic phase was dried over magnesium sulfate and concentrated under reduced pressure. The resulting crude product was purified by column chromatography (silicagel, eluent gradient 100:0 > 60:40 heptane:DCM). This yielded pure compound **5** as a yellow solid.

825.6 milligrams of product, 76% yield. ^{1}H-NMR (400 MHz, $CDCl_3$): δ (ppm) 7.35 (s, 1H), 6.76 (d, *J* = 2.8 Hz, 1H), 6.52 (d, *J* = 2.6 Hz, 1H), 4.09 (t, *J* = 7.5 Hz, 2H), 1.79-1.61 (m, 2H), 1.44-1.16 (m, 10H), 0.96-0.75 (m, 3H). ^{13}C-NMR (100 MHz, $CDCl_3$): δ (ppm) 194.04, 167.51, 151.94, 128.26, 121.80, 120.05, 116.59, 116.48, 44.70, 31.77, 29.13, 27.00, 26.77, 22.63, 14.09. (Note: several peaks in the ^{13}C-NMR spectrum overlap).

(5Z,5'Z)-5,5'-([2,2'-bifuran]-5,5'-diylbis(methaneylylidene))bis(3-octyl-2-thioxothiazolidin-4-one) (2F-ORh)

A dried Schlenk tube was loaded with 400 mg (0.99 mmol) **5**, 303 mg (1.19 mmol) bis(pinacolato)diboron, 22 mg (0.03 mmol) Pd(dppf)Cl_2 and 293 mg (2.98 mmol) dried and finely

crushed potassium acetate. 3.2 mL dry dioxane was added and the mixture was subsequently degassed for 10 minutes. The mixture was heated to 110 °C and left to react for two hours. The reaction mixture was extracted with DCM and a saturated sodium bicarbonate solution. The organic layer was dried over magnesium sulfate and concentrated under reduced pressure. The crude product was purified by column chromatography (silicagel, eluent gradient 100:0 > 50:50 heptane:DCM). After recrystallization from methanol and chloroform, pure **2F-ORh** was obtained as a red solid.

174.5 milligrams of product, 54% yield. ^{1}H-NMR (400 MHz, $CDCl_3$): δ (ppm) 7.47 (s, 2H), 7.01 (d, *J* = 3.8 Hz, 2H), 6.98 (d, *J* = 3.8 Hz, 2H), 4.12 (t, *J* = 7.64 Hz, 4H), 1.89-1.62 (m, 4H), 1.47-1.15 (m, 20H), 0.96-0.78 (m, 6H). ^{13}C-NMR (100 MHz, $CDCl_3$): δ (ppm) 193.73, 167.39, 150.76, 148.60, 122.22, 120.57, 116.67, 111.86, 44.77, 31.78, 29.14, 27.03, 26.80, 22.64, 14.10. (Note: several peaks in the ^{13}C-NMR spectrum overlap). MALDI-TOF-MS [M+] calc: 644.19 found: 644.18.

5. References

(1) Fan, H.; Vergote, T.; Xu, S.; Chen, S.; Yang, C.; Zhu, X. A Thieno[3{,}4-b]Thiophene Linker Enables a Low-Bandgap Fluorene-Cored Molecular Acceptor for Efficient Non-Fullerene Solar Cells. *Mater. Chem. Front.* **2018**, *2* (4), 760–767.

(2) Li, X.; Li, K.; Su, D.; Shen, F.; Huo, S.; Fu, H.; Zhan, C. Design a Thieno[3,2-b]Thiophene Bridged Nonfullerene Acceptor to Increase Open-Circuit Voltage, Short-Circuit Current-Density and Fill Factor via the Ternary Strategy. *Chinese Chem. Lett.* **2020**, *31* (5), 1243–1247.

(3) Ye, C.; Wang, Y.; Bi, Z.; Guo, X.; Fan, Q.; Chen, J.; Ou, X.; Ma, W.; Zhang, M. High-Performance Organic Solar Cells Based on a Small Molecule with Thieno[3,2-b]Thiophene as π-Bridge. *Org. Electron.* **2018**, *53*, 273–279.

(4) Fan, X.; Gao, J.; Wang, W.; Xiao, S.; Zhan, C.; Lu, X.; Zhang, Q. Ladder-Type Nonacyclic Arene Bis(Thieno[3,2-b]Thieno)Cyclopentafluorene as a Promising Building Block for Non-Fullerene Acceptors. *Chem. – An Asian J.* **2019**, *14* (10), 1814–1822.

(5) Zhai, W.; Tang, A.; Xiao, B.; Wang, X.; Chen, F.; Zhou, E. A Small Molecular Electron Acceptor Based on Asymmetric Hexacyclic Core of Thieno[1,2-b]Indaceno[5,6-B′]Thienothiophene for Efficient Fullerene-Free Polymer Solar Cells. *Sci. Bull.* **2018**, *63* (13), 845–852.

(6) Gao, H.-H.; Sun, Y.; Wan, X.; Kan, B.; Ke, X.; Zhang, H.; Li, C.; Chen, Y. Design and Synthesis of Low Band Gap Non-Fullerene Acceptors for Organic Solar Cells with Impressively High Jsc over 21 MA Cm_2. *Sci. China Mater.* **2017**, *60* (9), 819–828.

(7) Manion, J. G.; Ye, S.; Proppe, A. H.; Laramée, A. W.; McKeown, G. R.; Kynaston, E. L.; Kelley, S. O.; Sargent, E. H.; Seferos, D. S. Examining Structure–Property–Function Relationships in Thiophene, Selenophene, and Tellurophene Homopolymers. *ACS Appl. Energy Mater.* **2018**, *1* (9), 5033–5042.

(8) Cameron, J.; Abed, M. M.; Chapman, S. J.; Findlay, N. J.; Skabara, P. J.; Horton, P. N.; Coles, S. J. Investigating the Effect of Heteroatom Substitution in 2{,}1{,}3-Benzoxadiazole and 2{,}1{,}3-Benzothiadiazole Compounds for Organic Photovoltaics. *J. Mater. Chem. C* **2018**, *6* (14), 3709–3714.

(9) Islam, A.; Liu, Z.; Peng, R.; Jiang, W.; Lei, T.; Li, W.; Zhang, L.; Yang, R.; Guan, Q.; Ge, Z. Furan-Containing Conjugated Polymers for Organic Solar Cells. *Chinese J. Polym. Sci.* **2017**, *35* (2), 171–183.

(10) Li, C.; Song, J.; Cai, Y.; Han, G.; Zheng, W.; Yi, Y.; Ryu, H. S.; Woo, H. Y.; Sun, Y. Heteroatom Substitution-Induced Asymmetric A–D–A Type Non-Fullerene Acceptor for Efficient Organic Solar Cells. *J. Energy Chem.* **2020**, *40*, 144–150.

(11) Yu, H.; Qi, Z.; Zhang, J.; Wang, Z.; Sun, R.; Chang, Y.; Sun, H.; Zhou, W.; Min, J.; Ade, H.; Yan, H. Tailoring Non-Fullerene Acceptors Using Selenium-Incorporated Heterocycles for Organic Solar Cells with over 16% Efficiency. *J. Mater. Chem. A* **2020**, *8* (45), 23756–23765.

(12) Li, Y.; Zhong, L.; Wu, F.-P.; Yuan, Y.; Bin, H.-J.; Jiang, Z.-Q.; Zhang, Z.; Zhang, Z.-G.; Li, Y.; Liao, L.-S. Non-Fullerene Polymer Solar Cells Based on a Selenophene-Containing Fused-

Ring Acceptor with Photovoltaic Performance of 8.6%. *Energy Environ. Sci.* **2016**, *9* (11), 3429–3435.
(13) Turkoglu, G.; Cinar, M. E.; Ozturk, T. Thiophene-Based Organic Semiconductors. In *Sulfur Chemistry*; Jiang, X., Ed.; Springer International Publishing: Cham, 2019; pp 79–123.
(14) Barroso, S.; Joksch, M.; Puylaert, P.; Tin, S.; Bell, S. J.; Donnellan, L.; Duguid, S.; Muir, C.; Zhao, P.; Farina, V.; Tran, D. N.; de Vries, J. G. Improvement in the Palladium-Catalyzed Miyaura Borylation Reaction by Optimization of the Base: Scope and Mechanistic Study. *J. Org. Chem.* **2021**, *86* (1), 103–109.
(15) Takagi, J.; Takahashi, K.; Ishiyama, T.; Miyaura, N. Palladium-Catalyzed Cross-Coupling Reaction of Bis(Pinacolato)Diboron with 1-Alkenyl Halides or Triflates: Convenient Synthesis of Unsymmetrical 1,3-Dienes via the Borylation-Coupling Sequence. *J. Am. Chem. Soc.* **2002**, *124* (27), 8001–8006.
(16) Ji, H.; Wu, L. Y.; Cai, J. H.; Li, G. R.; Gan, N. N.; Wang, Z. H. Room-Temperature Borylation and One-Pot Two-Step Borylation/Suzuki-Miyaura Cross-Coupling Reaction of Aryl Chlorides. *RSC Adv.* **2018**, *8* (25), 13643–13648.
(17) Nising, C. F.; Schmid, U. K.; Nieger, M.; Bräse, S. A New Protocol for the One-Pot Synthesis of Symmetrical Biaryls. *J. Org. Chem.* **2004**, *69* (20), 6830–6833.
(18) Dzhevakov, P. B.; Topchiy, M. A.; Zharkova, D. A.; Morozov, O. S.; Asachenko, A. F.; Nechaev, M. S. Miyaura Borylation and One-Pot Two-Step Homocoupling of Aryl Chlorides and Bromides under Solvent-Free Conditions. *Advanced Synthesis and Catalysis*. 2016, pp 977–983.
(19) Gidron, O.; Varsano, N.; Shimon, L. J. W.; Leitus, G.; Bendikov, M. Study of a Bifuran vs. Bithiophene Unit for the Rational Design of π-Conjugated Systems. What Have We Learned? *Chem. Commun.* **2013**, *49* (56), 6256–6258.
(20) Hendsbee, A. D.; Sun, J. P.; McCormick, T. M.; Hill, I. G.; Welch, G. C. Unusual Loss of Electron Mobility upon Furan for Thiophene Substitution in a Molecular Semiconductor. *Org. Electron.* **2015**, *18*, 118–125.
(21) Pachariyangkun, A.; Suda, M.; Hadsadee, S.; Jungsuttiwong, S.; Nalaoh, P.; Pattanasattayavong, P.; Sudyoadsuk, T.; Yamamoto, H. M.; Promarak, V. Effect of Thiophene/Furan Substitution on Organic Field Effect Transistor Properties of Arylthiadiazole Based Organic Semiconductors. *J. Mater. Chem. C* **2020**, *8* (48), 17297–17306.

Appendix A: Unsuccessful synthetic procedures

As mentioned in chapter 3, several synthetic routes were attempted to synthesize the two furan-based NFAs. For both NFAs, the bottleneck in these routes was the synthesis of the bi-aldehyde. In the following sections, the different unsuccessful synthetic routes that were tried to synthesize the thiophene-furan and the bifuran bi-aldehydes are discussed. All the synthetic procedures were performed under an N_2 atmosphere.

1. Stille cross-coupling followed by a single formylation

The first route attempted to synthesize the desired bi-aldehydes is shown in **Scheme A.1**. The first step in this route is a Stille cross-coupling (CC) between 5-bromofuran-2-carbaldehyde and 2-(tributylstannyl)thiophene or 2-(tributylstannyl)furan. After stirring the crude reaction mixture for 1 hour in a 1M sodium hydroxide solution, to make the polar tributyltin hydroxide, and purification by column-chromatography both products were obtained in a good yield of around 80%. The final step to form the desired bi-aldehyde was a single formylation. During this reaction, the aldehyde group that was already on the molecule degraded under the described conditions, as confirmed by the disappearance of the aldehyde peak in the ^{1}H-NMR spectrum.

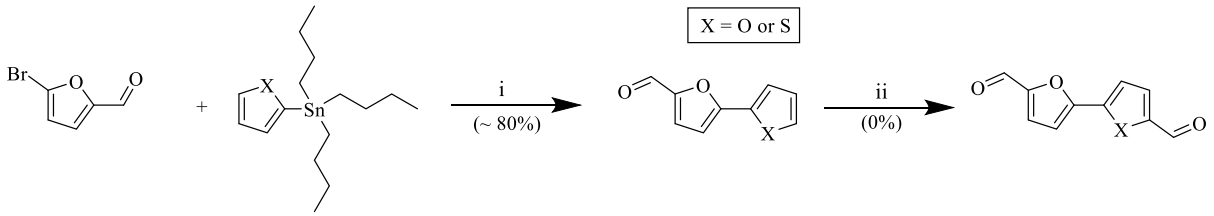

Scheme A.1: Synthesis route of the targeted bi-aldehydes, based on a Stille cross-coupling followed by a single formylation. (i) 1) $Pd_2(dba)_3$, PPh_3, Tol./DMF (90:10), 115 °C 2) Work-up with 1M NaOH ; (ii) 1) 1.1 eq. LDA/THF, -78 °C, 2) 2 eq. DMF, -78 °C. Reaction yields are given between parentheses.

2. Stille cross-coupling followed by a double formylation

Because the previous route showed degradation of the aldehyde during the final formylation step, a double formylation route was tried (**Scheme A.2**). In this route the first step was again a Stille CC, but this time with 2-bromofuran instead of 5-bromofuran-2-carbaldehyde, giving 2-(thiophen-2-yl)furan in a good yield. Now, the final step was a double formylation reaction, using *n*-butyllithium as a base instead of lithium diisopropylamide. This change was done because the work of Dai *et al.* showed the exact same reaction in a moderately good yield (44%).[1] Unfortunately, in our case the reaction only resulted in mono-formylated compound.

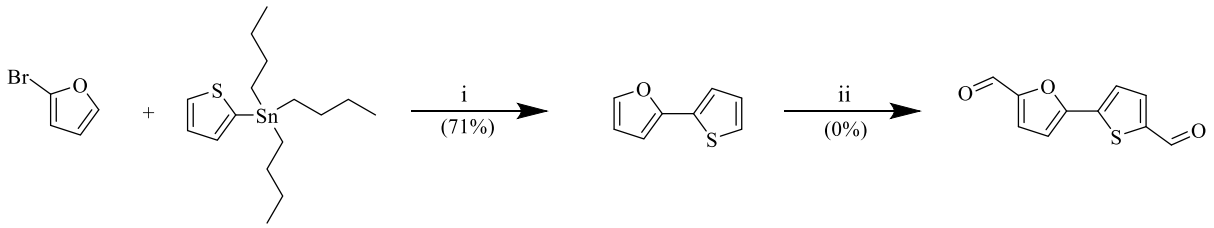

Scheme A.2: Synthesis route of one of the targeted bi-aldehydes, based on a Stille cross-coupling followed by a double formylation. (i) 1) $Pd(PPh_3)_4$, Tol./DMF (90:10), 115 °C 2) Work-up with 1M NaOH ; (ii) 1) 2.2 eq *n*BuLi/THF, -78 °C, 2) 3 eq. DMF, -78 °C. Reaction yields are given between parentheses.

3. Screening of Suzuki-Miyaura cross-coupling reaction conditions

Since the first attempted synthetic routes showed difficulties in the final formylation step, new routes were tried to yield the desired bi-aldehyde in only one step. A synthetic route to avoid this is based on the direct coupling of two aldehyde-moieties through a Suzuki-Miyaura cross-coupling reaction.

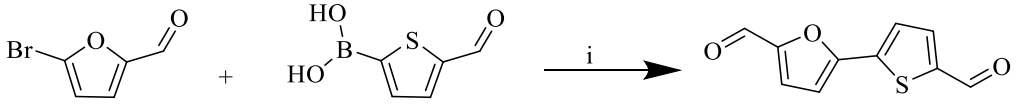

Scheme A.3: Synthesis route of one of the targeted bi-aldehydes, based on a Suzuki-Miyaura cross-coupling reaction. (i) $Pd(PPh_3)_4$, 2M K_2CO_3, other conditions are as shown in **Table A.1**.

For this reaction as shown in **Scheme A.3** several conditions have been screened, which are listed in **Table A.1**. Firstly, the reaction was performed using tetrahydrofuran (THF) as a solvent, chosen because it is an often used solvent in Suzuki-Miyaura CC reactions.[2] A small amount of toluene was added to the reaction mixture because the catalyst did not dissolve properly in pure THF. Unfortunately, only a trace amount of the desired product was visible after the reaction and the ^{1}H-NMR showed mainly starting compounds. The solvent system was then changed to a mixture of toluene and methanol, which allowed for higher reaction temperatures. This was the reaction that yielded a small amount of the desired bi-aldehyde, as described in chapter 3. In order to enhance the reaction yield, a phase transfer agent, Aliquat 336, was added to the reaction mixture. This should help with the activation of the catalyst by the base. However, this reaction resulted in a black, almost gelatinous reaction mixture, from where no desired product could be identified. In the last attempted modification, the solvent system was changed to toluene and dimethylformamide (DMF). Regretfully, this again resulted in a black slurry-like reaction mixture.

Table A.1: Effect of changing the reaction conditions on the yield of the Suzuki-Miyaura cross-coupling reaction.

Entry	Solvent	Temperature [°C]	Phase transfer agent [a]	Yield [%]
1	90% THF + 10% toluene	80	No	Trace
2	60% toluene + 40% methanol	100	No	12 [b]
3	60% toluene + 40% methanol	100	Yes	-
4	80% toluene + 20% DMF	115	Yes	-

[a] One drop of Aliquat 336 was added to the reaction mixture. [b] Trace amounts of homocoupling left after purification steps.

Since the reaction described in entry 2 yielded a little amount of furan-thiophene bi-aldehyde, it was performed again in the exact same manner to synthesize the bifuran bi-aldehyde. However, the reaction resulted in a very low amount of product, which showed a significant amount of believed triphenylphosphine-oxide after purification by column-chromatography.

4. Stille-type homo-coupling

Since the aforementioned reactions have not proven successful in synthesizing the bifuran bi-aldehyde a Stille-type homo-coupling using hexamethyl-ditin was tried (**Scheme A.4**). Several papers have reported these type of homo-coupling reactions in relatively high yields.[3,4] The crude proton NMR of a small scale test-reaction showed that the desired product was obtained in relatively high amounts and that only a little amount of unidentified side-product was formed. Unfortunately, the large scale reaction showed a more than 10-fold increase in the formed unidentified side-product. A purification by column

chromatography was attempted in order to separate the desired product. Regretfully, the collected fractions still contained a large amount of what is believed to be triphenylphosphine-oxide.

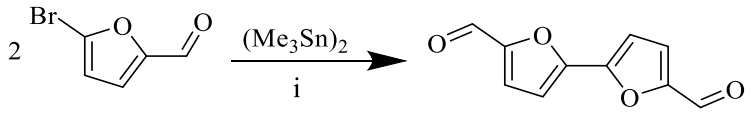

Scheme A.4: Synthesis route of the bifuran bi-aldehyde, based on a Stille-type homo-coupling. (i) $Pd(PPh_3)_4$, Tol./DMF (90:10), 115 °C.

When comparing the performed Stille CC reactions described in sections **1** and **2** and the reactions described in sections **3** and **4** we find much higher yields in the CC reactions reported in sections **1** and **2**. In these reactions there was no aldehyde on the stannylated compound. The higher yields found combined with reported Suzuki-Miyaura CC reactions using protected aldehydes on the boronic acid/ester moieties,[5,6] leads us to believe that the aldehyde impedes the transmetalation step in the catalytic cycle.

5. References

(1) Dai, W.-M.; Mak, W. L. First Synthesis of Dioxadithiaporphycene with a Benzene Ring Fused onto the Double Bond. *Tetrahedron Lett.* **2000**, *41* (52), 10277–10280.

(2) Molander, G. A.; Felix, L. A. Stereoselective Suzuki−Miyaura Cross-Coupling Reactions of Potassium Alkenyltrifluoroborates with Alkenyl Bromides. *J. Org. Chem.* **2005**, *70* (10), 3950–3956.

(3) Echavarren, A. M.; Stille, J. K. Palladium-Catalyzed Coupling of Aryl Triflates with Organostannanes. *J. Am. Chem. Soc.* **1987**, *109* (18), 5478–5486.

(4) Gribanov, P. S.; Golenko, Y. D.; Topchiy, M. A.; Philippova, A. N.; Kirilenko, N. Y.; Krivoshchapov, N. V.; Sterligov, G. K.; Asachenko, A. F.; Bermeshev, M. V.; Nechaev, M. S. One-Pot Two-Step Stannylation/Stille Homocoupling of Aryl Bromides and Iodides under Solvent-Free Conditions. *Mendeleev Commun.* **2018**, *28* (3), 323–325.

(5) McClure, M. S.; Roschangar, F.; Hodson, S. J.; Millar, A.; Osterhout, M. H. A Practical One-Pot Synthesis of 5-Aryl-2-Furaldehydes. *Synthesis (Stuttg).* **2001**, *2001* (11), 1681–1685.

(6) Hergert, T.; Varga, B.; Thurner, A.; Faigl, F.; Mátravölgyi, B. Copper-Facilitated Suzuki-Miyaura Coupling for the Preparation of 1,3-Dioxolane-Protected 5-Arylthiophene-2-Carboxaldehydes. *Tetrahedron* **2018**, *74* (16), 2002–2008.

Acknowledgements

It has been a weird year, due to the current Covid-19 crisis. I would be lying if I was saying I wasn't bummed that everything went differently than initially expected. The couple of months that I had to wait to start my graduation project and the following tight time schedules when I could finally start in the lab made the start of my project somewhat hectic. During my project there has been quite some set-backs which at one point had me quite down, because in the evenings there was no distraction possible with the Covid regulations. But there were so many people who helped pull me through these weird and though times and therefore I'm even more happy to finally have come to the point of thanking them.

First of all, I want to thank Prof. Janssen for the opportunity to do my graduation project in his group. His kind words and all the advice during the synthesis and individual meetings were a great help in finding my way in the world of organic photovoltaics.

Furthermore, I would like to thank Dr. Wienk for all his questions and input during the synthesis meetings, you really helped me to think critically about the data I had collected.

And then the most important "thank you". Pieter I still think you're crazy for taking me in during the last year of your PhD, but I couldn't be more grateful that you did. Your never-ending enthusiasm is contagious and is one of the things that really helped cheer me up when I was feeling a bit down. You even made me like doing synthesis again, something I thought wouldn't happen (although doing a column will never be my favorite thing). I'm very grateful for all the lab-skills you have taught me like: safe synthesis, device fabrication and all the measuring techniques. As well as all the tips you gave me and discussions we had when interpreting the data. You also could not have anticipated that my project would take so much longer so that you've had already long finished your PhD by the time that I was done. Yet still you were there for me after you've finished, something I think cannot be underestimated. Best of luck with your new job!!

I would like to thank Prof. Janssen, Dr. Wienk, Dr. Leenaers and Prof. Schenning for taking the time to take part in my graduation committee.

The bi-weekly synthesis meetings were a great way to get some feedback and help. So for that I would like to thank Nicolas, Haijun, Bart and Koen. A special thanks to Koen for helping me out with my square wave voltammetry measurements.

Nicolas, often it was just the two of us in the synthesis lab and maybe more than anyone you've heard me complaining abound failed synthesis or long and boring columns. Your typical answer "it's gonna be fiiinneee" luckily came true in the end. So I want to thank you for all the advice and laughs during my synthesis times.

Additionally, I would like to thank Ralf Bovee for measuring MALDI-TOF and Haijun for the AFM measurements.

I also want to thank my (intruding) officemates Stan and Alex as well as Guus and Steffijn for their friendship and distractions during times where I needed to not think about my project and the occasional beers and hamburgers when Covid-regulations allowed for it.

Furthermore, I want to thank all the members of the M2N group for the nice atmosphere, guidance and suggestions during my time here. A special thanks to Margot, for the occasional office-door talks, laughs, support and for arranging all sort of things.

Besides everyone at the TU/e I also want to thank the people who supported me when I was not working on my project. I have not been the easiest person to be around the last couple of months, because at moments all I could talk about was the hard time I had with my project. But still you managed to put a

smile on my face and to motivate me to pull through. A special thanks to my parents for all the emotional support and for encouraging me to continue with my masters, without you I would not be here. Thomas, you've always been there for me and if there was one person who always said I could do it, it'd be you. Thank you so much for helping me get my mind off things by always making me smile and by pushing me to do relaxing things. Thank you for keeping up with me, all the complaining and mood swings the last couple of months could not have been easy. I promise you I'll try to be less of a "stress-kip" now that I'm done!